This is to certify that the
dissertation entitled

TRANSPORT CHARACTERIZATION OF NEW HIGH TEMPERATURE QUATERNARY THERMOELECTRIC MATERIALS AND DEVICES

presented by

SIM YEAN LOO

has been accepted towards fulfillment
of the requirements for the

Ph.D. degree in Electrical Engineering

Major Professor's Signature

8/14/03

Date

TRANSPORT CHARACTERIZATION OF NEW HIGH TEMPERATURE QUATERNARY THERMOELECTRIC MATERIALS AND DEVICES

By

Sim Yean Loo

A DISSERTATION

Submitted to
Michigan State University
In partial fulfillment of the requirements
For the degree of

DOCTOR OF PHILOSOPHY

Department of Electrical and Computer Engineering

2003

ABSTRACT

TRANSPORT CHARACTERIZATION OF NEW HIGH TEMPERATURE QUATERNARY THERMOELECTRIC MATERIALS AND DEVICES

By

Sim Yean Loo

A new computer-controlled high temperature thermoelectric transport measurement system was built for investigating new high temperature quaternary thermoelectric materials and devices. Such thermoelectric materials are desirable for power generation applications – converting thermal energy to electricity. Some of the advantages of thermoelectric devices include no moving parts, solid-state construction, environmentally friendliness, and high reliability. An increasing concern of environment and awareness of limited resources has made waste heat recovery an urgent global issue.

The high temperature thermoelectric system is computer-controlled by LabVIEW™ programming with extensive PID temperature control. It can be used to characterize the thermoelectric power (S) and electrical conductivity (σ) of electronic materials in a broad temperature range (80-800K). The figure of merit, ZT ($= S^2\sigma T/\kappa$), is used to define the efficiency of thermoelectric materials. The measured power factor ($S^2\sigma$) can be used to identify good candidates for thermoelectric applications. Some of the new quaternary materials exhibit power factor larger than 30 $\mu W/K^2 \cdot cm$ in a wide temperature range of 300-600K. Since these materials are expected to have very low thermal conductivity at high temperatures, a ZT of approaching or larger than 1 at high temperatures can be achieved. Three of the best thermoelectric materials: bismuth telluride alloys, lead telluride alloys and silicon-germanium, have a ZT of ~1 at their

optimum temperatures. The experimental results also reveal the new quaternary materials as narrow-band gap semiconductors with metallic behavior.

The theory behind thermoelectric materials will be reviewed; this includes the search of materials with large band degeneracy or high anisotropy, the parameters that can enhance the B-factor, and the coefficient of performance as well as the efficiency of the thermoelectric devices. The structural design and automated features of the measurement system will be presented. The technique of material/device characterization will be discussed as well as the results of investigations on new quaternary materials and devices constructed with these materials.

Dedicated to my sweet husband, Roger Booth.

ACKNOWLEDGEMENTS

This research would not have been possible without the patience and guidance of my advisor, Dr. Tim Hogan. He has contributed a significant amount of time to introduce many students, including me, to the world of scientific research. It has been a great experience working for Dr. Hogan and I value everything that I have learned in this lab, not just the spirit of research, but also the working manner, attitude and ethics. I would also like to thank all the people with whom I have worked in the thermoelectric project, including Duck-Young Chung, Kuei-Fang Hsu, Sangeeta Lal, Daniel Bilc and etc.

I would like to thank Dr. Mercouri Kanatzidis, Dr. Tim Grotjohn and Dr. Don Reinhard for taking the time to review my thesis, attending my presentation and contributing to some helpful discussions. I would like to thank Dr. Eldon Case for assisting in the material science aspect of thermoelectrics investigation. I also feel grateful for all the wonderful lab colleagues I have worked with.

At last, but not the least, I would like to thank my husband, Roger Booth, my parents, my parents in-law, and my aunt Chim and uncle Roberto for all their support throughout the years.

I am also grateful for the financial support of the Office of Naval Research and DARPA through grants N00014-01-1-0728.

TABLE OF CONTENTS

Chapter 3

Module/prototype Design

Chapter 4

High temperature measurement system

Chapter 5

Experimental Results of the system

LIST OF TABLES

Chapter 2

Chapter 3

Chapter 4

Chapter 5

Chapter 6

LIST OF FIGURES

Chapter 2

Chapter 3

Chapter 4

Chapter 5

F

F

F

F

Fig

Fig

Fig

Fig

Figu

Figu

Figur

Chapter 6

Chapter 1 Introduction

New perspectives on thermoelectric research are explored at Michigan State University through collaborations among the Electrical Engineering, Chemistry and Physics departments. My role in this research has been in developing a new transport measurement system and module design/prototype that will be compatible with the newly discovered thermoelectric materials. A new computer-controlled thermoelectric measurement system is built to characterize the electrical and thermal properties of new thermoelectric materials, primarily at high temperatures (up to 800K). Thermoelectric research at high temperatures is desirable since materials with high thermoelectric efficiency at high temperatures have potential applications in power generation. Using this system, we can study the new materials' properties over a very broad temperature range. Quaternary cubic materials are the main focus in this investigation. Knowledge in chemistry (e.g. chemical structure in doping and alloying, crystallography and etc.) and physics (e.g. band gap calculation, band diagram and etc.) is required to understand why the materials have such properties.

The uniqueness of this research includes the thermoelectric properties of new high temperature quaternary cubic materials obtained for the first time through this high temperature measurement system. The development of this measurement system as part of this research has further allowed for the investigation of thermoelectric properties for other materials not included in this work, primarily at high temperatures. Since these measurements will give the first insight of the thermoelectric properties of new materials, the system is an important tool used to investigate these new materials. This high temperature TE measurement system is specially designed to measure small geometry

bulk samples and some of the unique features of this system include computer-control through LabVIEW™ programming. Through such programming, routes to temperature stabilization and control have been investigated. This has also allowed for the collection of large number of data points in the experiments. These features have overcome some of the limitations found among the few existing high temperature TE measurement systems.

A broad and detailed background of thermoelectricity is introduced in the first part of the thesis. This section includes the theoretical background of thermoelectrics, the transport theory relating to thermoelectrics, the investigation of old and new thermoelectric materials and the various techniques of material/module characterization. The next section gives a description of the new high temperature system, including the structural design, and automated features, especially in temperature control of the system. The experimental results will be presented and a detailed investigation on the new quaternary cubic materials will be discussed based on the experimental results. Finally, a thermoelectric module will be fabricated with these types of materials and the performance of this module will be discussed.

Chapter 2 Background

Thermoelectric (TE) materials have been investigated ever since the discovery of thermoelectric effects in the 1800s. Their lightweight, lack of moving parts and environmental friendliness are just some of the advantages of TE devices. However, the low efficiency of TE devices has made them less viable as commercial devices. The search for high efficiency TE materials lies in discovering materials with a high figure of merit, ZT [1]. The figure of merit includes the thermoelectric power (Absolute Seebeck Coefficient) (S), electrical conductivity (σ) and thermal conductivity (κ) of the sample, while T is the absolute temperature. Z has unit of $1/K$ thus ZT is a unitless quantity. The higher the ZT, the better the material for TE applications.

$$ZT = \frac{S^2\sigma}{\kappa}T \tag{1.}$$

2.1.1 What is Thermoelectrics?

Thermoelectrics is the study of the conversion between thermal and electrical energy. There are three thermoelectric effects associated with it. The first thermoelectric phenomenon was discovered in 1823 by Seebeck. He found that when heat was applied to one of the junctions of two dissimilar metals, when connected in a closed loop configuration as shown in Figure 2.1 a), he would measure a deflection on his galvanometer. Seebeck thought it was a magnetic effect and pursued a derivation to explain this phenomenon. He had investigated a large number of materials, including some we now call semiconductors, and arranged them in order of the product of Seebeck

coefficient, S, and electrical conductivity, σ. Although, he had pursued the wrong direction, he did gather a lot of useful information for many materials.

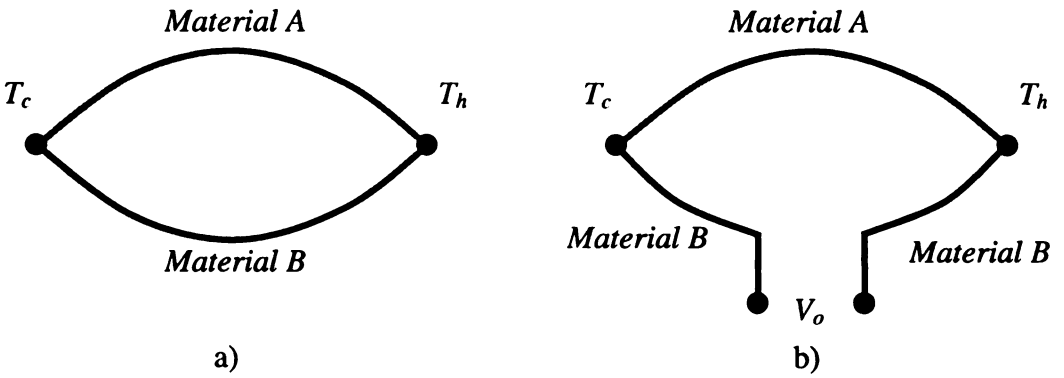

Figure 2.1 Seebeck Effect.

With the discovery of Faraday's Law, the magnetic field measured by Seebeck was better understood to be caused by a current flowing in the closed loop of Figure 2.1 a). This was later verified by a corresponding open circuit voltage when the loop was broken as shown in Figure 2.1 b). The relative Seebeck coefficient is expressed as the voltage, V_o divided by the temperature gradient, $\Delta T = (T_h - T_c)$,

$$S_{AB} = \frac{V_o}{\Delta T} \tag{2.}$$

The Seebeck voltage is also known as Seebeck electromotive force, emf. The application of the Seebeck effect is a thermocouple. A thermocouple is a device which converts thermal energy to electric energy. It is made up of two dissimilar conductors and when the junctions are in different temperatures, a Seebeck emf or voltage is produced. The amount of electric energy produced can be used to measure temperature. When a reference temperature is used, the temperature difference, and consequently the emf of a thermocouple, becomes a function of the temperature of the measuring junction. This

functional dependence permits the establishment of lookup tables, curves or mathematic relationships for a specific type of thermocouple.

About 12 years after the discovery of Seebeck, Jean Peltier discovered the second effect which shows a temperature gradient across the junctions of two dissimilar metals when a current, *I*, is applied.

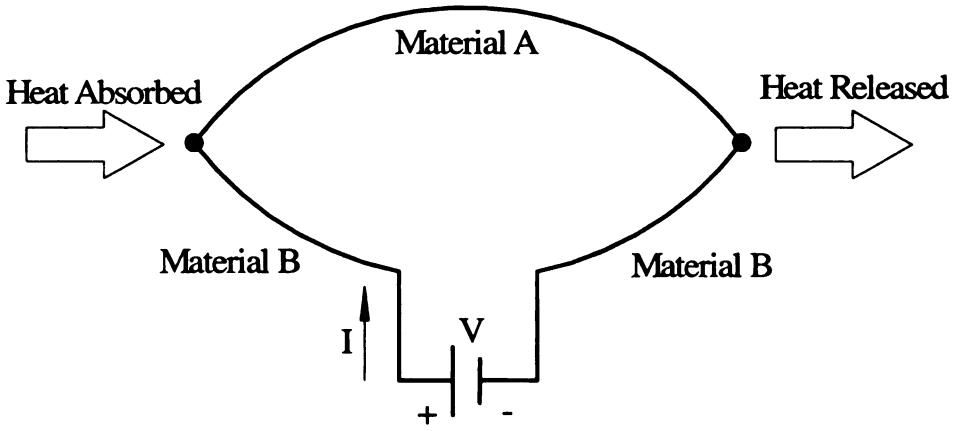

Figure 2.2 Peltier Effect.

Figure 2.2 shows the Peltier effect. The heat flow (*dQ/dt*, energy per unit time) away from the junction was found to be proportional to the current, *I* with the proportionality constant, $\prod$, defined as the Peltier coefficient

$$\Pi_{AB} = \frac{dQ}{dt \cdot I} \tag{3.}$$

Unfortunately, these fascinating discoveries were neglected since the electromagnetic phenomena were also discovered and developed around the same time, and had caught the attention of many scientists during that period.

Some twenty years passed before interest in direct thermal to electric energy conversion found renewed interest following the further development of

thermodynamics. In 1851, Thomson had discovered a third effect, which described how a single homogeneous metal could release or absorb heat depending on the direction of the current flow in the presence of a temperature gradient on it. To restate this phenomena [2], if the electrons move along the increasing temperature gradient (from cold to hot), the material will absorb the energy (heat) and the potential energy of the electrons is increased. If the electrons move along the same direction as the gradient (from hot to cold), the material will give up the energy (heat) and the potential energy of the electrons is decreased.

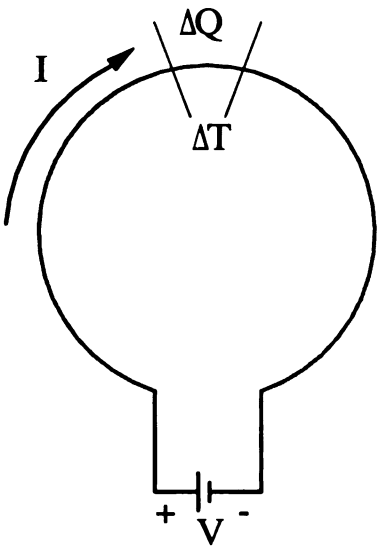

Figure 2.3 Thomson Effect.

Figure 2.3 shows the Thomson effect which describes the development of a temperature gradient, ΔT, along the length of a single material when current, I, flows through the sample. A corresponding absorption or emission of heat, ΔQ, is proportional to the product of the current and temperature gradient, with the proportionality constant, γ_T, defined as the Thomson coefficient

$$\gamma_T = \frac{\Delta Q}{I \cdot \Delta T} \tag{4.}$$

Thus, a net heat flow in a single homogeneous conductor per unit volume per unit time is

$$\Delta Q = I^2 R - \gamma_T \cdot \Delta T \cdot I \tag{5.}$$

where I is the current density, R is the electrical resistance of the conductor. The first term on the right side is the irreversible Joule heating and the second term is the reversible Thomson effect. The sign of the second term is positive if heat is absorbed and negative is heat is liberated.

Thomson further derived a relationship between the Seebeck and Peltier effects,

$$\Pi_{AB} = S_{AB} T \tag{6.}$$

and also related the Seebeck effect to Thomson effect,

$$S = \int_0^T \frac{\gamma_T}{T} dT \tag{7.}$$

where S is the absolute thermoelectric power of a single conductor. Equations 6 and 7 also known as the Kelvin relations and the Seebeck effect of a thermocouple can be expressed as

$$S_{AB} = S_A - S_B = \int_0^T \frac{\gamma_{TA}}{T} dT - \int_0^T \frac{\gamma_{TB}}{T} dT \tag{8.}$$

Equation 8 shows that the Seebeck effect or thermoelectric power of a thermocouple can be expressed as the algebraic sum of the absolute thermoelectric power of each of the

individual elements. This result is crucial because it allows one to predict the properties of a thermocouple if the thermoelectric properties of the individual element are known.

There are three ways to better visualize the thermoelectric power of a material. One way is to consider the Thomson effect, which describes the reversible heat change and is related to the current and emfs in the conductor along the temperature gradient, this property of the material is called the absolute thermoelectric power. Another way is to consider a thermocouple made of a superconductor and the sample of interest. Since superconductors show no thermoelectric effects below their transition temperatures, usually at very low temperatures (<21K), the observed thermoelectric effect of this thermocouple at these temperatures must be only by the sample of interest. Greater accuracy can then be found for a given reference material (such as lead, or platinum) by forming a junction between the reference material and a superconductor, and measuring the junction at temperatures below the transition temperature of the superconductor. The data for the reference material that was obtained over a wide temperature range can then be shifted to align with the low temperature data for a more accurate reference material data set. This calibrated reference material can then be used to form a junction with other unknown samples, and determine their thermopower.

2.1.2 Why Thermoelectric?

The uniqueness and advantages of thermoelectric devices has been reviewed [3] over many years. For cooling applications, much effort has been made toward replacing existing compressor-based devices with thermoelectric devices. However, there are many other applications where TE devices are the best choice.

The advantages of TE devices are:

1. No moving parts – less maintenance required
2. Solid-state construction – can operated under harsh conditions, e.g. under vibration
3. Environmentally friendly
4. Scalability – light weight, small size devices
5. Act as a converter – can be a cooler or a power generator
6. Can be operated in any orientation and in zero gravity environment
7. Low electronic signature (noise)
8. High reliability, and long lifetime

2.1.3 How Does A Thermoelectric Device Work?

Thermoelectric devices can consist of a single couple (or commonly known as a thermocouple) as shown in Figure 2.4, or many such couples connected together. Most TE devices consist of a *p* and an *n*-type material forming the couple since this configuration gives the best performance.

The gray strips at the top and bottom of the device shown in Figure 2.4 are the metal connections. This couple is connected electrically in series and thermally in parallel. To distinguish between the efficiency of a thermoelectric generator and a thermoelectric cooler, the efficiency of a cooler is titled the coefficient of performance (COP), ϕ, while the efficiency of a generator is titled efficiency, η. Since TE devices can be scaled without loss of efficiency, the coefficient of performance (COP) of a TE cooler can be derived on the basis of a single TE couple.

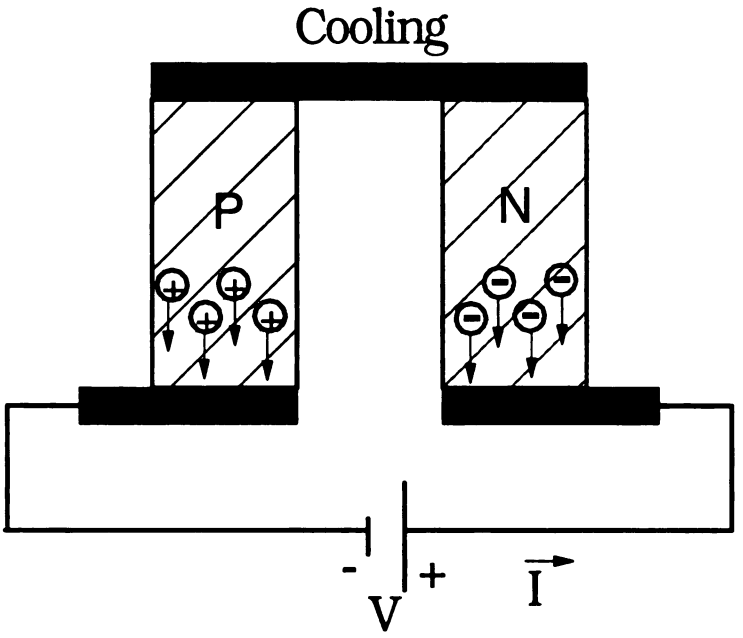

Figure 2.4 TE module (couple) for Cooling.

In Figure 2.4, when current flows from *n* to *p*-type material, both carriers flow from the top to the bottom plates, carrying heat with them. This has made the top plate an active cooling area and the bottom plate a heat source. Reverse the direction of current will result the cooling in the bottom plate and heat flow from the bottom to the top. This construction utilizes the Peltier effect and thus, is often called Peltier cooling.

The cooling effect is offset only in equilibrium between them by the Joule heating (I^2R) and by heat conducted from the hot junction. It shows that half of the overall Joule heating goes to each junction. The rate of absorption of heat from the source is

$$Q = S_{pn} T_c I - \frac{1}{2} I^2 R - K\Delta T \qquad (9.)$$

and $\Delta T = T_h - T_c$

Part of the potential difference applied to the couple is employed in overcoming the resistance of the branches and part is used to balance the Seebeck voltage resulting from the temperature difference between the junctions. Thus, the power W supplied to the couple is given by

$$W = S_{pn}\Delta TI + I^2R \tag{10.}$$

After some derivations [4], the coefficient of performance, ϕ, for a TE cooler is defined as the ratio of Q/W, which is

$$\phi = \frac{S_{pn}T_cI - \frac{1}{2}I^2R - K\Delta T}{S_{pn}\Delta TI + I^2R} \tag{11.}$$

The maximum COP is determined by taking the derivative of equation (11) with respect to current I - setting equal to zero and solving for I_{max}

$$I_{\max} = \frac{S_{pn}\Delta T}{R}\left(\frac{1}{\sqrt{1+ZT_M}-1}\right) \tag{12.}$$

then inserting I_{max} into (11) gives,

$$\phi_{\max} = \frac{T_M\left(\sqrt{1+ZT_M}-1\right)}{\Delta T\left(\sqrt{1+ZT_M}+1\right)} - \frac{1}{2} \tag{13.}$$

where $T_M = (T_h+T_c)/2$

In Figure 2.5, the TE couple is electrically connected to a load on one end and when heat is applied to the other end, electrons in the *n*-type, and holes in the *p*-type legs preferentially flow from the top (higher energy) plate to the bottom (lower energy) plate. A current, I, is thus induced and the structure works as a power generation device.

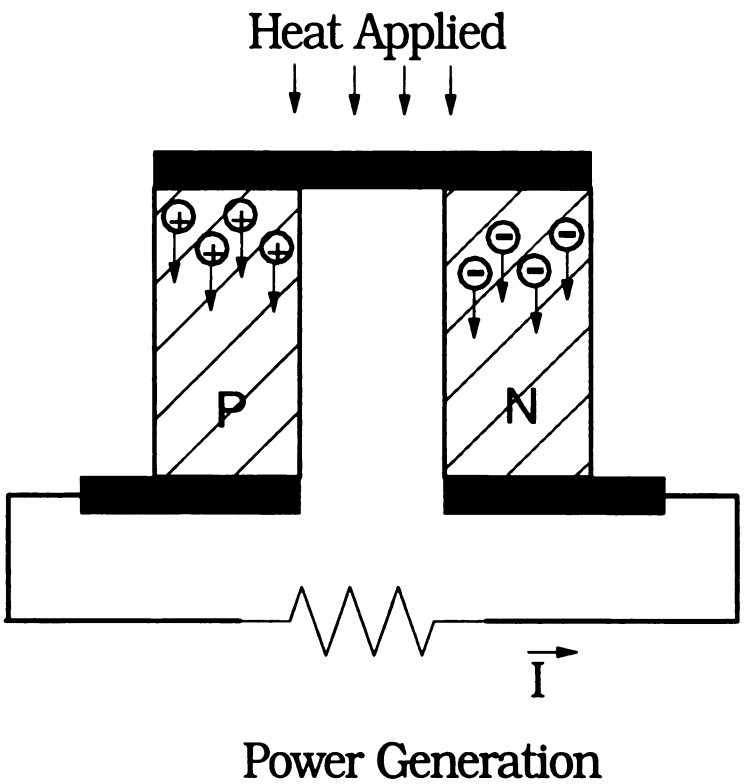

Figure 2.5 TE module for Power Generation.

The heat supplied is either conducted along the branches to the cold junction or used to balance the Peltier effect at the hot junction. Since the Joule heating is distributed throughout each of the *n* and *p* legs, one half of it flows back to the source. Thus,

$$Q = K\Delta T + S_{pn}\left(T_M + \frac{\Delta T}{2}\right)I - \tfrac{1}{2}I^2R \qquad (14.)$$

The Peltier effect is not associated with the nature of the contact between the two conductors, i.e. it is not related to "contact potential". The Peltier effect is different from the Joule heating in that Joule heating varies as the square of the current and directly as the electrical resistance of the conductor (I^2R). Moreover, Joule heating is a function of dimensions of the conductor and does not require a junction of dissimilar materials. Also,

in contrast to Peltier effect, Joule heating does not change its sign when the direction of the current is reversed since it is an irreversible phenomenon.

For maximum power output from a given couple the load resistance R_L should be made equal to the generator resistance R. The useful work is then,

$$W = \frac{S_{pn}{}^2 \Delta T^2}{4R} \tag{15.}$$

since half of the thermoelectric voltage appears across the load. The efficiency is

$$\eta = \frac{\Delta T}{2T_M + \frac{\Delta T}{2} + \frac{4RK}{S_{pn}{}^2}} \tag{16.}$$

More detail derivations for the COP of TE cooler and efficiency of power generator can be found in various sources [5, 6].

2.2 Why there is renewed interest in recent years

At room temperature, the best bulk TE material is Bismuth Telluride alloys where Bi_2Te_3 which was suggested by Goldsmid [7] about four decades ago. *ZT* is about 1 for this material at room temperature (its optimum temperature). Much effort and investigation had been directed toward optimizing the properties of bismuth telluride alloys but there has been only modest progress in finding a bulk material with higher *ZT*. The highest *ZT* in any bulk TE materials at about room temperature is 1.14 for p-type $(Bi_2Te_3)_{0.25}(Sb_2Te_3)_{0.72}(Sb_2Se_3)_{0.03}$ alloy [8]. Table 2.1 shows three typical TE materials for different temperature ranges. All of them have a *ZT* of about 1 at their optimum temperature:

	Z_{max} (K^{-1})	Useful Range
Bi_2Te_3	$3x10^{-3}$	< 500 K
PbTe	$1.7x10^{-3}$	< 900 K
Si-Ge	$1x10^{-3}$	< 1300 K

Table 2.1 Z of three typical TE materials.

Materials with *ZT* of about 4 or 5 are needed in order for a TE cooler to compete with the compressor-based refrigerator while *ZT* of 2 is predicted for thermoelectric systems to be useful in many applications such as automobiles and shipboard use.

A renewed interest in recent years follows the availability of new fabrication techniques, and the development of new theories predicting large increases in the efficiencies might be possible through quantum confinement.

2.2.1 Transport Theory: Optimizing *ZT* – the B factor

In 1993, Hicks and Dresselhaus [9] had shown that preparing material with superlattice (SL) structure should enhance *ZT*. They also suggested a *B* parameter in calculations to evaluate the effect of anisotropy on the figure of merit. This paper had delivered new prospective in TE research and suggested that more investigation could be done in searching for new TE materials.

The *B* parameter was first introduced by Chasmar and Stratton [10]. For bulk semiconductors, *ZT* is directly proportional to the *B* parameter and βE_G, which is the energy gap divided by the thermal energy, $ZT = F(B, \beta E_G)$, where $\beta = 1/kT$

$$B = \gamma \frac{1}{3\pi^2}\left(\frac{2k_B T}{h^2}\right)^{3/2} \sqrt{m_x m_y m_z}\, \frac{k_B^{\,2}}{e\kappa_l}\mu_x \qquad (17.)$$

where m is the effective mass of the carriers (electrons or holes) in the x, y, or z direction, and μ_x is the carrier mobility along the transport direction, x, and γ is the degeneracy of the bands for the carriers (electrons or holes) in the material. A high B factor translates to a high figure of merit, ZT.

This formula shows that highly anisotropic materials can be utilized to improve efficiencies if the highest mobility direction (the x-direction) can be chosen to correspond to the electrical current flow direction, while the effective masses of the other two directions are large. However, exploiting an anisotropic mass may run counter to attempts to increase the B factor through the band degeneracy term, γ.

Large band degeneracy can be obtained in materials where the band minima (conduction band) or the band maxima (valence band) is located in the Brillouin zone at points of low symmetry. This condition is generally found in highly symmetric crystal structures (i.e.: cubic) that contain a large number of atoms in the unit cell. Because of the requirement for high symmetry in the crystal structure, highly anisotropic effective masses of the carriers are not found in such materials. Thus attempts to increase the B factor through the γ term are generally in contrast with attempts to increase the B factor through exploiting the anisotropic mass. For instance, Bi_2Te_3 has a band degeneracy of $\gamma = 6$ as ellipsoidal band extrema.

Thus, in order to increase the value of Z, large effective masses, high carrier mobility and low lattice thermal conductivity is necessary. The value of ZT increases with βE_G until $\beta E_G \sim 10$. So for good thermoelectric materials, the optimal value of βE_G should be about 10, i.e. semiconductors with an energy gap of 10 kT [11]. The energy

gap can be obtained from appropriate band structure calculations. Table 2.2 shows the energy bandgap and the βE_G values of some typical TE materials.

Materials	E_g (eV)	T_M(K)	E_g/k_BT_M
Bi_2Te_3	0.16	300	9.7
PbTe	0.5	650	8.9
$AgSbTe_2$	0.3	650	5.4
GeTe	0.4	700	6.6
Si-Ge	0.7	1100	7.4

Table 2.2 Energy band gap of some good TE materials.

In the Boltzmann transport theory, thermopower can be expressed in the Mott equation [12]

$$S = \frac{\pi^2 k^2 T}{3e} \cdot \frac{d \ln \sigma(E)}{dE}\bigg|_{E=Ef} \tag{18.}$$

$\sigma(E)$ is the electrical conductivity and it is a function of Fermi energy, E_f. For bulk materials, if the electronic scattering is independent of energy, $\sigma(E)$ is simply proportional to the density of states (DOS) at $E = E_f$. The Mott equation shows us that S is a measure of the variation in $\sigma(E)$ above and below the Fermi surface, specifically through the derivative of the natural log of $\sigma(E)$. Since the thermopower is a measure of the asymmetry in electronic structure and scattering rates near the Fermi level, finding materials with electrical conductivities that have strong asymmetrical energy dependence in a small energy interval (a few kT) near E_f is a way to approach high thermopower.

Subsequently, this has lead to searching for complex structures and composition compounds. Furthermore, it has led to fabricating materials with 2D, 1D and 0D

structures due to the large value in $d\ln\sigma(E)/dE$ as can be seen through the density of states for each of these conditions (shown in Figure 2.6 below).

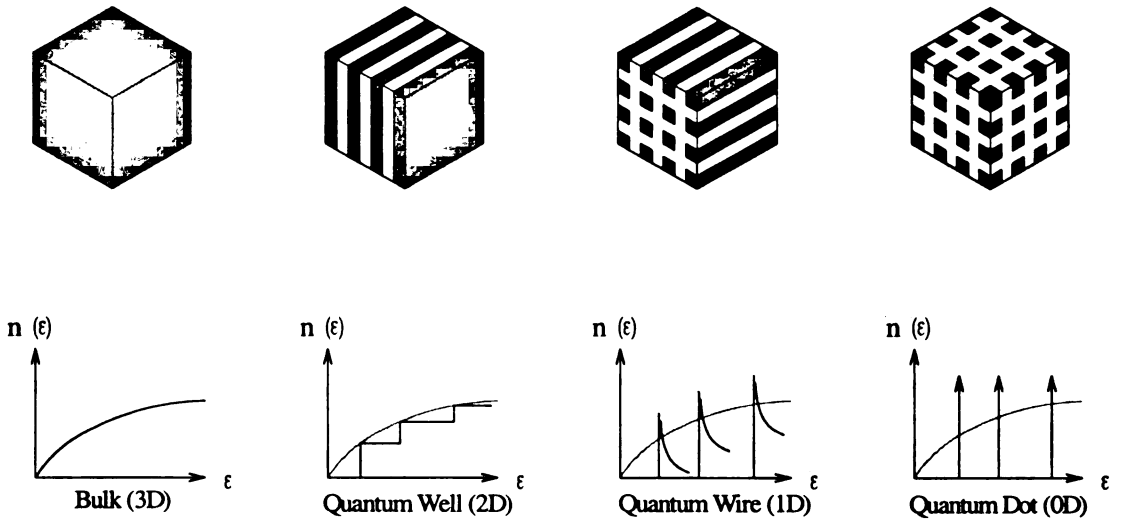

Figure 2.6 Density of states for different dimensionalities.

Another factor to achieve high ZT values is to have high mobility. As for a direct gap semiconductor, the conduction and valence bands are at the same point in k-space, this leads to small effective masses, thus high mobility. This is not desired for TE materials, because small effective masses will reduce the B factor. Actually, an indirect bandgap will be a better TE material.

We assume a quality factor, Q_f and it is depended on the degeneracy, effective masses and mobility,

$$Q_f = \gamma\sqrt{m_x m_y m_z}\,\mu_x$$

The best quality factor in semiconductors are achieved by silicon and germanium. These two elements are nonpolar because all atoms are alike, so the bonding is purely covalent. It is now important to introduce the concept of electronegativity, X, it is a

number which indicates an atom's tendency to take an electron away from another atom or to donate to the other atom.

In a binary solid composed of atoms A and B, an electronegativity difference of this compound is $\Delta X = X_A - X_B$. If this compound is a solid composed of cations and anions, it means that the atoms wish to trade electrons. In this case the solid is ionic and polar. Optical phonons tend to create long-range electric fields that scatter the electron strongly. Polar scattering by phonon makes a significant contribution to limiting the mobility of electrons. Silicon and germanium have high mobility because they lack polar scattering. They do have carriers scattered by optical phonons through other interactions, such as the deformation potential.

Slack [13] indicated that, for any TE materials composed of two or more elements, high mobility is achieved by having all of the atoms with similar values of electronegativity. Then the value of ΔX is small and the bonding is largely covalent. The small amount of ionic bonding means that polar scattering is weak and the mobilities should be large. This is the case for bismuth telluride, which has $<\Delta X> = 0.30$. Here $X_{Bi} = 2.02$ and $X_{Te} = 2.40$ and the average value of $<\Delta X>$ is found by averaging the number of bonds of different types.

2.2.2 New Materials and Material Synthesis Techniques

Progress in material synthesis methods, especially the advent in structure determination by x-ray diffraction [3], has been advanced in recent years and the new or improved synthesis techniques allow much more complex materials to be studied for TE applications. The polychalcogenide flux technique [14], which has been developed at

Michigan State University, has produced a large number of new and interesting TE materials [15, 16].

As reducing material dimensions will enhance the *ZT*, various chemical or physical deposition methods are developed to grow thin film and very encouraging results have been reported [17]. The combination of revised theories and the development of fabrication methods has helped in defining the path to search for higher efficiency TE materials.

2.2.3 Modern Technologies

All the above factors have, in a way, made this a good time to look for better TE materials, i.e. materials with high efficiency (high *ZT*). If new TE materials with high efficiency can be found and the fabrication cost is reasonable, the cooling industries will not be the only party benefiting. Other industries like IC fabrication will enjoy the more advanced active cooling since heat dissipation problem will be more significant in the coming century. To be able to use the waste heat from various sources including the internal combustion engine will make the current automobiles more efficient.

2.3 Enhancing *ZT*

In order to enhance the *ZT* of materials, either the Power Factor ($S^2\sigma$) of the materials should be increased or the thermal conductivity should be reduced, or both based on equation (1.). Increasing the Power Factor would seem like a better approach since the thermopower has more influence upon the *ZT* ($ZT \propto S^2$). However, for simple materials, increasing thermopower will lead to a simultaneous decrease in the electrical

conductivity. An increase in the electrical conductivity will results in increase to the electronic contribution in the thermal conductivity due to the Wiedeman-Franz (WF) law. Based on the WF law, for metal and metal alloys, the ratio of the thermal conductivity to electrical conductivity is a constant. So it is difficult to reduce one while increasing the other. In semiconductors, the ratio of the thermal conductivity to electrical conductivity has a higher value than the metals due to its lower electrical conductivity. However, Ioffe [18] showed that alloying the semiconductors could reduce this ratio.

In Section 2.2.1, we have described how large asymmetry electronic structure would give high thermopower based on transport theory. Generally if thermopower increases, so does the resistivity. This can be seen in the Mott equation (equation 18) when the substitution for $E_F/(kT)$ is made,

$$S = -\left[\left(\frac{5}{2} - s\right) - \frac{E_F}{kT}\right]\left(\frac{k}{e}\right)$$
$$= -\left(\frac{k}{e}\right)\left[\left(\frac{5}{2} - s\right) + \ln\left(\frac{N_C}{n}\right)\right] \qquad (19.)$$

while $\sigma = ne\mu$, where n is the carrier concentration, e is the charge of electron, and μ is the mobility. For traditional materials, the best compromise has been found in narrow gap, heavily doped (~ 10^{19} /cm^3) semiconductors. Figure 2.7 shows the variation of Figure of Merit, ZT, with carrier concentration.

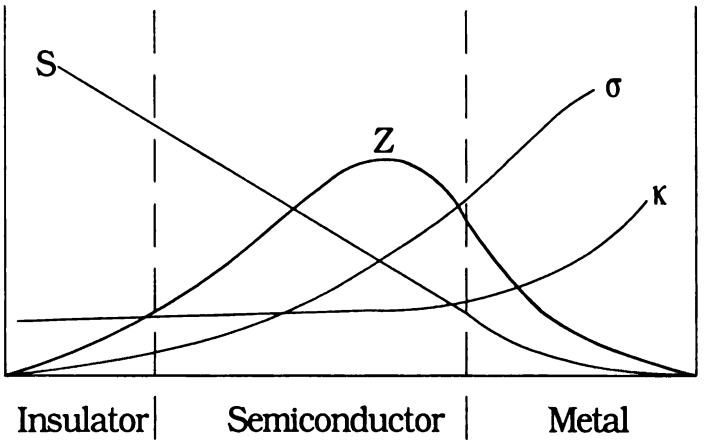

Figure 2.7 The variation of Figure of Merit ZT with carrier concentration

2.3.1 Minimizing Thermal Conductivity

Many researchers have also investigated avenues toward reducing the thermal conductivity of materials. Thermal conductivity of a semiconductor has two main components: the lattice (phonon) component (κ_l) and electronic component (κ_e), $\kappa = \kappa_e + \kappa_l$. The electronic thermal conductivity is $\kappa_e = L\sigma T$, where L is the Lorentz number, σ is the electrical conductivity, and T is temperature. In semiconductors, the Lorentz number L varies with the level of doping, reduced Fermi energy, $\xi = E_F/kT$, reduced energy band gap E_g/kT and the particular carrier scattering mechanisms.

Since the electronic thermal conductivity varies with the electrical conductivity, and in many semiconductors, κ_l is much greater than κ_e, it will be more effective to reduce the lattice contribution. These are some of the ways to approach minimizing κ_l:

1. The concept of "phonon glass electron crystal" (PGEC), which was suggested by Slack [13], is supported by various experimental results [25, 26, 27, 29, 30]. A proposed way for a material to exhibit PGEC behavior is for the material to

contain cages (or tunnels) in its crystal structure, in which atoms are allowed to "rattle". This situation produces a phonon damping effect that results in dramatic reduction of the solid's lattice thermal conductivity. It can be pictured as a loosely bound atom with a large thermal parameter scatters phonons much more strongly than electrons thus permitting a glass-like thermal conductivity to coexist with the high electron mobilities found in a crystal [19].

2. Another way is using compounds made from heavy elements such as antimony, bismuth, tellurium or lead. This is because high atomic masses can reduce the atomic vibrations frequencies (maintain in lower frequencies range, i.e. it has lower energy). So this large non-periodic mass fluctuation is introduced in the crystal lattice to lower the thermal conductivity. Unfortunately, low vibration frequencies also raise the electrical resistivity.

   Selenium, tellurium and antimony have another advantages in TE: they have a high value of polarizability. Compounds made with them have a large dielectric constant, thus a long scattering time. This contributed to strong screening of impurities, which increases the mobility. Atoms and ions with large atomic number have low thermal conductivity and high dielectric constant.

3. Having large number of atoms (N) in the unit cell or using alloys to prepare materials with complex structure. Since large N lowers the fraction of vibrational modes (phonons) that carry heat efficiently (the acoustic modes) to $1/N$. Large unit cell has larger lattice period and this will provide short mean free path-length for the heat carrying phonons.

4. The disorder of random atomic substitution in an alloy can also scatter the phonons, which reduces the thermal conductivity.

2.3.2 Properties of Good TE materials

Kanatzidis [19] has summarized that the best semiconductors for TE application have the following characteristics:

1. electronic bands near the Fermi level with many valleys preferably away from the Brillouin zone boundaries. This requires high symmetry. ($\uparrow S$, $\uparrow \mu$)
2. elements with large atomic number and large spin-orbit coupling. ($\downarrow \kappa$)
3. compositions with more than two elements (i.e. ternary, quaternary compounds) ($\downarrow \kappa$)
4. low average electronegativity difference between elements. ($\uparrow \mu$)
5. large unit cell size. ($\downarrow \kappa$)
6. energy gap equal to about 10 kT, where T is the operating temperature of the TE. For room temp operation this should be $0 < Eg < 0.3$ eV. ($\uparrow S$)

2.4 What is being done at MSU and other places

One way to categorize the TE research area is by the material type: uniform bulk materials and compositionally modulated films. Bulk materials can often be fabricated in large quantities using traditional methods such as direct solidification from a melt. While to produce modulated materials might require rather sophisticated process like chemical vapor deposition. Both types of materials have their own difficulties in fabrication

process and in optimizing their TE properties. To establish the goals for materials made at MSU and by the TE scientific community, Figure 2.8 shows some of the best TE materials which are currently under investigation.

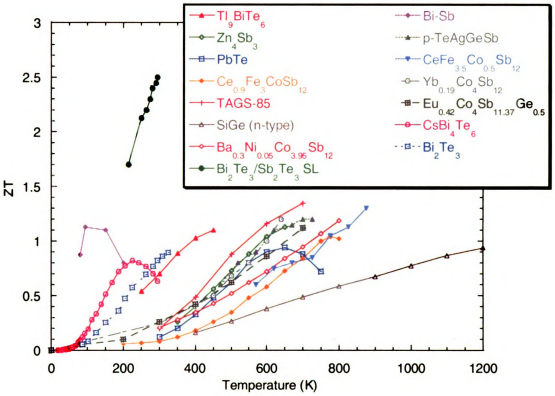

Figure 2.8 *ZT* of some best TE materials. (Images in this dissertation are presented in color.)

Bulk materials (Other locations than MSU)

2.4.1 Bismuth Telluride

Bismuth telluride is the most important TE material and it has the best *ZT* at room temperature. It is used in all devices that operate at or near to room temperature. This included all present refrigeration devices. It is usually alloyed with Sb_2Te_3, which has the same crystal structure. Alloying with Sb_2Te_3 can reduce the thermal conductivity to as low as $\kappa = 1$ W/mK. This low thermal conductivity is the main contribution in achieving

high *ZT*. Both *n*- and *p*-type materials have equally good properties. A single junction can cool down to a temperature of about 212 K if $T_h = 300K$. In practice, a single device cools slightly less than this ideal limit. However, a device with four to five stages can cool to well below 200K from room temperature.

Although, Bi_2Te_3 is often considered as a rhombohedric structure, it is easier to represent this structure as a layered crystal with hexagonal symmetry. The layers are stacked in a five-layer sequence (Te-Bi-Te-Bi-Te), which repeats itself; so two Te layers are adjacent on the boundaries of these units. Figure 2.9 shows the crystal structure of bismuth telluride.

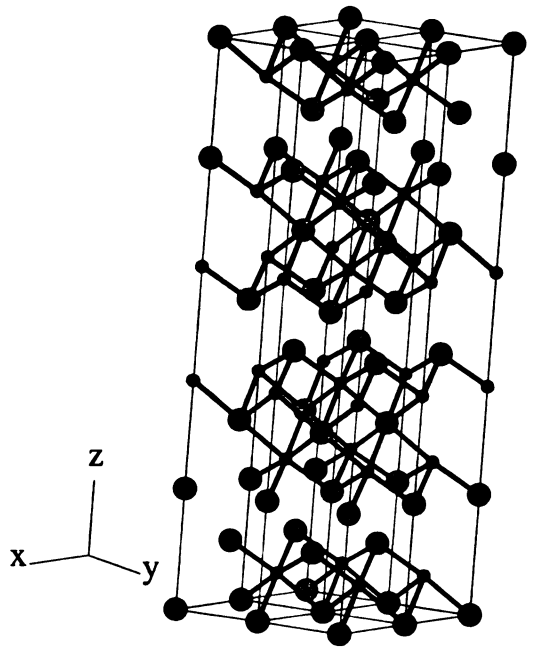

Figure 2.9 The crystal structure of bismuth telluride (Small circle indicates the bismuth atom and large circle indicates the tellurium atom).

Both conduction and valence bands have six equivalent minima. The ellipsoids are canted away from symmetry axes. The energy bands are nonparabolic, and the

effective masses are temperature dependent. A transport model is complicated due to the anisotropy and the nonparabolic, nonellipsoidal energy bands.

The energy band gap of pure Bi_2Te_3 is 0.16 eV [20], but this value increases when alloyed with Sb_2Te_3, and the device material has a gap of about 0.25 eV. Table 2.3 shows the different composition of bismuth telluride alloys. The composition of the commercial bismuth telluride alloys remain company secret as unknown doping is introduced to the compounds to optimize the properties.

Material	Z (10^{-3} K^{-1})	ZT	Type
$Bi_{24}Sb_{68}Te_{142}Se_6$	3.2	0.96	p
$Bi_{0.5}Sb_{1.5}Te_{3.13}$	3.0	0.90	p
$(Sb_2Te_3)_{72}(Bi_2Te_3)_{25}(Sb_2Se_3)_3$	3.4	1.02	p
$Bi_{1.75}Sb_{0.25}Te_{3.13}$	2.2	0.66	n
$(Sb_2Te_3)_5(Bi_2Te_3)_{90}(Sb_2Se_3)_5$	3.2	0.96	n

Table 2.3 The best TE materials at T=300K

2.4.2 IV-VI Semiconductors (PbS, PbSe, and PbTe)

PbS, PbSe, and PbTe all have NaCl structure. PbTe is a good TE material around 700K so it is used in TE generators. PbTe is a semiconductor with a small energy gap. At low temperature the gap is 0.19 eV. The gap increases with increasing temperature and equals 0.31 eV at T = 300K [11]. The standard alloy is $Pb_{1-x}Sn_xTe$. The best alloy is when x = 0.25, which has ZT > 1 near 800K. PbTe can be alloyed with a few tenths of 1% of sodium to make a p-type TE. Figure 2.10 shows the crystal structure of lead telluride.

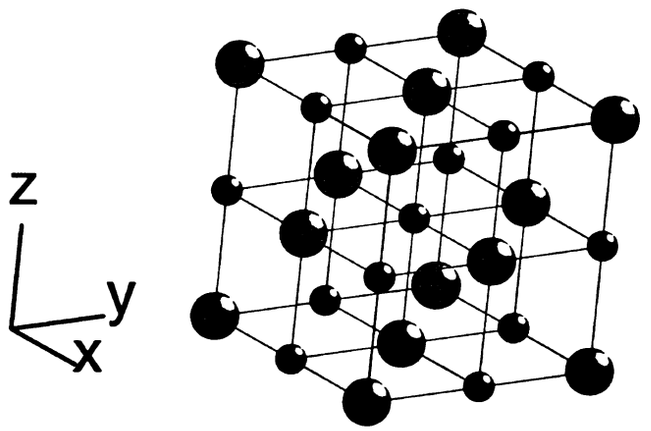

Figure 2.10 The crystal structure of lead telluride (Small circle indicates lead atom and large circle indicates tellurium atom).

2.4.3 Si-Ge

Silicon germanium alloys were first used in space in the SNAP-10A nuclear reactor and have been the exclusive choice for radioisotope thermoelectric generators launched by the U.S. since 1976. The operating temperature of the SiGe device can be up to 1300K without significant degradation. Satellites and space stations are often powered by thermonuclear TE generators. A spherical radioactive core serves as a source of heat. It is clad with layers of TE. Power is generated by the outward flow of heat. The inner layer is the warmest and uses Si-Ge alloys. The next layer uses PbTe for n-type and TAGS for p-types elements. Bi_2Te_3 is used for the last layer, near 300K.

The best mixture is $Si_{0.7}Ge_{0.3}$. The p and n-type SiGe can be produced by introducing boron and phosphorus doping respectively. The best n-type SiGe has a ZT of 0.9 at around 1200K. The best p-type SiGe has lower ZT of 0.5 at 1200K. The thermal expansion and mechanical strength considerations are critical to the design of the high temperature devices. Therefore these properties of SiGe alloys are studied to reduce the

stresses occur in the devices [21]. The thermal expansion of SiGe alloys range from 4 to $5x10^{-6}$/K in temperature 300-1400 K.

2.4.4 Bismuth Antimony

Bismuth has rhombohedral structure and is a semimetal with a carrier concentration of about $10^{18}/cm^{-3}$. In pure form it has a small but equal number of electrons and holes. A semimetal is due to band overlaps. The conduction band in one part of the Brillouin zone overlaps the valence band in another part. There are six electron ellipsoids, so the material is multivalley.

Alloying bismuth with group IV elements has introduced addition of donors or acceptors and this is expected to modify the band structure of bismuth as well as change the carrier concentration. However, the addition of group V elements can be expected to modify the band structure without destroying the equality of electron and hole concentration. Therefore, antimony is chosen due to it is similar to Bi and they form complete range of solid solutions [22]. Alloying with antimony raises the chemical potential and the hole pockets disappear. Then the material is n-type with a small energy gap between the chemical potential in the electron band and the top of the valence band. In this sense it becomes a narrow-gap semiconductor. The highest *ZT* is 0.6 and it is reached with 10-15% of Sb alloying with Bi. There is also a magnetothermoelectric effect. Some types of TE behavior are induced, or improved, by the application of magnetic field. In most cases, the application of magnetic field can make modest improvement in *ZT* for poor-TE materials but has no effect on materials that have high

ZT. Bi-Sb alloys are the exception to this general behavior. Magnetic fields can double the value of ZT to where it can achieve ZT>1 [23] (See Figure 2.8).

2.4.5 Skutterudites

Skutterudites are one of the families of compounds that are of great interest for thermoelectric applications. Skutterudite is a naturally occurring mineral, $CoAs_3$, first found in Skutterud, Norway. The structure is cubic and contains 32 atoms per unit cubic cell as shown in Figure 2.11. It poses an open, or cage-like, structure. When atoms are placed into the interstitial voids, or cages, of these materials, the lattice thermal conductivity can be substantially reduced compared to that of unfilled skutterudites.

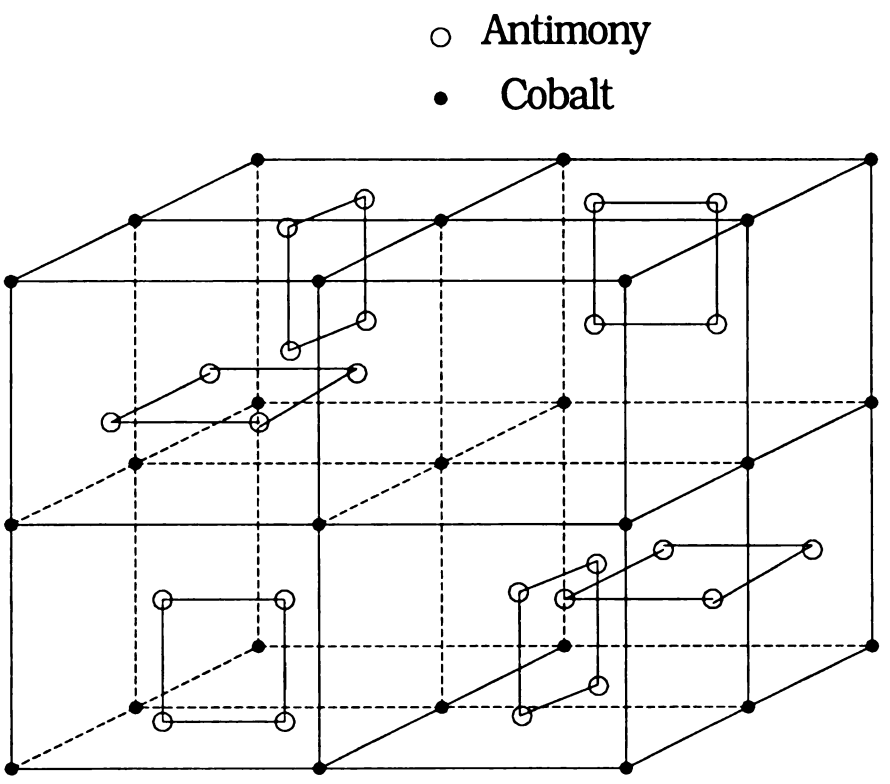

Figure 2.11 Schematic illustrating the unit cell of the unfilled skutterudite crystal structure [24].

Skutterudite materials meet the basic conditions for having high ZT values. These include a large unit cell, heavy constituent atom masses, low electronegativity differences between the constituent atoms, and large carrier mobilities [25]. Skutterudites can form covalent structures with low coordination numbers for the constituent atoms and can thus incorporate atoms in the relatively large voids formed in the lattice. The concept of phonon-glass electron-single-crystal says that heavy atoms should be introduced into the voids to lower the thermal conductivity of the sample. The basic families of these binary compounds are CoP_3, $CoAs_3$, $CoSb_3$ and etc. Ytterbium skutterudites (ZT~1 at 600K) and Eu-filled $CoSb_3$-based skutterudites ($ZT > 1$ at 700K) have been showed to have very high ZT [26, 27].

2.4.6 Clathrates

Clathrates are also called gas hydrates. Hydrates were discovered in 1810 by Sir Humphrey Davy, and were considered to be a laboratory curiosity. In the 1930s clathrate formation turned out to be a major problem, clogging pipelines during transportation of gas under cold conditions. Clathrates are crystalline solids which look like ice, and which occur when water molecules form a cage-like structure around smaller 'guest molecules'. The most common guest molecules are methane, ethane, propane, isobutane, normal butane, nitrogen, carbon dioxide and hydrogen sulfide, of which methane occurs most abundantly in natural hydrates. In clathrates, water crystallizes in the cubic system, rather than in the hexagonal structure of normal ice. Several different hydrate structures are known with one structure, known as Structure I, being the most common. In this structure the cages are arranged in body-centered packing; the unit cell contains 46 molecules of

water and up to eight molecules of methane [(CH_4). $5.75(H_2O)$], but not all cages are occupied [28].

The cage-like structure can also formed by group IV elements, for instance, X_8E_{46} where E is a group IV element and X is an atom in the voids (cages), formed by E. Nolas et al. [29, 30] have shown reduction of thermal conductivity in polycrystalline Ge ($ZT > 1$ at > 700K) and Sn clathrates with the voids filled with alkali-metal atoms. These materials have replaced the traditional alloy phonon scattering, which predominantly scatters the highest frequency phonons, by a much lower frequency "rattle" scattering. The highest frequency phonons have very low or zero group velocity and thus contribute little to the total thermal conductivity. The low frequency phonons have the highest group velocity and contribute most to thermal conductivity. This has explained why the impurities, alkali-metal atoms in this case, produce such significant reduction in thermal conductivity. Moreover, the high Seebeck coefficient and electrical conductivity of clathrate materials have made them of growing interest as potential thermoelectric materials.

The difference between skutterudites and clathrates systems is that in the skutterudites, the voids are present in the structure whether or not the "guest" atoms are present. Figure 2.12 shows the crystal structure of clathrates.

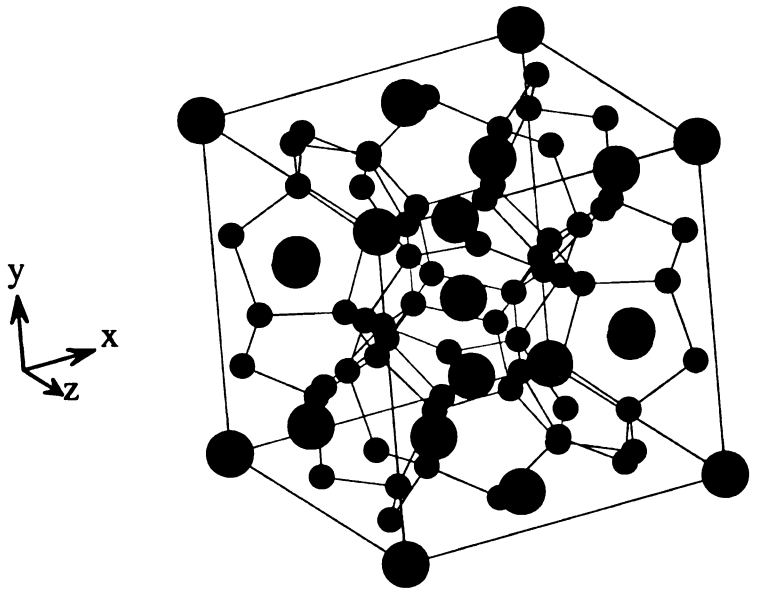

Figure 2.12 The crystal structure of clathrates (Small circle indicates GaSi atom and large circle indicates Ba atom).

2.4.7 Half-Heusler Alloys

Half-Heusler alloys are cubic materials (MgAgAs type) wih the general formula MNiSn where M is a group IV transition metal (Ti, Zr or Hf). Half- Heusler is formed by removing the Ni atoms on one of the two Ni sublattices of the full Heusler alloys MNi_2Sn and replacing them by an ordered lattice of vacancies.

Full Heusler alloys are metals but half-Heuslers alloys are intermetallics. It has a small gap in the density of states and a substantially semiconducting character. These materials exhibit a high negative thermopower (-40 to –250 μV/K) and low electrical resistivity values (0.1-8 m Ωcm). However, the thermal conductivity is rather high (~10 W/mK). Transport properties of Ti-based half-Heusler compounds ($TiNiSn_{1-x}Sb_x$) are investigated by Tritt's group [31]. It showed that by introducing very small amount of Sb doping to TiNiSn compounds, the electrical resisitivity can be reduced significantly.

Uher et al. [32] have shown that the transport properties of the half-Heusler compounds can be manipulated by annealing, isostructural alloying and doping. The thermal conductivity of some half-Heusler compounds can be reduced through these methods. Figure 2.13 shows the crystal structure of half-heusler alloy.

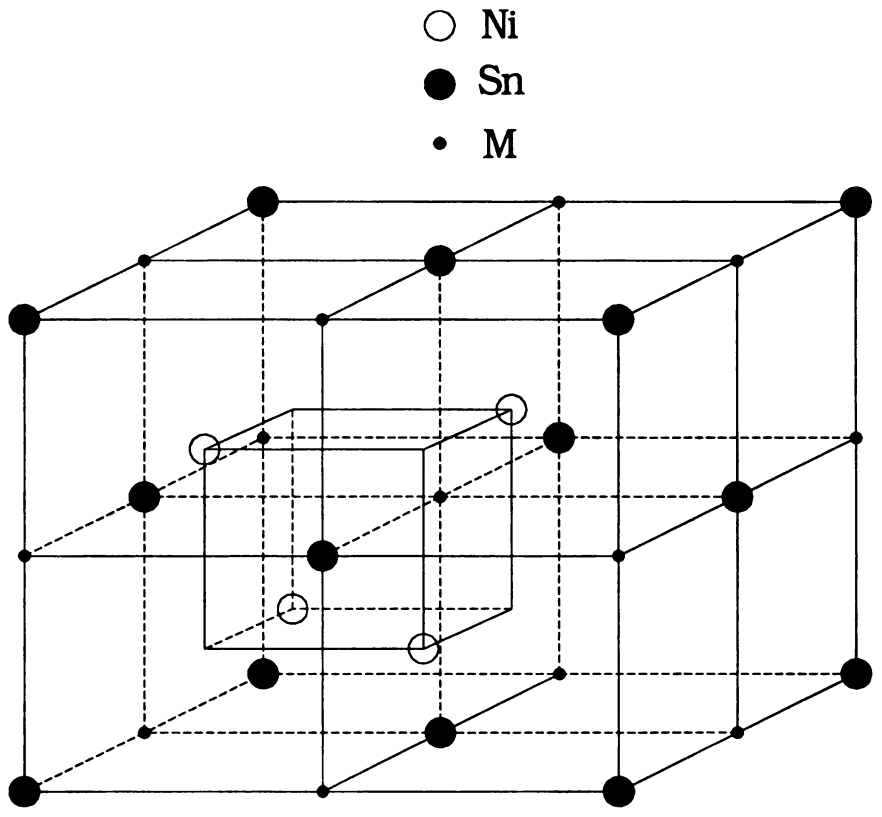

Figure 2.13 The crystal structure of Half-Heusler alloy.

2.4.8 TAGS

In the early 1960s, lead telluride, PbTe, was the standard material for TE application in space power supplies at high temperature. The n-type PbTe has very good stability and mechanical properties but the p-type PbTe has a number of weaknesses. This

has led to various studies in different doping on PbTe in order to improve the p-type materials. This is how TAGS materials were discovered.

$AgSbTe_2$ is a good TE by itself because it has low thermal conductivity. This is caused by silver ion disordering, as occurs in AgI and similar compounds. These four elements produce an excellent *p*-type TE at high temperature. They are usually represented as GeTe alloyed with $AgSbTe_2$. The best TE materials have 10-20% of $AgSbTe_2$.

Basic TAGS-type materials have general formula of $(AgSbTe_2)_{1-x}(GeTe)_x$ where T is tellurium, A is antimony, G is germanium and S is silver. Two of the famous materials are TAGS-80 and TAGS-85 [33], 80% and 85% of GeTe respectively. Actually, TAGS-80 (ZT~1.85 at 800K) exhibits better TE properties than TAGS-85 (ZT~1.35 at 700K) but the mechanical and stability problems of this composition has made TAGS-85 a preferable choice.

New materials in MSU

2.4.9 Chalcogenides – $CsBi_4Te_6$

One of the successful cases in creating new materials through the polychalcogenide flux technique is $CsBi_4Te_6$. Since β-$K_2Bi_8Se_{13}$ has shown promising TE properties and low thermal conductivity [34], there was an attempt to make the Te analog of this material with Cs. $CsBi_4Te_6$ was formed instead of the expected $Cs_2Bi_8Te_{13}$ and it exhibits a new structure.

The alkali metals (e.g. K and Cs) play an important role in lowering the thermal conductivity. In Figure 2.14, Cs^+ ions lie between the $[Bi_4Te_6]$ layer and they undergo

"rattling" to reduce the thermal conductivity. When doped appropriately, this material exhibits a high ZT below room temperature. $CsBi_4Te_6$ doped with various percentages of SbI_3 have shown some trend in power factor measurement. The sample doped with 0.05% of SbI_3 has the maximum ZT of about 0.8 at 225 K [35]. This material is air and water stable and melts without decomposition at 545 C. The crystals grow with long needle-like morphology. The direction of rapid growth along the needle axis is also the direction of the maximum TE performance.

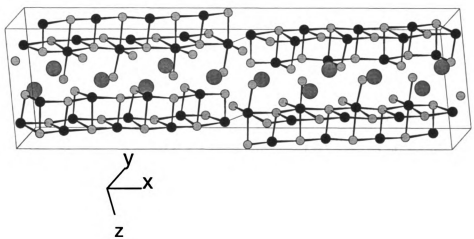

Figure 2.14 The crystal structure of $CsBi_4Te_6$ (Small gray circle indicates tellurium atom, small black circle indicates bismuth atom and large circle indicates Cs atom)

2.4.10 Cubic – $AgPbBiQ_3$ (Q = S, Se, Te)

The $AgPbBiQ_3$ class of compounds and their solid solution members are related to the NaCl structure type (or cubic structure), where Ag, Pb and Bi atoms are statistically disordered on the Na site and Q atoms occupy the Cl site [36]. These compounds were synthesized by combining the elements in appropriate ratio and heating under static vacuum at high temperature for days.

These materials are narrow band gap semiconductors with band gaps in the range of 0.6 to 0.28 eV. Their electrical conductivity is in the range of 70-400 S/cm, thermopower is from –40 to –160 μV/K (*n*-type) and they have extremely low thermal conductivity (<1.3 W/mK). The compounds $AgPbBiTe_3$, $AgPbBiSe_3$ and $AgPbBiTe_{2.75}Se_{0.25}$ and $AgPbBiTe_2Se$ were investigated.

More recently, the TE properties of this type of material have been enhanced and some of the measurement results are shown in the preliminary section.

Modulated materials

2.4.11 Quantum Well (Superlattice Structure)

When bulk TE materials seem to reach its limit in optimizing *ZT*, revised transport theory as stated in section 2.2.1 has suggested fabrication of 2D and 1D TE materials. A breakthrough was reached [17] when a p-type Bi_2Te_3/Sb_2Te_3 SL structure with *ZT* of 2.4 was fabricated and a temperature gradient of 32.2 K was measured from the device made by this material. The enhancement is achieved by controlling the transport of phonons and electrons in the SL. The SL structures are produced with various layer thickness, some are as small as 10 Å, using a low-temperature growth chemical vapor deposition (CVD) process [37, 38]. The thickness of the heterojunction layers influences the mobility of the samples. Materials with similar cross and in-plane mobilities as well as low thermal conductivity are chosen and *ZT* values were measured in devices using the Harman technique.

A QW is composed of a semiconductor with a narrow band gap sandwiched between two materials with larger band gaps. This configuration is called a type I

quantum well. Electrons and holes have their lowest energy states in the middle material and are usually confined to this region. Conducting particles such as electrons or holes are created in semiconductors by deliberately adding impurities that donate these carriers. In bulk 3D materials, the impurities scatter the carriers and impede their motion. In a QW, one can put the impurities in the barrier materials, so the conducting layer is free of impurities. Then the carriers in this layer have no impurities to limit their mobility. There are still phonons, but they are ineffective scatterers at low temperatures. This arrangement of impurities is called modulation doping.

Very high mobilities can be achieved in QW's by modulation doping. The hope is that a similar enhancement can be achieved for the Seebeck coefficient. However, in devices one will need to move bulk heat, which means that a multiple QW structure is desired. The fabrication cost of such devices is much higher than for bulk homogeneous materials and it is a challenge to fabricate homogenous QW structures.

2.4.12 Quantum Dots

Quantum dot superlattice (QDSL) structures have been investigated for application in thermoelectrics. This structure has a delta-function distribution of density of states and discrete energy levels due to three-dimensional quantum confinements. A test device that is made by PbSeTe/PbTe QDSL (grown by molecular beam epitaxy (MBE)) showed very large temperature gradients across the device [39]. This enhanced TE device performance and is believed to be almost entirely due to a high density of quantum nanodots with essentially 100% PbSe composition embedded in a 3D slab matrix of PbTe. The maximum temperature gradient for this device is 43.7 K. It is higher

than the previous reported value of 32.2 K for similar single one leg Bi_2Te_3/Sb_2Te_3 SL [17] (cross-plane current flow of SL and no QD) for an equivalent hot junction temperature.

2.5 Techniques of Characterization

Transport measurement of TE materials has been the main focus in the primary stage of my research. It is important to know the various properties of TE materials for they will tell us how good such materials are in TE performance, and help us to understand the materials to a level that we can improve upon them and develop them into devices.

After identifying materials with good TE properties, the investigation will be brought to the next stage – TE module/prototype fabrication.

Some of the characterization techniques will be reviewed followed by the set-up of the measurement system constructed for this research.

2.5.1 For Materials

Various techniques have been developed to measure the electrical and thermal properties of materials. Studying the advantages and disadvantages of these methods helps to design a better measurement system.

2.5.1.1 Steady-State Technique

The Steady-State method [40] is widely used for thermal conductivity measurements at low temperatures where the heat radiated from the sample is much smaller than the heat transported through the sample. Figure 2.15 shows the mounting configuration of this method.

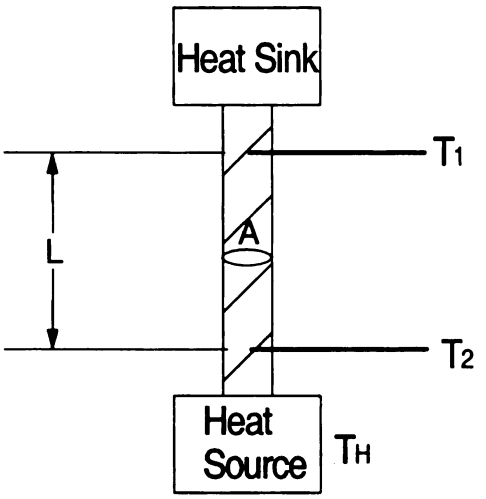

Figure 2.15 Stead-State Technique.

If all the heat supplied to the source Q (= $\partial q/\partial T$) is conducted along a sample of uniform cross section A and distance L between two thermocouples, then at any point, the thermal conductivity,

$$\kappa(T) = \frac{Q \cdot \partial L}{A \cdot \partial T} \tag{20.}$$

and the mean conductivity between points 1 and 2 separated by a distance L is

$$\kappa(T) = \frac{Q \cdot L}{A \cdot \Delta T} \tag{21.}$$

where ΔT is T_2-T_1

If the sample has high electrical conductivity, then the length of the sample should be sufficiently greater than the diameter. This helps to create a larger temperature gradient across the sample. For low conductivity materials, equilibrium times become very long so L/A ratio should be small.

The disadvantage of this technique is it requires a relatively long time for temperature stabilization and this long waiting time might also affect the precision of the measurement.

2.5.1.2 Harman Technique

The most common methods to measure thermal conductivity are the comparison method [41] and the absolute method [42]. In both methods, it is difficult to eliminate unnecessary heat transfer to the sample, especially in the case of small sample of low thermal conductivity. Therefore, Harman technique is introduced attempt to solve this problem.

Harman Technique [43] is a measurement of thermal conductivity by utilization of the Peltier effect. This measurement allows calculation of thermopower, thermal conductivity and electrical resistivity. A special feature of this method is that ZT is given in terms of the ratio of two voltages. Even though this method has been tested at 300K only, it should be able to be tested on low thermal conductivity materials of small dimension up to 1000K. The theory of this measurement is explained below, followed by descriptions of the experimental methods used.

I. Theory

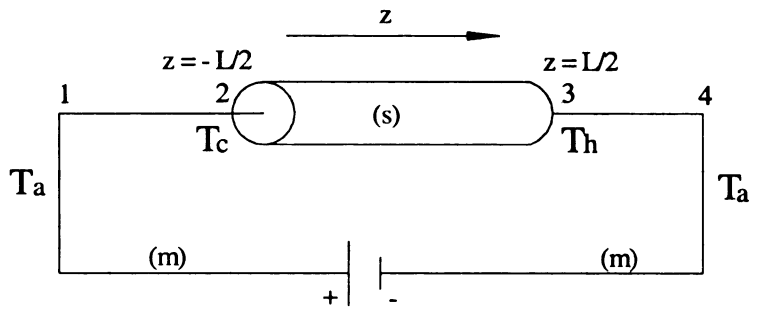

Figure 2.16 Cylindrical sample connecting to a circuit.

The basic circuit for this technique is in Figure 2.16. With direct current in the circuit, three principal phenomena will occur: Peltier effect, Joule heating and thermal conduction. Before the current is applied, it is assumed that there is no temperature gradient across the sample. By applying a current, I, through the sample, a temperature gradient is induced as caused by the Peltier heating at one end of the sample, and a subsequent Peltier cooling at the other end of the sample. Assuming it is a p-type material, the current is carrying heat from the cold junction ($z = - L/2$) at temperature T_c to the hot junction ($z = L/2$) at temperature T_h. The lead wires are maintained at the ambient temperature T_a.

The formal solution of this measurement can be derived in two parts. In the first part, the temperature distribution in a homogeneous cylinder satisfying appropriate boundary conditions is derived. In the second part, the energy balance at each junction ($z = \pm L/2$) is obtained, and the resulting equations combined to obtain the desired relation between the thermoelectric quantities.

i. Derivation of the temperature distribution

The continuity equation for the total energy flux, u, in steady-state is

$$\nabla \cdot u = 0 \tag{22.}$$

Energy flux is the rate at which energy passes through a fixed boundary per unit cross sectional area per unit time. The common unit is $J/(m^2s)$. From the consideration of irreversible thermodynamics, u is given for isotropic materials by

$$u = (\alpha T+\Lambda)j - \kappa \nabla T \tag{23.}$$

α is the thermopower, j is the current density, κ is the thermal conductivity and the gradient of electrochemical potential, Λ, is

$$\nabla \Lambda = -j\rho - \alpha \nabla T \tag{24.}$$

ρ is the electrical resistivity. If substituting (20) and (21) in (19) yields

$$j^2\rho - Tj \cdot \nabla \alpha = \nabla \cdot (-\kappa \nabla T) \tag{25.}$$

where $\nabla \cdot j = 0$, assuming charge concentration is stationary.

Under the conditions that the gradients of α, κ, ρ are small

$$\nabla^2 T = -j^2\rho/\kappa \tag{26.}$$

Equation 23 is the heat equation with uniform Joule heating in the sample, assuming the resistivity is independent of temperature.

In order to obtain a solution of the heat equation, we next consider the boundary conditions of this circuit. The sample is in right circular cylindrical shape with length L, radius a, and the lead-in wires are assumed to have sufficiently small cross section so that radiation loss may be neglected. The radiation flux $\sigma\varepsilon(T^4-T_a^4)$ is approximate to $4\sigma\varepsilon T^3(T-T_a)$ where σ is the Stefan-Boltzmann constant, ε is the surface emissivity and $T = (T_h+T_c)/2$. The energy flux in the neighborhood of the junction is assumed parallel to the cylindrical axis. This yields the following boundary conditions:

$$T(r,-L/2)=T_c \tag{27.}$$

$$T(r,L/2)=T_h \tag{28.}$$

$$-\kappa\left[\frac{\partial T(a,z)}{\partial r}\right]=h[T(a,z)-T_a] \tag{29.}$$

in cylindrical coordinate gives

$$\nabla^2 T=\left(\frac{\partial^2 T}{\partial r^2}\right)+\frac{1}{r}\left(\frac{\partial T}{\partial r}\right)+\left(\frac{\partial^2 T}{\partial z^2}\right)=-j^2\rho/\kappa \tag{30.}$$

By applying the boundary conditions (27-29) to the solution of equation 23, one obtains

$$T(r,z)-T_a$$
$$=\sum_{n=0}^{\infty}\frac{2\gamma}{(\lambda_n a)^2+\gamma^2}\left[\frac{T_h-T_c}{2}\frac{\sinh\lambda_n Z}{\sinh\lambda_n/2}+(\overline{T}-T_a-\frac{j^2\rho}{\lambda_n{}^2})\frac{\cosh\lambda_n z}{\cosh\lambda_n L/2}\right] \tag{31.}$$
$$\frac{J_0(\lambda_n r)}{J_0(\lambda_n a)}+\frac{j^2\rho a}{2h}\left[\frac{\gamma}{2}\left(1-\frac{r^2}{a^2}\right)+1\right]$$

where $h = 4\sigma\varepsilon T^3$, $\gamma = ha/\kappa$ and λ_n is a solution of $(\lambda_n a)J_1(\lambda_n a)= \gamma J_0((\lambda_n a)$.

In order that the approximation be accurate to 1%, it is necessary for T and T_a not to deviate from $T(avg)$ by more than 1/3 of 1%.

ii. Energy Balance at the Junctions

The total energy enters the sample at $z = -L/2$, is the sum of the energy current entering the sample and the radiation from the face of the sample. Thus the total energy, U_{sc} is

$$U_{sc} = 2\pi \int_0^a u_s(r,-L/2) r dr + \pi a^2 h(T_c - T_a) \tag{32.}$$

Combining equations 31 and 32 will result in equation 33, detail derivation can be found in Harman [43],

$$\begin{aligned} & I(\alpha_s - \alpha_m)\overline{T} = (K_m + K_s)(T_h - T_c) \\ & + \pi a(a + L/3)h(T_h - T_c)/2 + I^2 \Delta R_c \\ & \frac{-[(1/24) + (L^2/180a^2) + (a^2/48L^2) - 2aA/L][\pi a^2 h(T_h - T_c)]^2}{K_s \Delta T} \end{aligned} \tag{33.}$$

In equation 33, if the thermopower of the sample and lead wires, as well as the thermal conductivity of the lead wire are known. Thermal conductivity of the sample can be determined (calculated) from this equation, assuming we can measure the values of current, cold and hot temperature, dimension and emissivity.

Actually the emissivity can be obtained from equation 33 through measuring two samples with identical properties but different dimensions.

The factor involving contact resistance is eliminated experimentally by carrying out measurements for both directions of current.

II. Experimental Method

i. Measurement of Thermopower

Figure 2.16 shows material (m) in contact with sample (s). Point 1 and 4 are at the ambient temperature Ta and points 2 and 3 are at the temperature T_c and T_h respectively. The thermopower of the sample (s) relative to the material (m) is

$$\alpha_s - \alpha_m = \lim_{(Th-Tc)\to 0} \frac{V_4 - V_1}{T_h - T_c} \tag{34.}$$

If the material (m) is chromel, then equation 30 becomes

$$\alpha_s = \frac{V_\alpha}{\Delta T} = \pm\left[\frac{V_{\alpha-chr}}{\Delta T}\right] + \alpha_{chr} \tag{35.}$$

If the material (m) is alumel, then equation 30 becomes

$$\alpha_s = \frac{V_\alpha}{\Delta T} = \pm\left[\frac{V_{\alpha-alu}}{\Delta T}\right] + \alpha_{alu} \tag{36.}$$

V_α is the absolute Seebeck potential of the sample and $V_{\alpha-chr}$ is the thermal emf of a chromel-sample-chromel circuit. If the material (m) is alumel, then let the notation changes from 'chr' to 'alu'. Since these materials are used for thermocouples, their absolute thermopowers can be found from the literature. Thus, the thermopower of the sample can be easily obtained from measuring the voltage and temperature across the sample.

ii. Measurement of electrical resistivity and contact resistance

The measurement requires 8 wires attached to the sample as shown in Figure 2.17 The cylindrical sample is nickel plated on both ends and soldered to a chromel-alumel thermocouple and a copper current lead on each end. Two alumel wires are attached to the sample as voltage leads with a spacing of L'.

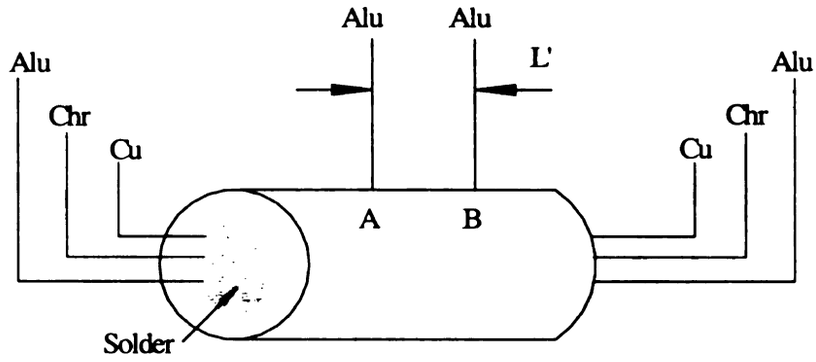

Figure 2.17. Harman technique circuit.

If the potential difference between the ends of the sample is $V_\rho+V_c$ and the between points A and B is V_ρ' when applying a current I, then the resistivity of the sample can be determined,

$$\rho = \frac{V_\rho' \pi a^2}{IL'} \tag{37.}$$

where a is the radius of the sample.

The total contact resistance is

$$R_c = \frac{V_\rho + V_c}{I} - \frac{\rho L}{\pi a^2} \tag{38.}$$

where L is the length of the sample.

iii. Measurement of thermopower and thermal conductivity

With the same configuration of the sample, thermopower and thermal conductivity can be obtained by addition of voltage method.

When a current is applying across the sample, a potential V_T exists. This potential is the sum of the IR drop due to sample resistance, the contact resistance and the Seebeck voltage of the sample and the lead wires.

Au

sample is

T

where V

current a

direction

irreversi

the total

dissimil

Combin

Equation

At steady-state, the total voltage across the two alumel leads on the ends of the sample is determined by the usual dc null method in the two current directions,

$$+V_T(alu)^+ = +V_\rho + V_c + V_{\alpha-alu} + V_{irr}(alu) \tag{39.}$$

$$-V_T(alu)^- = -V_\rho - V_c - V_{\alpha-alu} + V_{irr}(alu) \tag{40.}$$

The total voltage across the chromel leads in the two current directions is

$$+V_T(chr)^+ = +V_\rho + V_c + V_{\alpha-chr} + V_{irr}(chr) \tag{41.}$$

$$-V_T(chr)^- = -V_\rho - V_c - V_{\alpha-chr} + V_{irr}(chr) \tag{42.}$$

where $V_T(alu)^+$ is the total dc voltage across the two alumel leads in the plus direction of current and $V_T(alu)^-$ is the total dc voltage across the two alumel leads in the minus direction of current; so on for chromel leads. V_{irr} is a voltage across the sample which is irreversible with current and hence temperature gradient. It is less than a few percent of the total voltage and is believed to be due to unequal Joule heating in the vicinity of two dissimilar material junctions.

Equalize equations 35 and 36 gives

$$\alpha_{chr} - \alpha_{alu} = \alpha_{chr-alu} = \frac{V_{\alpha-alu} - V_{\alpha-chr}}{\Delta T} \tag{43.}$$

Combining equations 39 and 40 to obtain

$$V_{\alpha-alu} = V_\alpha - V_{alu} = \frac{V_T(alu)^+ + V_T(alu)^-}{2} - (V_\rho + V_c) \tag{44.}$$

Equation 44 becomes

$$V_\alpha = \pm\left[\frac{V_T(alu)^+ + V_T(alu)^-}{2} - (V_\rho + V_c)\right] + \alpha_{alu}\Delta T \qquad (45.)$$

Similarly,

$$V_\alpha = \pm\left[\frac{V_T(chr)^+ + V_T(chr)^-}{2} - (V_\rho + V_c)\right] + \alpha_{chr}\Delta T \qquad (46.)$$

The thermopower of the sample is thus

$$\alpha_s = \frac{V_\alpha}{\Delta T} \qquad (47.)$$

and the thermal conductivity is

$$\kappa = \frac{\alpha_s I \overline{T}}{\Delta T} \cdot \frac{L}{\pi a^2} \qquad (48.)$$

where $\overline{T}$ is the average temperature. As we know $Z=\alpha^2/\kappa\rho$, and by substituting the equations 38, 47 and 48, the figure of merit Z can be determined from a ratio of two voltages,

$$Z = \frac{V_\alpha}{V_\rho \overline{T}} \qquad (49.)$$

2.5.1.3 Pulse Technique

Pulse technique is a method for measurement of thermoelectric power and thermal conductivity simultaneously at low temperatures [44]. It is very similar to the steady-state technique but doesn't require a long waiting time. This is an AC method

used to avoid rapid temperature drift; the heat current, which is used to create a thermal gradient across the sample, is pulsed with a square wave.

This method will produce piecewise exponential signals for the temperature gradient and voltage across the sample. These signals are used to obtain the thermopower and thermal conductivity of sample.

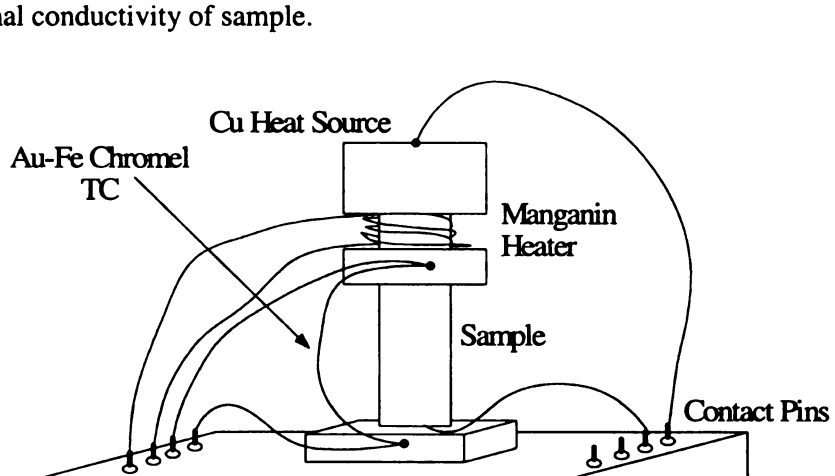

Figure 2.18 Pulse Technique experimental set-up.

The high speed of this technique also allows the accumulation of a high density of data points. For long pulse times, this method reaches steady-state where it is the same as the technique described in section 2.5.1.1. For shorter pulse times this method does not reach steady-state temperature gradient and the thermal conductivity of the sample should be extracted from the data as discussed below.

Figure 2.18 has shown the measurement set-up of the pulse technique, a sample with thermal conductance, K, is sandwiched between a heat source with $T_1(t)$ and a heat bath with $T_0(t)$. When a current is applied to the sample, the heat equation can be written as

$$\dot{Q} = C(T_1)\dot{T}_1 = R(T_1)I^2(t) - K(T_1 - T_0) \tag{50.}$$

where $\dot{Q}$ is the amount of heat per unit time accumulated at the heat source, $C(T_1)$ is the heat capacity of the heat source and $R(T_1)$ is the resistance of the heater. The amount of heat is balanced between the current dissipated by the heater and heat conducted by the sample.

The temperature difference, $\Delta T = (T_1 - T_0)$, is usually made small with respect to the mean temperature, $\overline{T} = (T_1 + T_0)/2$, so the thermal conductance can be considered as a function of mean temperature. If the bath temperature stays constant and a constant current I_0 is applied through the heater, after a sufficient long time, a steady state is reached and thus $\dot{T}_1 = 0$ and the thermal conductance becomes

$$K(\overline{T}) = \frac{I^2 R(T_1)}{T_1 - T_0} \tag{51.}$$

If the bath temperature is let to drift slowly, and a periodic square-wave current with period 2 is applied thought the resistance,

$$I(t) = \begin{cases} 0 & if \quad t \mod 2\tau < \tau \\ I_0 & if \quad t \mod 2\tau \geq \tau \end{cases} \tag{52.}$$

then the system will no longer reach steady state and the temperature T_1 of the heat source will also be an oscillating function of time. Figure 2.19 shows the periodic waveform of the current supplied to the sample. The condition t mod 2τ gives the remainder after t is divided by 2τ. The mathematics equations that will be performed now will further explain how the technique is used to obtain the conductance K as a function

of temperature from the amplitude of the measured signal T_1, if the $C(T)$ and $R(T)$ are known. The heat equation needed to be solved in this case.

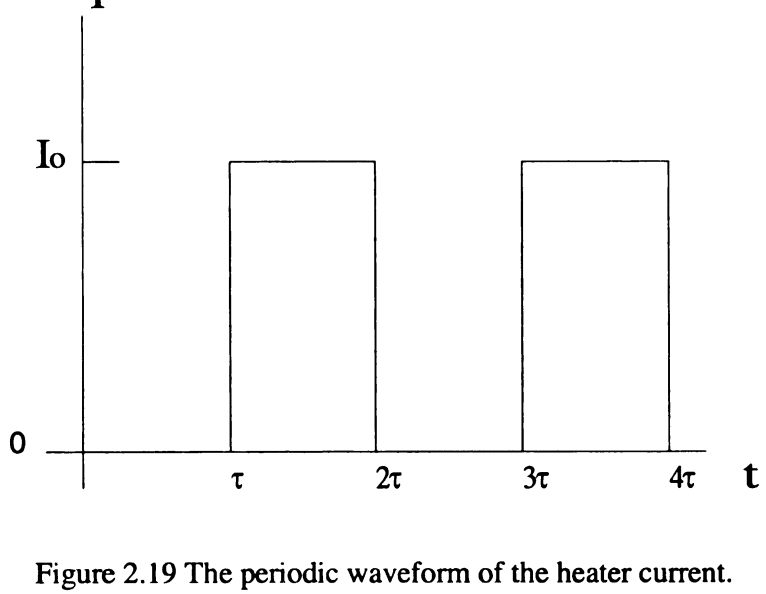

Figure 2.19 The periodic waveform of the heater current.

Some assumptions needed to be made to solve the heat equation. Since ΔT is small, we can approximate T_1 to T_0, and we can assume $C(T)$, $R(T)$ and $K(T)$ to be constant. T_0 can be considered to be constant as far as the bath temperature drift slowly. If the drift is slow compared to the time scale that is used to modulate the current, then it is possible to solve the heat equation.

Equation 50 becomes

$$\dot{T}_1 = \frac{R}{C} I^2(t) - \frac{K}{C}(T_1 - T_0) \tag{53.}$$

Subtracting both sides by $\dot{T}_0$, gives

$$\dot{T}_1 - \dot{T}_0 = \frac{R}{C} I^2(t) - \frac{K}{C}(T_1 - T_0) - \dot{T}_0 \tag{54.}$$

Equation 54 can be written as

$$\frac{d}{dt}(\Delta T)+\frac{K}{C}\Delta T=\frac{R}{C}I^2(t)-\dot{T}_0(t) \tag{55.}$$

Equation 55 is a linear first order differential equation and can be expressed as

$$\frac{d}{dt}(\Delta T)+\frac{K}{C}\Delta T=f(t) \tag{56.}$$

where

$$f(t)=\frac{R}{C}I^2(t)-\dot{T}_0 \tag{57.}$$

If we let $f(t) = 0$, equation 56 becomes

$$\frac{d}{dt}(\Delta T)=-\frac{K}{C}\Delta T \tag{58.}$$

rearrange equation 58 gives

$$\frac{d}{\Delta T}(\Delta T)=-\frac{K}{C}dt \tag{59.}$$

Integrating both sides in equation 59 gives

$$\ln(\Delta T)=-\int\frac{K}{C}dt+c_1=-\frac{K}{C}t+c_1 \tag{60.}$$

or

$$\Delta T=e^{-\frac{K}{C}t+c_1}=const.*e^{-\frac{K}{C}t} \tag{61.}$$

where c_1 is the integration constant and $const.= e^{c_1}$. Combining equation 61 and 56 gives

$$\frac{d}{dt}\left(\Delta Te^{\frac{K}{C}t}\right)=e^{\frac{K}{C}t}\left(\frac{d}{dt}(\Delta T)+\frac{K}{C}\Delta T\right)=e^{\frac{K}{C}t}f(t) \tag{62.}$$

Integrating equation 62 gives

$$\Delta T e^{\frac{K}{C}t} = \int e^{\frac{K}{C}t} f(t)dt = \int e^{\frac{K}{C}t}\left(\frac{R}{C}I^2(t) - \dot{T}_0(t)\right)dt \tag{63.}$$

$$\Delta T e^{\frac{K}{C}t} = \int e^{\frac{K}{C}t}\frac{R}{C}I^2(t)dt - \int e^{\frac{K}{C}t}\dot{T}_0(t)dt + c_2 \tag{64.}$$

If we let $t = t_1$, then

$$\Delta T = \int_0^{t_1} e^{\frac{K}{C}(t-t_1)}\frac{R}{C}I^2(t)dt - \int_0^{t_1} e^{\frac{K}{C}(t-t_1)}\dot{T}_0(t)dt + c_2 e^{-\frac{K}{C}t_1} \tag{65.}$$

The second term in equation 65 can be approximated by

$$\int_0^{t_1} e^{\frac{K}{C}(t-t_1)}\dot{T}_0(t)dt \approx \frac{C}{K}\dot{T}_0(t)e^{\frac{K}{C}(t-t_1)}\Big|_0^{t_1} = \frac{C}{K}\left(\dot{T}_0(t_1) - \dot{T}_0(0)e^{-\frac{K}{C}t_1}\right) \tag{66.}$$

if we assume $\dot{T}_0$ varies very slowly with time and it can be considered as a constant but still include the limits of the integration (an adiabatic approximation). The first term in equation 65 then becomes

$$\int_0^{t_1} e^{\frac{K}{C}(t-t_1)}\frac{R}{C}I^2(t)dt = \frac{R}{C}\left[\int_0^{\tau} 0\cdot e^{\frac{K}{C}(t-t_1)}dt + \int_{\tau}^{2\tau} I_0^2 e^{\frac{K}{C}(t-t_1)}dt\right. \tag{67.}$$

$$+ \int_{2\tau}^{3\tau} 0\cdot e^{\frac{K}{C}(t-t_1)}dt + \int_{3\tau}^{4\tau} I_0^2 e^{\frac{K}{C}(t-t_1)}dt + \ldots$$

$$\left. + \int_{\left[\frac{t_1}{\tau}\right]\tau}^{t_1} I^2(t_1)\cdot e^{\frac{K}{C}(t-t_1)}dt\right]$$

$\left[\frac{t_1}{\tau}\right]$ is the integer part of t_1/τ and t_1 is in term of τ. For t_1 mod $2\tau < \tau$, equation 67

becomes

$$\frac{R}{C}\int_0^{t_1} e^{\frac{K}{C}(t-t_1)} I^2(t)dt = \frac{R}{C}\int_0^{t_1} e^{-\frac{K}{C}(t_1-t)} I^2(t)dt$$

$$= \frac{R}{C}\frac{C}{K} I_0^2 \left(e^{-\frac{K}{C}(t_1-2\tau)} - e^{-\frac{K}{C}(t_1-\tau)} + e^{-\frac{K}{C}(t_1-4\tau)} - e^{-\frac{K}{C}(t_1-3\tau)} + \ldots \right. \quad (68.)$$

$$\left. + e^{-\frac{K}{C}\left(t_1-\left[\frac{t_1}{\tau}\right]\tau\right)} - e^{-\frac{K}{C}\left(t_1-\left[\frac{t_1}{\tau}-1\right]\tau\right)} \right)$$

Since $t_1 = t_1 \bmod \tau + \left[\frac{t_1}{\tau}\right]\tau$ {This equation can be understood better by giving an example, let t_1 = 23s and τ= 5s, so 23 =3 + 4τ }, taking the factor (t_1 mod τ) out from the right side of equation gives

$$\frac{R}{C}\int_0^{t_1} e^{-\frac{K}{C}(t_1-t)} I^2(t)dt =$$

$$\frac{R}{K} I_0^2 e^{-\frac{K}{C}(t_1 \bmod \tau)} \left(e^{-\frac{K}{C}\left(\left[\frac{t_1}{\tau}\right]\tau-2\tau\right)} - e^{-\frac{K}{C}\left(\left[\frac{t_1}{\tau}\right]\tau-\tau\right)} + e^{-\frac{K}{C}\left(\left[\frac{t_1}{\tau}\right]\tau-4\tau\right)} \right. \quad (69.)$$

$$\left. - e^{-\frac{K}{C}\left(\left[\frac{t_1}{\tau}\right]\tau-3\tau\right)} + \ldots e^{-\frac{K}{C}\left(\left[\frac{t_1}{\tau}\right]\tau-\left[\frac{t_1}{\tau}\right]\tau\right)} - e^{-\frac{K}{C}\left(\left[\frac{t_1}{\tau}\right]\tau-\left[\frac{t_1}{\tau}-1\right]\tau\right)} \right)$$

$$\frac{R}{C}\int_0^{t_1} e^{-\frac{K}{C}(t_1-t)} I^2(t)dt =$$

$$\frac{R}{K} I_0^2 e^{-\frac{K}{C}(t_1 \bmod \tau)}\left(e^{-\frac{K}{C}\left(\left[\frac{t_1}{\tau}-2\right]\tau\right)} - e^{-\frac{K}{C}\left(\left[\frac{t_1}{\tau}-1\right]\tau\right)} + e^{-\frac{K}{C}\left(\left[\frac{t_1}{\tau}-4\right]\tau\right)} - e^{-\frac{K}{C}\left(\left[\frac{t_1}{\tau}-3\right]\tau\right)} + \ldots \right. \tag{70.}$$

$$\left. 1 - e^{-\frac{K}{C}\tau} \right)$$

In equation 70, the alternating addition and subtraction terms will cancel each other and only the last two terms will remain. Multiplying the numerator and denominator by $1+e^{-\frac{K}{C}\tau}$ will give

$$\frac{R}{C}\int_0^{t_1} e^{-\frac{K}{C}(t_1-t)} I^2(t)dt = \frac{R}{K} I_0^2 e^{-\frac{K}{C}(t_1 \bmod \tau)}\left(\frac{\left(1-e^{-\frac{K}{C}\tau}\right)\left(1+e^{-\frac{K}{C}\tau}\right)}{1+e^{-\frac{K}{C}\tau}} \right) \tag{71.}$$

$$\frac{R}{C}\int_0^{t_1} e^{-\frac{K}{C}(t_1-t)} I^2(t)dt = \frac{R}{K} I_0^2 e^{-\frac{K}{C}(t_1 \bmod \tau)}\left(\frac{1-e^{-\frac{K}{C}2\tau}}{1+e^{-\frac{K}{C}\tau}} \right)$$

$$= \frac{R}{K} I_0^2 e^{-\frac{K}{C}(t_1 \bmod \tau)}\left(\frac{1-e^{-\frac{K}{C}\left[\frac{t_1}{\tau}\right]\tau}}{1+e^{-\frac{K}{C}\tau}} \right) \tag{72.}$$

For $t_1 \bmod 2\tau \geq \tau$, equation 67 becomes

$$\frac{R}{C}\int_0^{t_1} e^{-\frac{K}{C}(t_1-t)} I^2(t)dt$$

$$= \frac{R}{C}\frac{C}{K} I_0^2 \left(e^{-\frac{K}{C}(t_1-2\tau)} - e^{-\frac{K}{C}(t_1-\tau)} + e^{-\frac{K}{C}(t_1-4\tau)} - e^{-\frac{K}{C}(t_1-3\tau)} + \ldots \right. \quad (73.)$$

$$\left. + e^{-\frac{K}{C}(t_1-t_1)} - e^{-\frac{K}{C}\left(t_1-\left[\frac{t_1}{\tau}\right]\tau\right)} \right)$$

taking the factor t_1 mod τ out from the right side of equation 73 gives

$$\frac{R}{C}\int_0^{t_1} e^{-\frac{K}{C}(t_1-t)} I^2(t)dt = \frac{R}{K} I_0^2 \left(1 + e^{-\frac{K}{C}(t_1 \bmod \tau)} \right)$$

$$\left(e^{-\frac{K}{C}\left(\left[\frac{t_1}{\tau}\right]\tau - 2\right)} - e^{-\frac{K}{C}\left(\left[\frac{t_1}{\tau}\right]\tau - 1\right)} + e^{-\frac{K}{C}\left(\left[\frac{t_1}{\tau}\right]\tau - 4\right)} - e^{-\frac{K}{C}\left(\left[\frac{t_1}{\tau}\right]\tau - 3\right)} + \ldots - 1 \right) \quad (74.)$$

In equation 74, the alternating addition and subtraction terms will cancel each other and only the last two terms will remain. Multiplying the numerator and denominator with $1 + e^{-\frac{K}{C}\tau}$ will give

$$\frac{R}{C}\int_0^{t_1} e^{-\frac{K}{C}(t_1-t)} I^2(t)dt = \frac{R}{K} I_0^2 \left(1 - e^{-\frac{K}{C}(t_1 \bmod \tau)} \right) \left(\frac{1 + e^{-\frac{K}{C}\left[\frac{t_1}{\tau}\right]\tau}}{1 + e^{-\frac{K}{C}\tau}} \right) \quad (75.)$$

Combining equations 66, 72 and 75 and substituting into equation 65 gives

$$\Delta T = \Delta T(0)e^{-\frac{K}{C}t} - \frac{C}{K}\left(\dot{T}_0(t) - \dot{T}_0(0)e^{-\frac{K}{C}t}\right)$$
$$+\frac{R}{K}I_0^2\begin{cases} e^{-\frac{K}{C}(t \bmod \tau)}\left(\dfrac{1-e^{-\frac{K}{C}\left\lfloor\frac{t}{\tau}\right\rfloor\tau}}{1+e^{-\frac{K}{C}\tau}}\right) & \text{if } t \bmod 2\tau < \tau \\ 1-e^{-\frac{K}{C}(t \bmod \tau)}\left(\dfrac{1+e^{-\frac{K}{C}\left\lfloor\frac{t}{\tau}\right\rfloor\tau}}{1+e^{-\frac{K}{C}\tau}}\right) & \text{if } t \bmod 2\tau \geq \tau \end{cases} \quad (76.)$$

The solution has a saw-tooth waveform as shown in Figure 2.20.

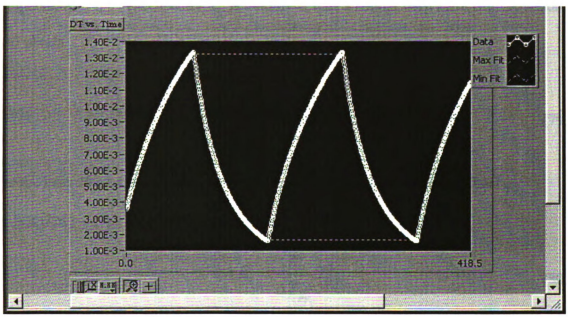

Figure 2.20 The waveform of the temperature gradient across the sample.

The maxima occur at $t = n\tau$ with n even and the minima with n odd. If $t = n\tau$ then $t \bmod \tau = 0$ and $\tau\lfloor t/\tau \rfloor = t$. The temperature gradient is obtained by taking the difference between the maximum and minimum curves,

$$\Delta T_{pp} = \frac{R}{K} I_0^2 \left(\frac{1 - e^{-(\frac{K}{C})t}}{1 + e^{-(\frac{K}{C})\tau}} - 1 + \frac{1 + e^{-(\frac{K}{C})t}}{1 + e^{-(\frac{K}{C})\tau}} \right)$$
$$= \frac{R}{K} I_0^2 \tanh\left(\frac{K\tau}{2C} \right) \quad (77.)$$

Rewrite the equation will let us obtain the thermal conductance

$$K = \frac{R}{\Delta T_{pp}} I_0^2 \tanh\left(\frac{K\tau}{2C} \right) \quad (78.)$$

K can be solved by numerical iteration if all the other parameters are known as a function temperature. If the heat capacity, *C*, is unknown, then a similar derivation from equation will obtain

$$C = \frac{2R}{(\partial T / \partial t)_{pp}} I_0^2 \left(\frac{1}{1 + e^{-(\frac{K}{C})\tau}} \right) \quad (79.)$$

For the case when τ is much greater than the system relaxation time *C*/*K*, then $\tanh(K\tau/2C) \sim 1$, so the thermal conductance becomes

$$K = \frac{R}{\Delta T_{pp}} I_0^2 \quad (80.)$$

This is the same result one achieves for the steady-state technique described in section 2.5.1.1.

2.5.1.4 High Temperature Transport Probe

This system is developed to measure the power factor of material as a function of temperature over a range of 80-700K [45]. The system is considered as a high

temperature probe, consists of two stainless steel half cylinders which are bolted together and separated by a thin sheet of machinable ceramic, Macor. A 100 Watt heater is inserted into each half cylinder. Each heater is independently controlled to establish $T+\Delta T/2$ and $T-\Delta T/2$. On the top faces of the half-cylinders are thick quartz substrates which are attached with silver paint. The sample is mounted laterally across the surfaces of the substrates with silver paint. Type K thermocouples are attached at each end of the sample while two platinum wires are attached just inside each of the sample ends. Figure 2.21 shows the sample stage of this system.

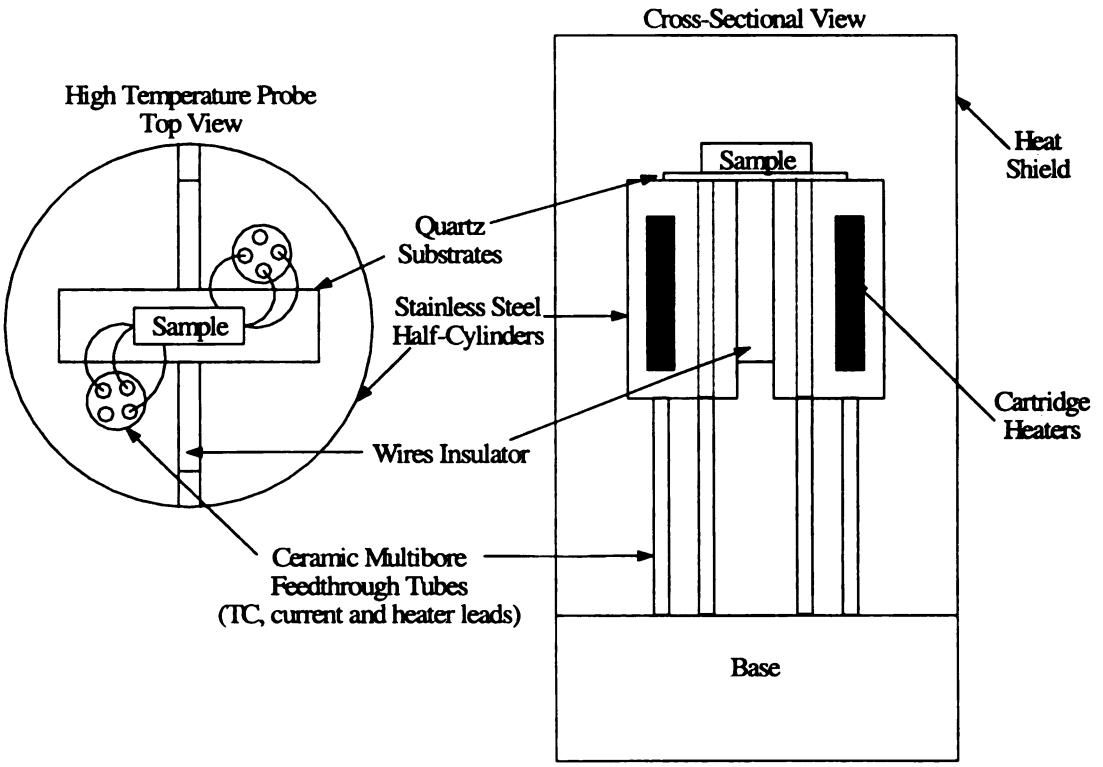

Figure 2.21 High Temperature Transport Probe Sample Stage.

A possible disadvantage of this sample configuration, is that the sample is mounted laterally on the surface, where for thicker samples, an additional temperature

gradient can occur from the top surface of the sample to the bottom of the sample. This might affect the accuracy of the measurement.

2.5.1.5 Parallel Thermal Conductance (PTC) Technique

This method is also a variation of steady-state technique [46]. It is developed in order to measure the thermal conductivity of small samples. Most other measurement technique requires mounting a heater, a differential thermocouple (or two single ended thermocouples) to the sample. If the sample is very small, the mounting job becomes difficult and if the sample is fragile, it might be too weak to support the weight of the heater.

In the PTC method, a sample holder or stage is made to support the small sample. A heater and thermocouples are mounted on the support post and the sample is simply attached to the post with paste. This method consists of three steps. Step1 is to measure the preliminary thermal conductance of the sample holder itself, which determines the base line or background thermal conduction and losses associated with the sample stage. Step 2 is to measure the thermal conductance of the whole system after attaching the sample to the sample stage. The parallel thermal conductance can be obtained after subtracting the value of Step 2 from Step 1. The last step is to disconnect the sample from the base (but not from the sample holder hat) and measure the thermal conductance. If we subtract this value from step 1, we can determine the radiation losses due to the sample itself. A 0.5 correction factor is introduced for the estimated radiation losses. Figure 2.22 shows the sample configuration of PTC technique.

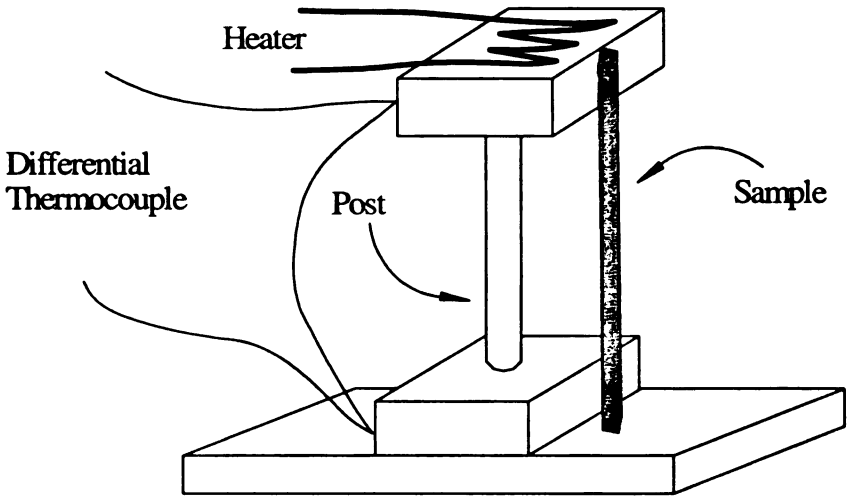

Figure 2.22 Sample holder with sample.

2.5.1.6 Low-Temperature 4-sample Thermoelectric Measurement System

This automated system is a well-established low-temperature (80-400K) thermoelectric measurement system that is developed in our lab [47]. The system is capable to measure the thermopower, electrical conductivity and thermal conductivity of four samples simultaneously.

The measurement method and sample configuration (shown in Figure 2.23) are variation of the pulse technique. A copper – constantan differential thermocouple is used for measuring the temperature gradient, and thermally connected to the sample using GE varnish. A surface mount resistor (470 Ω) is used to periodically heat one end of the sample to establish a temperature gradient of < 1K between the thermocouples on the sample. Two copper wires act as voltage leads and are soldered to the sample with indium. A ten-minute period (2.2 cycle) of oscillation was chosen and the temperature gradient was observed to reach steady state within half of the period, as shown in Figure 2.24. In this condition, the peak-to-peak value was used to determine the

temperature gradient across the sample, and along with the measured power supplied to the heater, and the sample dimensions, the thermal conductivity was found.

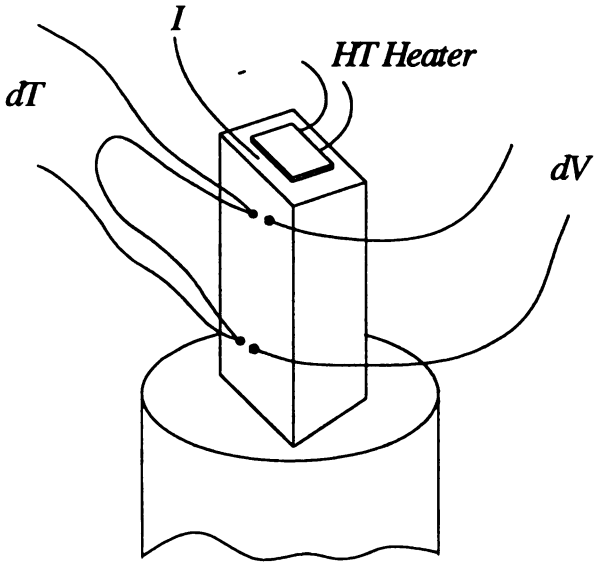

Figure 2.23 Sample configuration in 4-sample system.

This pulse technique also gives the opportunity to determine the thermopower by simultaneously measuring the voltage, *dV*, and finding the slope of the *dV* vs. *dT* curve as shown in Figure 2.25. The final measurement of electrical conductivity is measured by both ac and dc techniques.

The 4-sample system in our lab is used in the steady state mode where the temperature gradient reaches steady state during the current pulse.

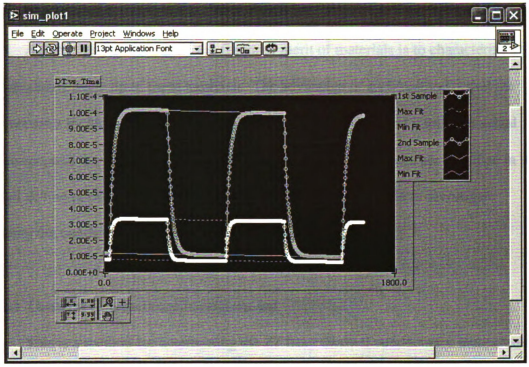

Figure 2.24 The plot of temperature gradient vs. time of two samples.

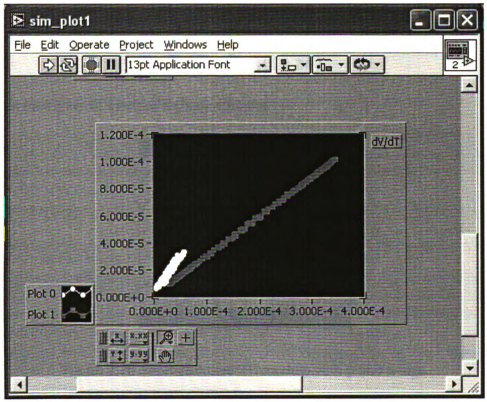

Figure 2.25 The plot of dV vs. dT curve of two samples.

2.5.2 For Modules

Another way to determine the figure of merit of materials is to characterize a module that is made up of these materials. The advantage of such method is that the measurement includes all the contact resistances of the module and it tells the actual performance of the module as a device. Since the contact resistances are included in the overall device performance, there is significant effort will be made to investigate reducing the contact resistances to these materials.

2.5.2.1 Thermal Conductance Measurement

This is a method for determining the ZT from thermal conductance measurements on a thermoelement that is connected in parallel with a metallic wire [48].

The thermal conductance K of a sample, in the absence of an electric field ($E = 0$) is $K_{E=0}$ and under zero current flow ($I = 0$) is $K_{I=0}$, it can be found that

$$K_{E=0} = K_{I=0}(1 + zT) \tag{81.}$$

where z is the figure of merit of a single element.

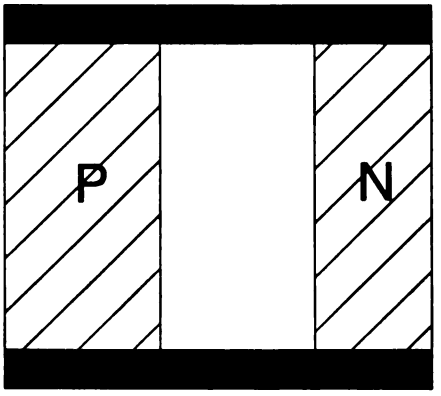

Figure 2.26 Short circuited TE module with p and n-legs.

This concept can also be applied to a module. Figure 2.26 shows short circuit in a module where the voltage is zero, i.e. the electric field is zero. Equation 14 can be also expressed as

$$Q = K\Delta T + S_{pn}T_h I - \tfrac{1}{2} I^2 R \tag{82.}$$

The short circuit heat flow is

$$Q_{short} = K_{pn}\Delta T + S_{pn}T_h I - \tfrac{1}{2} I^2 R_{Module} \tag{83.}$$

where R_{Module} is the resistance of the p and n-legs plus the contact resistance.

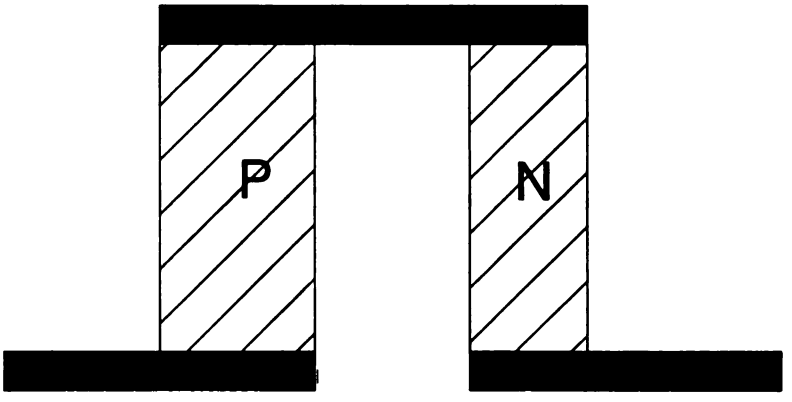

Figure 2.27 Open circuited TE module with p and n-legs.

Figure 2.27 shows an open circuit module where there is no current flow and the heat flow from the top to the bottom of the module is

$$Q_{open} = K_{pn}\Delta T \tag{84.}$$

When a temperature gradient is created across the module, there will be a flow of current. It will lead to heat transfer through Peltier effect. The current is equal to $(S_{pn})\Delta T/(R_{module})$ and the Peltier heat flow is $(S_{pn})^2 T\Delta T/(R_{module})$. Substitute I in equation 83 with $(S_{pn})\Delta T/(R_{module})$. The short circuit equation is then

$$\frac{Q_{short}}{\Delta T} = K_{pn} + \frac{S_{pn}^2}{R_{module}}\left(T_h - \frac{1}{2}\Delta T\right) = K_{pn} + \frac{S_{pn}^2}{R_{module}} T_M \qquad (85.)$$

where T_M is the mean temperature. Comparing equations 84 and 85 gives

$$K_{pn,E=0} = K_{pn,I=0}(1+ZT) \qquad (86.)$$

or

$$K^* = (K_p + K_n)(1+ZT) \qquad (87.)$$

where K_p and K_n are the separate thermal conductances of the branches, thus

$$ZT = \frac{(S_p - S_n)^2}{(R_{Module})(K_p + K_n)} \qquad (88.)$$

Equations 49 and 55 are identical if S_n, R_n and K_n are all zero.

If we assume that the conductor n is a metal with S_n=0 and the product R_nK_n will have the known value LT, where L is the experimentally determined Lorentz number. K_n from equation 55 can be eliminated and the equation becomes

$$\frac{K_p}{K^* - K_p - LT/R_n} = \frac{1}{z_pT} + \frac{K_pR_n}{S_p{}^2T} \qquad (89.)$$

Thus, z_pT can be found as the intercept on the ordinate axis of the linear plot of $\frac{K_p}{K^* - K_p - LT/R_n}$ against R_n. This plot is obtained from measurements of the thermal conductance K_p in the open-circuit condition and K^* for various values of the parallel electrical resistance R_n. The Seebeck coefficient S_p can be determined from the slope $K_p/S_p{}^2T$ of the plot.

By measuring the thermal conductance of the module with its input leads separated and then joined together, the ZT of the module can be determined. This method can be applied to whole modules as well as to individual thermocouples.

2.5.2.2 Modified Harman Technique

Continuing from the work of Harman , a modified technique is developed [49] by utilizing only the voltage components in the measurement. When an electrical current, I, is applied to a TE device, a significant device Seebeck voltage, V_α, will be added. Thus, the total voltage across a TE device is

$$V_{Total} = V_\alpha + V_\rho$$

where $V_\alpha = S*\Delta T$, $V_\rho = I*R$. Equation 49 has shown that the figure of merit of a TE material or module can be obtained from the ratio of the Seebeck voltage to the Ohmic voltage. This technique is feasible only if these two voltage components can be distinguished. V_α term can be proportionally larger for small currents and it can easily be non-zero even when there is no current flow.

The quantity of V_{Total}, I and ΔT can be measured, but it is not easy to separate the two voltages V_α and V_ρ. The Harman method resolves these two voltages by creating a bipolar AC current and sending this current through the sample. At a sufficiently high frequency (10's to 100's of Hertz), a temperature gradient can not be established across the sample, however, the Ohmic voltage can change sign with the alternating current, thus, V_ρ reverses polarity but V_α does not.

Figure 2.28 shows when a current is applied to a sample, the voltage across is shown in Figure 2.29. The voltage rises instantaneously to V_ρ and then asymptotically to V_{Total} at steady state. As the current is turn off, the voltage drops instantaneously to V_α and decay exponentially to zero.

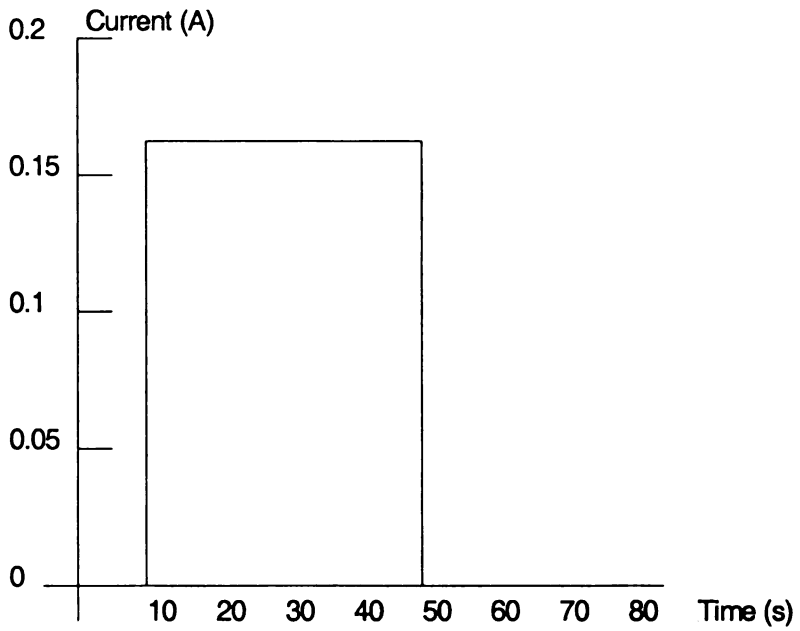

Figure 2.28 The current that is applied to the sample vs. time.

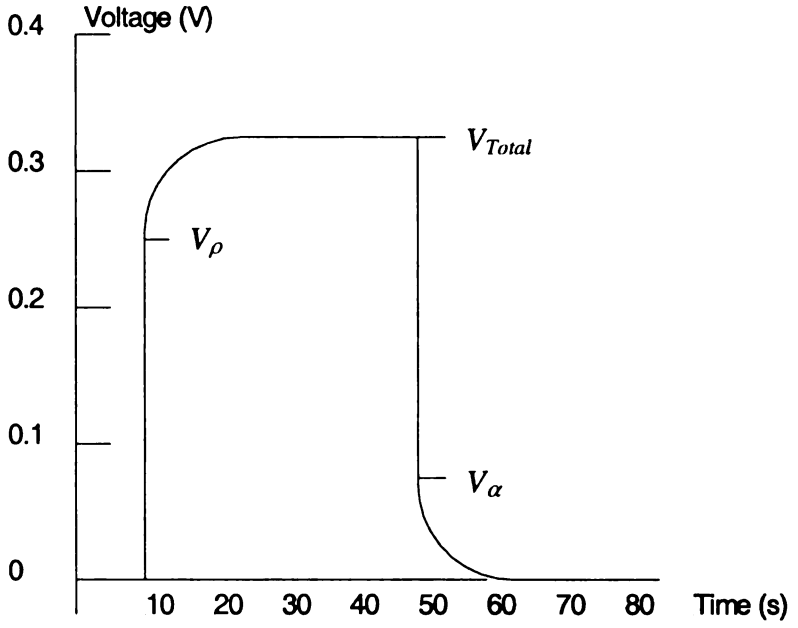

Figure 2.29 The voltage across the sample vs. time.

Chapter 3 Module/prototype Design

From the engineering point of view, the research will not seem completed until a TE module or prototype is actually built and shown to be operational. The synthesis and the transport characterization tell the properties of the individual materials used, but they do not give the necessary insight on how the device will perform after it is fully assembled.

3.1 Background of TE Generation

Figure 3.1 shows the range of output power provided by TE generators with various fuel sources. The magnitude of the power ranges from nanowatts generated in miniature thermocouple arrays to the megawatts in nuclear reactor-powered generators for the outer space applications.

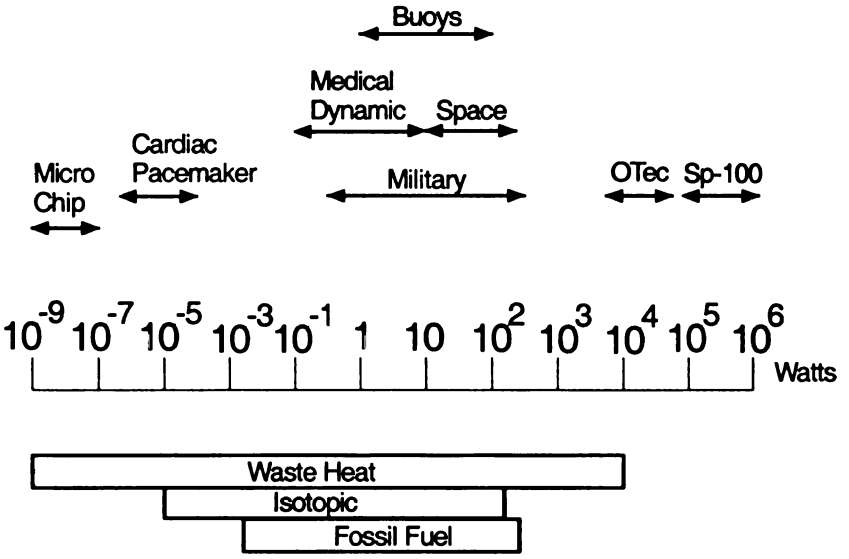

Figure 3. 1 The range of output power provided by TE generators with different fuel sources. (Sp-100 is a space subsystem)

The TE materials which perform well at high temperatures are usually developed into power generation applications where large temperature gradients are utilized for improved efficiencies. Every TE material has its optimum operating temperature. For the cubic materials studied is this project, the optimum operating temperatures are around 600-800 K. TE materials are often fabricated by either directional crystallization from a melt or pressed powder metallurgy. Each manufacturing method has its own particular advantages and sometimes, each leg in a TE module is fabricated by different methods. Table 3.1 shows the performance of various types of electrical power generators.

Types of Electrical Power Generators	Efficiency (%)	Output (W/lb)	Maintenance interval (h)
Central station steam plant	20-40	50	5000
Airplane piston engine	30	1000	50
Automobile engine	15	1000	30
Boeing 707 jet engine	20	2000	50
Fuel cell	60	7	5000
Solar cell	8	1.5	Very reliable
Thermoelectric generator (MHW)	5	0.8	70,000

Table 3. 1 Performance of various types of electrical power generators.

3.2 Choice of TE Materials for Module Fabrication

Bismuth telluride, lead telluride and silicon-germanium alloys are the most widely used materials for power generation. As shown in Figure 2.8, each material has its own range of useful operating temperatures due to its figure of merit, *ZT*. Bismuth telluride operates well between room temperatures to 250-300°C and has the best *ZT* among these materials. Lead telluride has a lower value of *ZT* and its operating temperatures are

between room temperature to 600°C. Silicon-germanium has the lowest *ZT* among the three and its operating temperature is around 1000°C. All three materials have relatively different characteristics that are important to the construction and operation of practical TE power generators. Table 3.2 shows some of the properties of these materials [50]:

TE Materials	Density (g/cm)	Thermal expansion coefficient $x10^{-6}C$	Tensile strength (lb/in^{-2})
Si-Ge alloys	3-3.5	5	3000-5000
Bi-Te and Pb-Te alloys	7.5-8.75	18	2000

Table 3. 2 Some properties of the most widely used TE Materials.

3.3 Construction of the Thermoelectric Module

The high reliability of TE modules is due to their solid-state construction and lacks of moving parts. The mean time between failure (MTBF) is typically greater than 200,000 hours. However, sometimes, a good construction design of the whole TE module system is a more important issue than the "natural robustness" of the module itself. The following are some of the important factors in constructing a good, reliable TE module [50, 51, 52]:

1) Mechanical Design

Most of the thermoelectric modules have higher compression strength than shear or tensile strength. Some of the modules can even survive compressive loads of up to 1000 psi. Therefore, the mechanical design of any thermoelectric system must ensure that only compressive loads are applied to the modules.

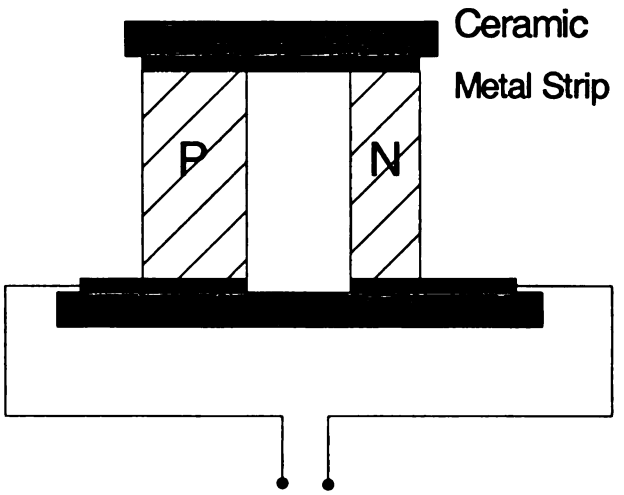

Figure 3. 2 TE module consists of a *p*- and *n*-type leg, an electrically connected metal strip and a ceramic for better thermal contact.

2) Contact

Good electrical contact must be formed between the TE materials and the metal strips since high contact resistance contributes to a significant Ohmic loss that will result in low device efficiency. On the other hand, poor thermal contact to the heat sink will result in overheating of the TE module, which will also significantly reduce the performance. All interfaces between the system components must be flat, parallel and free of debris to minimize thermal resistance. High conductivity thermal interface materials, e.g. alumina or other ceramics, are often used to ensure good contact between surfaces.

a) Solder

The most common way to form contact with low temperature TE materials, e.g., bismuth tellurides are soldering. The types of solders define their specific operating temperatures and must be selected carefully so as to avoid elements that might poison the TE materials, for instance, copper ions are known to rapidly diffuse into TE materials and change their properties. In some cases a diffusion barrier between the TE materials and the solder or

contacts is used. Introducing a flux prior to soldering might be a solution for some TE materials that do not bond well with solder directly.

b) Metallurgical bonding

Metallurgical bonding is often used as contact electrodes, however, metallic bonding is restricted to certain operating conditions where diffusion of the materials is negligible. The thermal expansion, chemical and physical properties of the materials used for contacts are also important considerations in building a module. Some of the examples are: tungsten and silicon alloys form very good bonding with silicon-germanium alloys, using graphite as a barrier layer between the tungsten and silicon-germanium alloys can extend the operating temperatures; Iron bonds well with lead telluride and nickel is used as a barrier to prevent the diffusion of iron into lead tellurides.

c) Pressure contact

Electrical and thermal losses across the mechanical interfaces are usually minimized by using spring-loaded pressed contacts. In fact, many of the high temperature TE modules are configured with pressure-contacts alone and no solder used. The TE materials are held together by spring-load pressed contacts. This helps to avoid difficulties associated with differences in the coefficients of thermal expansion between contacts and the TE materials.

d) Conductive paint

The alternative way for connecting TE materials is the use of conductive paint or paste. For instance, silver paint or platinum paint have offered very good electrical contacts.

Sometimes, a combination of conductive paint and pressure contact are obtained for better module construction.

3) Moisture/Oxidation

Moisture and oxygen in the air can corrode some TE materials. In this case it is important to seal the TE materials (of the modules) with an epoxy or coating material that can prevent oxidation without significantly degrading the module efficiency. Often power generators such as those that use bismuth telluride and lead telluride are evacuated, sealed, and back-filled with an inert gas in order to minimize material degradation at high temperatures. At low temperature, effective moisture seals are often installed. For instance, flexible foam insulating tapes or sheet materials or silicone rubber RTV are relatively good moisture seals. At high temperatures, silicon-germanium alloys are quite insensitive to their operating environment. Oxides will form on the surface of the materials but it will not affect the properties of the materials so sealing is not required for this type of materials. Sometimes, a silicon nitride coating is employed to prevent sublimation for extended operating temperatures over 1000 °C.

3.4 Segmented TE Modules

A segmented TE module consists of multiple layers of different TE materials. In a stacked configuration, individual modules made with different materials are stacked. Another configuration is also possible, called a unicouple, where different TE materials are stacked in direct contact with each other (or separated by a thin barrier layer). Segmentation can provide a wider operating temperature range for the module. One of

the examples of a segmented TE unicouples is shown in Figure 3.3 below [53]. The unicouple includes a combination of state-of-art TE materials including Bi_2Te_3 and novel materials based on skutterudites made in the Jet Propulsion Lab (JPL) is shown in Figure 3.3. Each section of one leg has the same current and heat flow, and the geometry of the legs must be optimized to maintain the desired temperature profile. This optimization is mainly due to differences in thermal conductivity. The segmented unicouple is expected to operate between 300 and about 975 K with a projected thermal to electrical efficiency of up to 15%.

The segmentation can be adjusted to accommodate various hot side temperatures depending on the specific application requirement. Various techniques and materials have been investigated to develop better bonding between the TE segments and to the metallic contacts. Calculations based on typical material properties show that a low contact resistance of less than about 20 $\mu\Omega cm^2$, is required to keep the efficiency from being significantly degraded by the contact resistance.

Both the *n*- and *p*-segmented legs are fabricated by hot-pressing the various TE materials separated by thin metallic foils. Nickel and niobium metallic powders were added on the top of the legs during the hot-pressing. The electrical contact resistance was measured by a four probe technique up to the predicted optimum temperatures. One voltage probe is located at one end of the sample while the second probe can move along the sample. The variations of the electrical contact resistance was recorded as a function of the distance of the moving probe to the fixed probe.

Electrical contact resistance lower than 5 $\mu\Omega cm^2$ have been obtained for each of the junctions at its projected operating temperature. For the *p*- and *n*-type samples with

Ni as the top metallic segment, even though, the interfaces showed good bonding, lateral cracks are observed within the Skutterudite materials in the region adjacent to Ni. This is probably due to the relative large difference between the thermal expansion of Ni, 13.3×10^{-6}/K, and to those for *p*-$CeFe_4Sb_{12}$ and *n*-$CoSb_3$, 7.5 and 6.36×10^{-6}/K, respectively. On the other hand, the samples with Nb as the metallic contact, did not show cracks since the coefficient of thermal expansion of Nb is 7.1×10^{-6}/K and is a much better match to the samples.

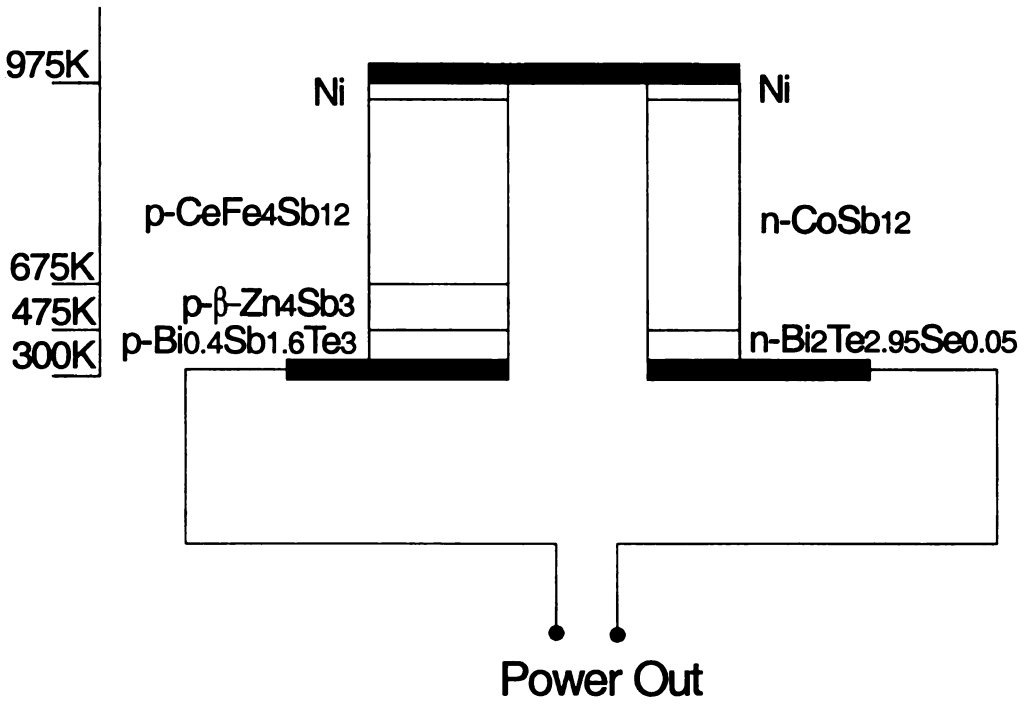

Figure 3. 3 The combinations of various TE materials at the unicouples.

Chapter 4 High temperature measurement system

4.1 System set-up and design

A new thermoelectric measurement system is presented to characterize the properties of new materials, primarily at high temperatures (up to 800K) where materials for power generation applications are typically operated. This computer-controlled system was designed to measure the thermoelectric power through a slope measurement technique, also called the pulse technique, and electrical conductivity in the standard four-probe configuration. Here we present the design and computer-controlled features of this measurement system, and its use in studying the properties of new materials over a very broad temperature range (80-800K).

The system consists of a Cryo Industries cryostat chamber, a Varian Turbo-V 70 Controller unit, a temperature controller (Lake Shore 330), a source meter (Keithley 2400), four nanovoltmeters (Keithley 2182) and a computer. The LakeShore 330 temperature controller is tuned by adjusting the Gain (Proportional), Reset (Integral) and Rate (Derivative) of the controller, and settings can vary from sample to sample.

The Varian Turbo-V 70 Controller is a microprocessor-controlled, solid-state frequency converter with self-diagnostic and self-protection features. The controller is composed of a power transformer, front panel display and keypad, rear panel with input/output connectors and a PCB that includes the power supply, 3-phase output, A/D section and other controls. This unit monitors the operation of a rough pump and a minuteman turbomolecular-dry pump (Turbo-V 70LP pump). The controller drives the pumps during starting phase by controlling the voltage and current with respect to the speed of the pump. The turbo-pump is rated to 1.5×10^{-9} Torr and the rotational speed is

75,000 rpm. Due to the flanges that are used, the system can only be pumped to $5x10^{-5}$ Torr at around 700K. However, this is a sufficient vacuum level for the experimental purposes.

The cryostat chamber is a Cryo Industries continuous flow cryogenic system. A flexible stainless steel transfer line is connected to the cryostat with the other end into a liquid nitrogen storage dewar. The sample stage on the end of the cold finger is custom designed. The cryostat contains three 20-pin connectors and they are labeled as A, B and TC. In this system, only connectors B and TC are used. The wiring diagrams of the two connectors are shown in Figures 4.1 and 4.2. Connector B has bundled all the wires from the source and voltmeters while Connector TC has connected a cable from the temperature controller to the heater and sensor of the cryostat.

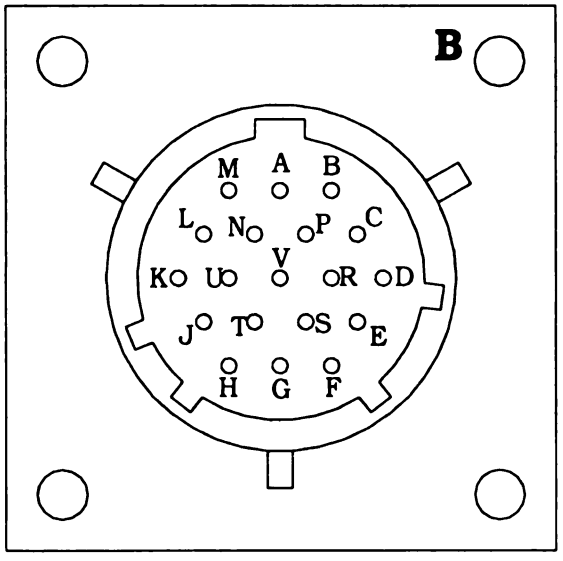

M **V+**
B **V-**
C **TC+ (constantan)**
D **TC+ (chromel) also short to V+**
L **TC- (constantan)**
K **TC- (chromel) also short to V-**
V **I+**
T **I-**
H **Heater+**
F **Heater-**

Figure 4. 1 Wiring diagram of connector B as seen from the outside of the connector. TC_+ is the upper side of the two thermocouple that are mounted on the sample, TC- is the bottom thermocouple.

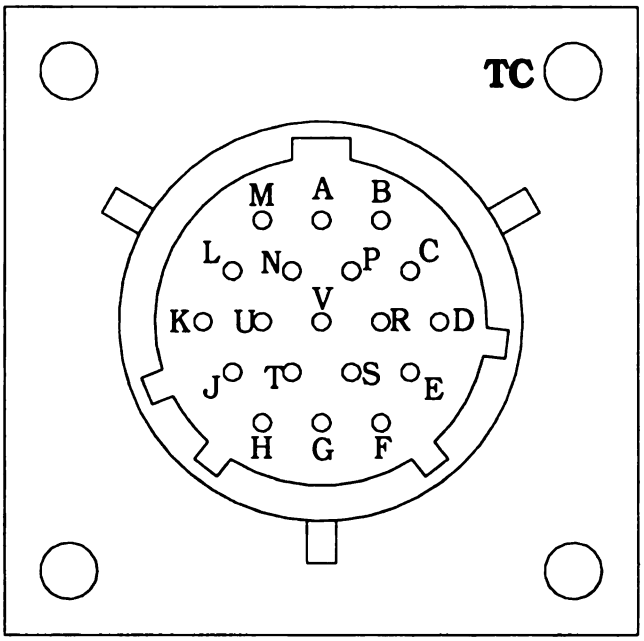

M heater white (LO)
L heater yellow (HI)
K heater black (LO)
J heater red (HI)
E sensor I+
F sensor V+
G sensor V-
H sensor I-

Figure 4. 2 Wiring diagram of connector TC as seen from the outside of the connector. This connector contains the heater and sensor leads to the temperature controller.

The Lake Shore 330 Temperature Controller is a microprocessor-based instrument with digital control of a variable current output. The sensor for this controller is a 100Ω Platinum resistor. The controller has dual sensor inputs and contains isolated current sources which allow true 4-wire sensor readings. It can store up to 21 sensor calibration curves. It has autotuning (PID) control as well as zone modes which can store up to 10 temperature ranges. Figure 4.3 and 4.4 show the sensor and heater connectors on the rear of the instrument. The wiring labels in Figure 4.3 and 4.4 correspond to the wiring labels in Figure 4.2. There are two pairs of heaters: label L/M and label J/K at the connector TC. The temperature controller is usually connected by either pair of the heater and each pair has a 50Ω resistor, if they are connected in parallel, the heater output is 25Ω.

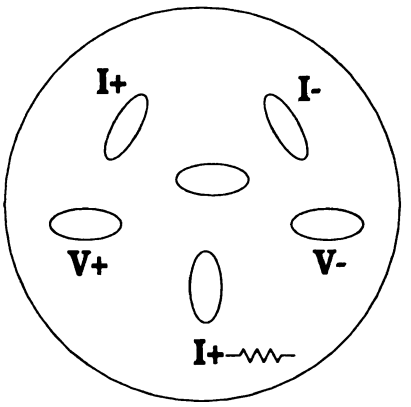

Figure 4. 3 The wiring diagram of the Lake Shore 330 temperature controller sensor Channel B connector in the rear panel.

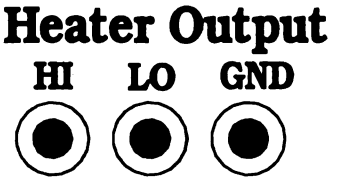

Figure 4. 4 Heater Output of the rear panel of Lake Shore 330 temperature controller.

The Keithley 2400 Source Meter is a dc power supply with a built-in multimeter. It has 0.012% accuracy with 5½-digit resolution. The source voltage is from 5μV to 210V and it can measure 1μV to 211V; the source current is from 50pA to 1.05A and it can measure 10pA to 1.055A. It can measure resistance from 100μΩ to 211MΩ and the maximum source power is 22W. This meter can deliver 520 readings per second over the GPIB cable connecting it to the computer.

The Keithley 2182 Nanovoltmeter is a 7½-digit high-performance digital nanovoltmeter. It is a low noise and high speed device with 15 nV peak-to-peak noise at 1 second response time and 40-50 nV peak-to-peak noise at 60 ms response time. The

meter can measure voltages from 10 nV to 12 V. The meter also has two trigger link cables for sending and receiving trigger pulses to initiate data collection.

All of the instruments that were introduced are controlled by LabVIEW programming. The communication between the measurement instruments and the computer is through GPIB address cables. Figure 4.5 shows the set-up of the high temperature system.

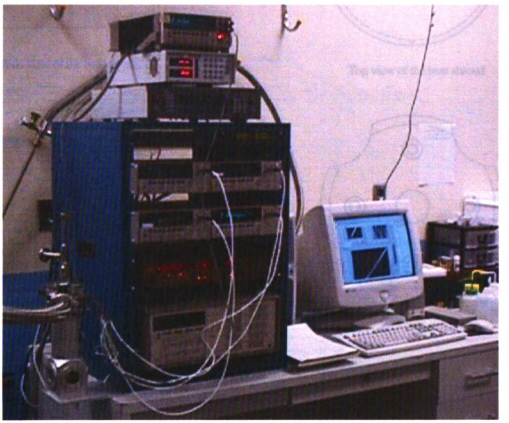

Figure 4. 5 The set-up of the high temperature system

Figure 4.6 shows the different views of the sample stage. The stage and the heat shroud are made with OFHC (Oxygen Free High Conductivity) copper and nickel/gold plated on the surface. The stage screws onto the cold finger of the cryostat while the heat

shroud screws onto the stage. The sample is mounted on the stage with conductive paint, and the heat shroud is used to reduce the radiation heat loss.

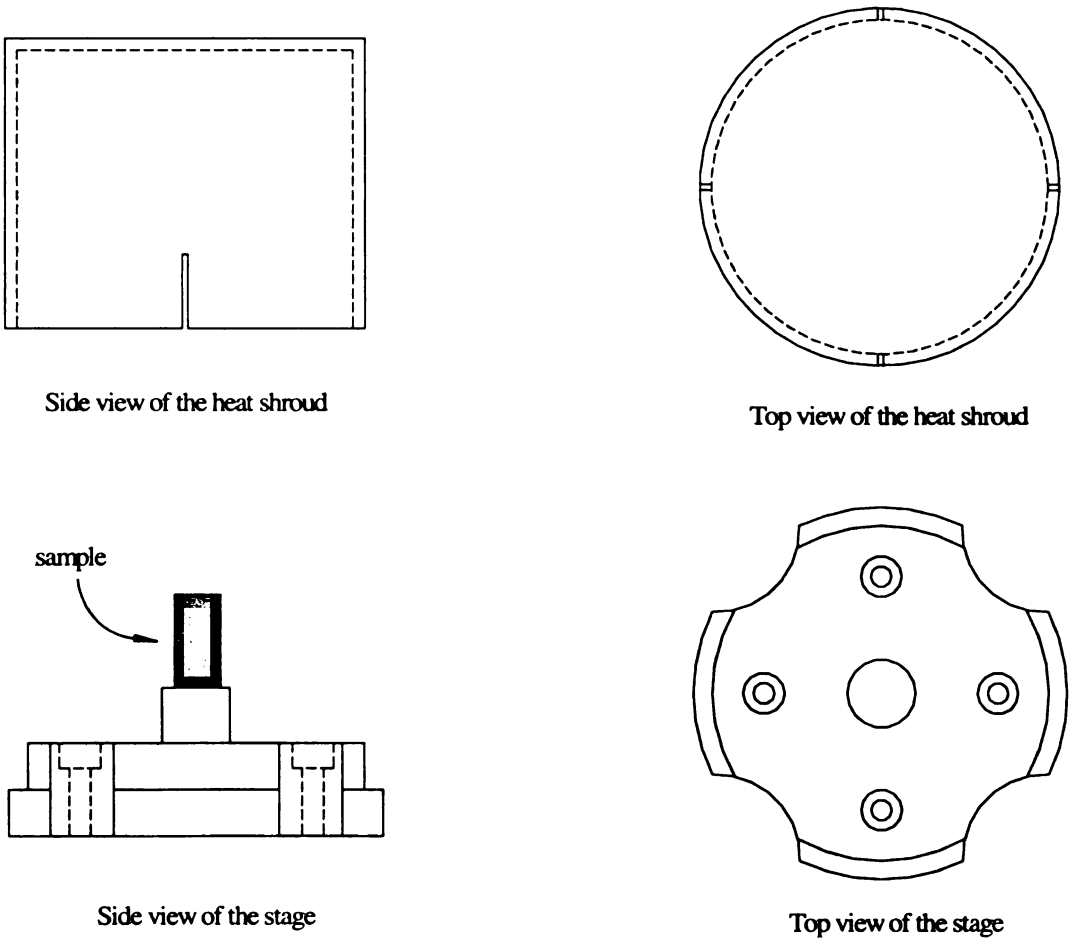

Figure 4. 6 The design of the sample stage.

4.2 Mounting and Running

Figure 4.7 shows the sample configuration on the stage. The pulse technique is used to periodically heat one end of the sample through a high temperature heater (100 W) to establish a temperature gradient of less than 1K. The high temperature heater is a 500 Ω Platinum RTD from Omega and it is ceramic encased. The temperature rating

is from –50 to 600 °C. The temperature and voltage gradients of the sample are measured by two single ended thermocouples (TC). In the early stage of the development of this system, the thermocouple was made of 0.001" diameter bare copper and constantan wires, as shown in Figure 4.8.

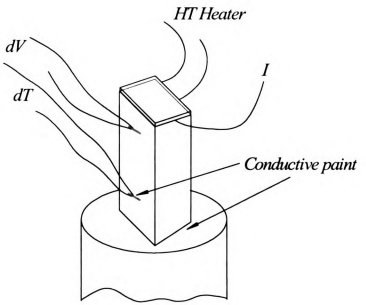

Figure 4. 7 The sample mounting configuration.

Figure 4. 8 The photo of the sample mounting configuration in the early development of the system.

The reference temperature of the thermocouples was located at the connectors, where the temperature is near room temperature. This location of the reference temperature has caused some inconvenience in replacing the new thermocouples. Therefore, a more recent wiring configuration is used, where the reference temperature locates at the sample stage, Figure 4.9 and 4.10. The heater and current leads are all 0.001" diameter bared copper wires. Bared wires are fed through fiberglass sleeves for electrical insulation.

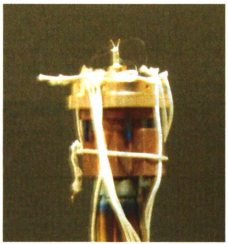

Figure 4. 9 The photo of the sample mounting configuration now.

Figure 4. 10 A close view of the sample mounting configuration now.

4.3 Measurement Method

The voltage (dV) and temperature (dT) gradients are measured simultaneously. The slope of dV *vs.* dT curve gives the thermopower as shown in Figure 4.11. Figure 4.12 shows the steady-state plot of the temperature gradient, dT as the sample is periodically heated. The electrical conductivity, σ, of the sample is measured by a four probe configuration, $\sigma = L/(R \cdot A)$ where L is the probe spacing, R is the resistance and A is the cross-section area of the sample.

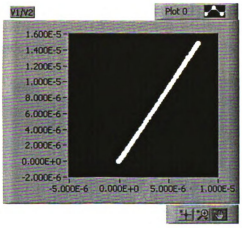

Figure 4. 11 The slope of dV *vs.* dT curve

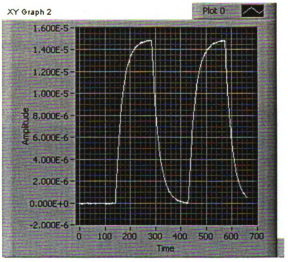

Figure 4. 12 The temperature gradient vs. time plot.

The heater and all the leads are mounted to the sample with conductive paint. Several different paints are used including Pelco® 16031 silver paint, high temperature silver paint, SPI# 05006-AB carbon paint and SPI# 04990-AB platinum paint. Silver paint works very well although it was not found suitable to some samples at high

temperatures. The high temperature silver paint was found to evaporate at high temperature and coat the sample surfaces. Carbon paint is the most inert paint but the contact resistance is too high and it is not suitable for electrical conductivity measurements. Platinum paint forms the best contact to the sample, but it has to go through a certain process of curing and the cost is very high. Furthermore, as the temperature is increased, the platinum paint can easily lift off the sample surfaces, causing lost contact of leads.

In addition to the challenges in choosing the right contact pastes, temperature stabilization at high temperatures is the most challenging task for this system. Figure 4.13 shows that when the temperature is not stable, the dV vs. dT curve and the temperature gradient plot will be distorted and thus the thermopower measurement will not be accurate.

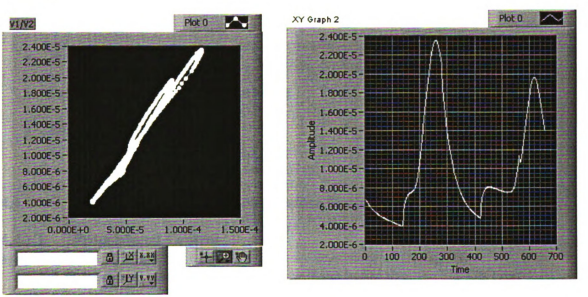

Figure 4. 13 The dV vs. dT curve and the temperature gradient plot when the temperature is not stable.

4.4 Software Control – PID

The PID control algorithm [54] is the most widely used automatic control technique in industries and it is the basis for many advanced control algorithms and strategies. PID control is a simple form of feedback. Feedback is a very powerful concept with many useful properties, e.g. reducing the effects of disturbances, creating robust linear relations, following commands with high fidelity, and establishing robustness to process variations. But there is some risk of instability, and for the control loop to work properly, the PID loop must be properly tuned.

The PID control algorithm comprises three elements: Proportional (P) - also known as Gain, Integral (I) - also known as Automatic Reset or simply Reset, and Derivative (D) - also known as Rate

The algorithm is normally available in several combinations of these elements:

- Proportional only
- Proportional and Integral
- Proportional, Integral, and Derivative
- Proportional and Derivative

4.4.1 Introduction to PID in Temperature Control

4.4.1.1 Proportional Control

A proportional controller attempts to perform better than the On-Off type controller by applying power, *W*, to the heater in proportion to the difference in temperature between the system and the set-point,

$$W = P \times (T_S - T_O)$$

where P is the *proportional gain* of the controller, T_S is the set-point (or set temperature) and T_0 is the system temperature (actual temperature). As the gain is increased the system responds faster to changes in set-point but becomes progressively underdamped and eventually unstable.

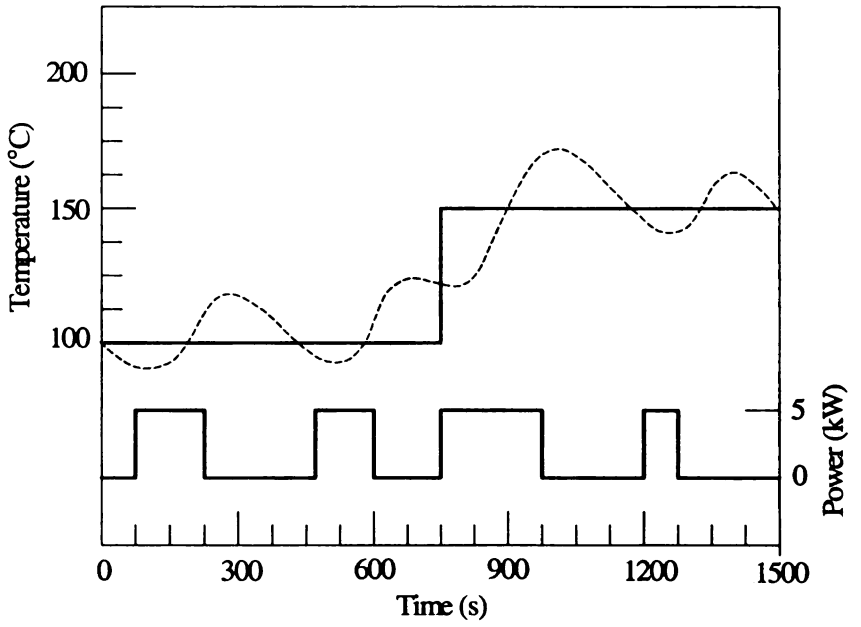

Figure 4. 14 Signals from an On-Off temperature controller.

The top portion of Figure 4.14 shows the set temperature (solid line) and the actual temperature (dashed line), the bottom line shows the control signal of a typical on-off controller. Figure 4.15 shows the set temperature (solid line) and the actual temperature (dashed line) signals of a controller with proportional control only.

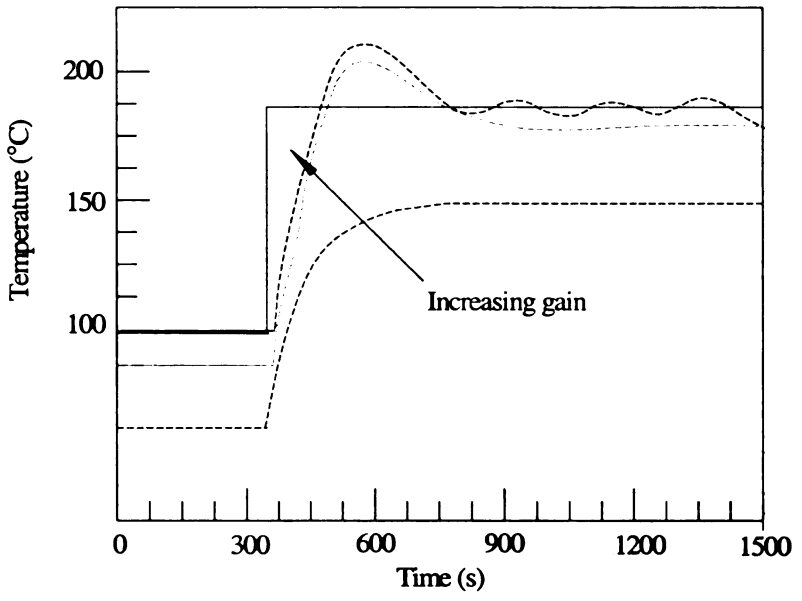

Figure 4. 15 Proportional temperature controller.

4.4.1.2 Proportional + Derivative Control

The stability and overshoot problems that arise when a proportional controller is used at high gain can be eliminated by adding a term proportional to the time-derivative of the error signal,

$$W = P \times \left((T_S - T_O) + D \times \frac{d}{dt}(T_S - T_O) \right)$$

This technique is known as *PD control*. The value of the *damping constant, D,* can be adjusted to achieve a critically damped response to changes in the set-point temperature. Too little damping will result in overshoot and ringing, too much will cause an unnecessarily slow response. Figure 4.16 shows the signals from a PD temperature controller.

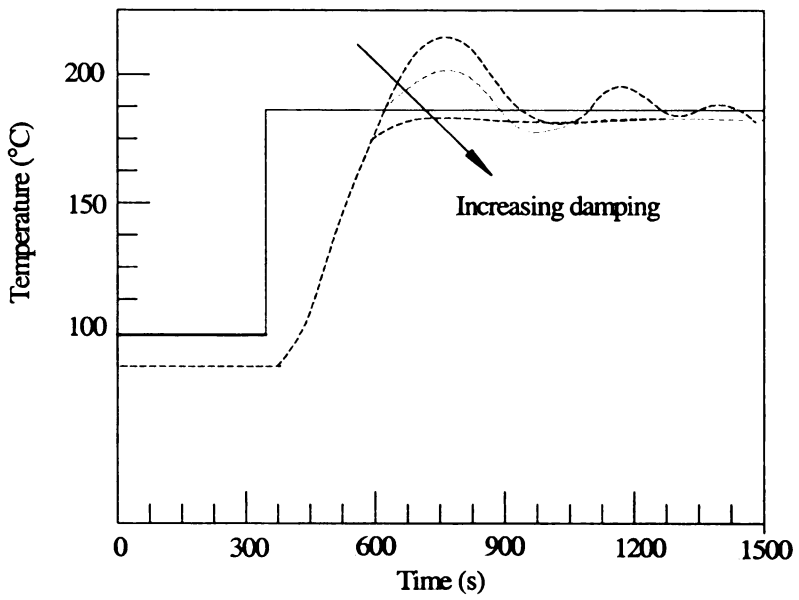

Figure 4. 16 Proportional + Derivative temperature controller.

4.4.1.3 Proportional + Integral + Derivative Control

Even though PD control deals with the overshoot and ringing problems associated with proportional control, it can not eliminate the steady-state error. Fortunately it is possible to solve this problem by using relatively low gain and adding an integral term to the control function,

$$W = P \times \left((T_S - T_O) + D \times \frac{d}{dt}(T_S - T_O) + I \times \int (T_S - T_O) dt \right)$$

where I, the *integral gain* parameter is sometimes known as the controller *reset level.*

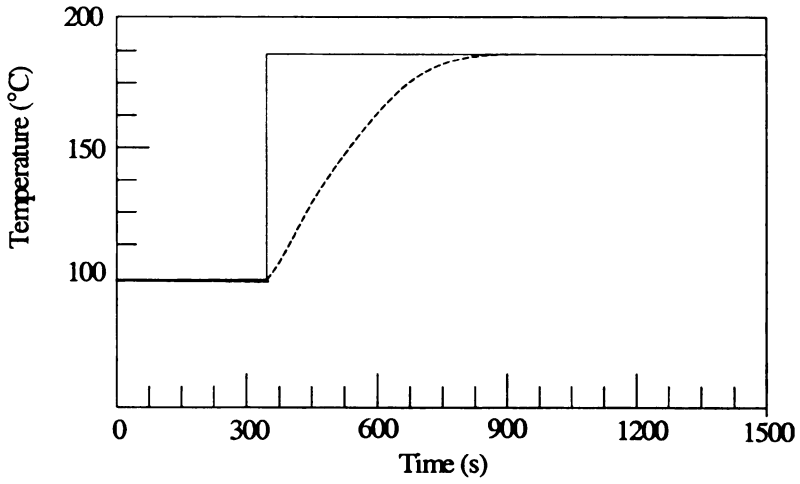

Figure 4. 17 Proportional + Integral + Derivative temperature controller.

This form of function is known as proportional-integral-differential, or PID, control. The effect of the integral term is to change the heater power until the time-averaged value of the temperature error is zero. The method works quite well but complicates the mathematical analysis slightly because the system is now third-order. Figure 4.17 shows the signals from a PID temperature controller.

4.4.1.4 Conslusion in PID Control

The PID control algorithm does not "know" the correct output to bring the process to the setpoint. It merely continues to move the output in the direction which should move the process toward the setpoint. The algorithm must have feedback (process measurement) to perform.

The PID algorithm must be "tuned" for the particular process loop. Without such tuning, it will not be able to function. The tuning is based on the dynamics of the process response.

4.4.2 Tunning the LakeShore 330 Temperature Controller

There are various PID tuning methods and every system has its most suitable tuning method. We have adapted the tuning procedures from the LakeShore Model 330 Autotuning Temperature Controller User's Manual [55] for our high temperature system. The procedures are stated in the following paragraphs. Further reading in the Controller User's Manual is recommended.

Step 1: Give a set temperature, e.g. let the set temperature be 310K. Turn off both Reset (I) and Rate (D). Enter a nominal gain of 50 by adjusting value of P and verify that the heater turns on. If the heater does not turn on, then increase the gain setting until it turns on; and wait to let the system stabilize. One should expect the controller to stabilize at some point below the set point (typically a few Kelvin below). As seen in Figure 4.18, the system stabilized at 305 K.

Step 2: Increase the gain by a factor of two until the system temperature begins to oscillate. Adjust the gain for small sustained oscillations. For example, if the oscillation amplitude decreases with time, increase the gain. However, if the oscillation amplitude increases with time, decrease the gain.

In this case, when the gain was increased from 50 to 100 (50x2), the temperature oscillated with a decreasing amplitude. Thus, the gain was further increased to 150. The temperature then started to oscillate with increasing amplitude. These two settings helped to determine where the possible value of gain would be. At a gain setting of 120, the system oscillated with a constant amplitude.

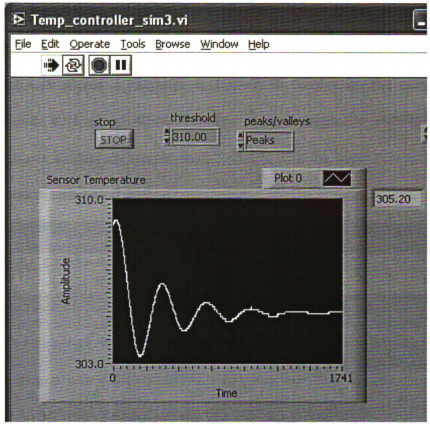

Figure 4. 18 A snapshot of LabVIEW display on the system temperature with P, I, D = 50, 0, 0

Then the period of these oscillations is measured to determine the correct setting for reset (I). In this case the period of oscillation is 235 seconds so I and D can be determined as:

I = max. reset value/Period = 999/235 = 4 since the maximum value of I in the 330 controller is 999.

D = Period/4 = 235/4 = 59. Depending on the system, a setting of D = Period/8 might have a better effect. Also, depending on the system, the gain should be reduced by a factor of two to three when this is used. After some iterations, let P(new) = P(old)/3 = 120/3 = 40

Step 3: Re-enter the new values for P,I,D = 40, 4, 59 until the temperature again stabilizes.

Figure 4.19 shows a snapshot of LabVIEW display on the sensor (system) temperature with P, I, D of 40, 4, 59. The system eventually stabilize at 310 K. Figure 4.20 shows another set temperature, T=330K with the same PID and it took less than 15 minutes to stabilize at desired temperature.

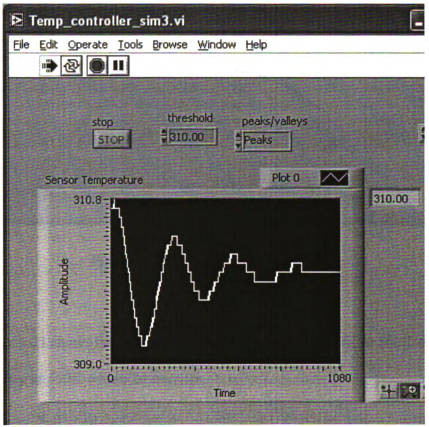

Figure 4. 19 A snapshot of LabVIEW display on the sensor (system) temperature with P, I, D = 40, 4, 59. The system stabilize at 310 K.

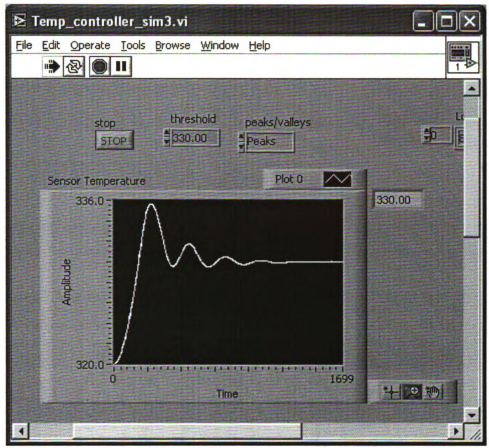

Figure 4. 20 System stabilize at 330K.

Figure 4.21 shows the temperature transition between 550K to 560K and the system stabilize at 560K within 20 minutes.

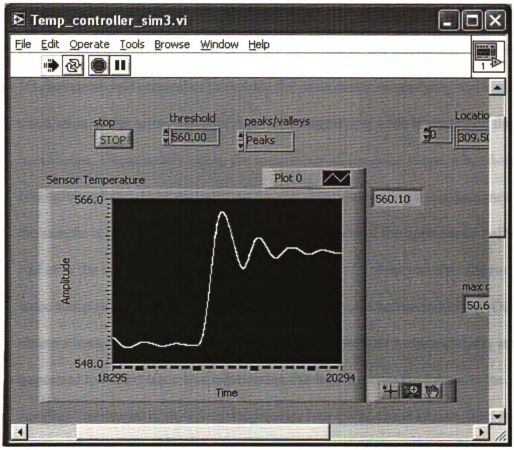

Figure 4. 21 The transition between temperatures.

4.5 Sample Mounting Procedures

This section mainly addresses sample mounting procedures. This is not the only way to mount a sample but it can act as a guide. Alternative methods can be used as long as they result in the same outcome.

1. When new samples arrive in the lab, record the material composition, the ID numbers, the person who made them and the date of receipt in the lab logbook.
2. Prepare a "Sample Run Sheet" for each sample, record the geometry, the appearance and any preliminary tests that were taken on the sample. The

geometry of the sample can be measured by the digital calipers or by a microscope and micrometer. If using the microscope, the micrometer scale is not 1:1, so one should remember to include the micrometer magnifying scale in calculation of the actual measurement. The magnifying scale is posted on the microscope. Occasionally, when the sample has an irregular shape, a hand-sketch is helpful and should be included on the run sheet. Recording the appearance of the sample is important because it allows comparison of the appearance before and after the run. For instance, discoloration might be observed after the run for some samples and it will be helpful to have taken notes before mounting. Other observations, for example, cracks on samples, needle-like surface and etc, are also important to record since this information can be critical in the future. If the sample is measured in the room temperature four-point probe system, also record the electrical conductivity value at room temperature. If the sample has a rectangular shape, it is necessary to measure all four faces to verify the homogeneity of the sample.

3. It is necessary to clean the sample prior mounting. Acetone is used to clean the surface. Next, the surface of the sample needs to be scraped in order to remove any possible oxide layer. Depending on the sample, polishing on a sand paper might be helpful too. Again, clean the surface of sample with acetone.

4. After cleaning the sample, it is ready to be mounted on the sample stage. Make sure the stage is clean and contains no leftover silver paint from the previous run. The dry silver paint can be removed by scraping with a razor blade, followed by acetone cleaning.

5. The sample is mounted on the sample stage with silver paint. Remember to shake the silver paint very well before using it. Shake the bottle laterally so that the paint does not splash against the cap, or alternatively stir the silver paint with a clean wooden stir stick. Open the cap and use the wire holder tool to take some silver paint (only a small drop is needed) from the brush and paint it on the stage. Mount the sample by sliding on the paint so that there are no air bubbles between the sample and the stage.
6. Allow 1-2 hours for the silver paint to dry. Sometimes, the drying time can take longer due to the humidity in the room. Then proceed on mounting the positive current lead and the HT heater on top of the sample with silver paint. It is often helpful to bend wires into place before applying silver paste so to avoid having to hold the wire in place while drying. Connect the HT heater with Cu wire leads after the paint is dry. Figure 4.22 shows the HT heater and positive current lead are mounted on top of the sample.
7. Place the HT stage underneath the microscope for mounting the thermocouple leads. Two single-ended chromel-constantan thermocouples are mounted on the side of the sample with silver paint. After mounting, remember to measure the separation between leads under the microscope.

Figure 4. 22 The HT heater and the positive current lead are mounted on top of the sample with silver paint.

8. Again, before mounting the thermocouple with silver paste, bend the wires into place before. Kapton tape can be used to hold the wire in place when putting the silver paint on. Remember to remove the Kapton tape only after the silver paint is completely dry, or else, wires can be pulled away as removing the tape. Figure 4.23 shows the top thermocouple is held with Kapton tape while the bottom thermocouple is mounted on the sample with silver paint. Remember to make as small contact point of silver paint as possible on the thermocouple and add more when necessary. Large contact point can result in difficulty in measuring the accurate lead separation and small deviation in lead separation will cause a large change in electrical conductivity measurement.

9. The leads separation is measured between the mid-points and the edges of the silver contacts as shown in Figure 4.24. But only the mid-point to mid-point leads separation is used in the electrical conductivity measurement.
10. When finished mounting, arrange all the bare wires so that they do not touch each other nor the radiation shield that is about to be placed on. Check the wiring connection by using the multi-meter before and after placing the shield on.

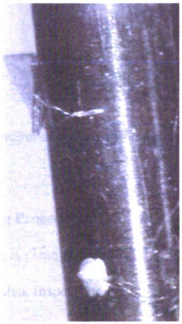

Figure 4. 23 The top thermocouple is held with Kapton tape and the bottom thermocouple **is** mounted on the sample with silver paint.

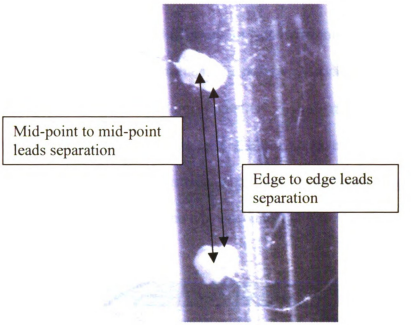

Figure 4. 24 The leads separation is measured between the mid-points of contacts and edges of the contacts.

4.6 High Temperature Operating Procedures

1. Ensure that the chamber o-ring is clean and lightly lubricated with high vacuum grease to seal appropriately. Also, inspect the o-ring groves on the sealing faces for cleanliness. Place the cryostat into the chamber and plug-in all connectors, verify the temperature controller reads the correct temperature (nominal room temp approx 24°C or 297K).
2. Turn on the dry pump vacuum system by pressing the "start" button. The rough pump will start first and then the turbo pump will automatically turn on when certain vacuum level is reached (usually around 10^{-3} Torr). Notice that the pump speed increase till 75 krpm. If it does not reach 75 krpm, stop the pump to detect possible leaks. It takes 1.5-2 hours for the system to reach vacuum level of 10^{-5} Torr at room temperature once the pump speed reaches 75 krpm.

3. A so-called "manual run" can be operated. The manual run does not include the automated temperature control software. In Nanowire computer, under C:\Program Files\National Instruments\LabVIEW 6\user.lib, in "Tim's Programs old" library, choose "PowerFactor_Manual.vi", the program will pop up as seen in Figure 4.25. This program will control the thermopower and electrical conductivity measurements. This is a quick check on the room temperature measurement as well as verify the wiring connections are fine.

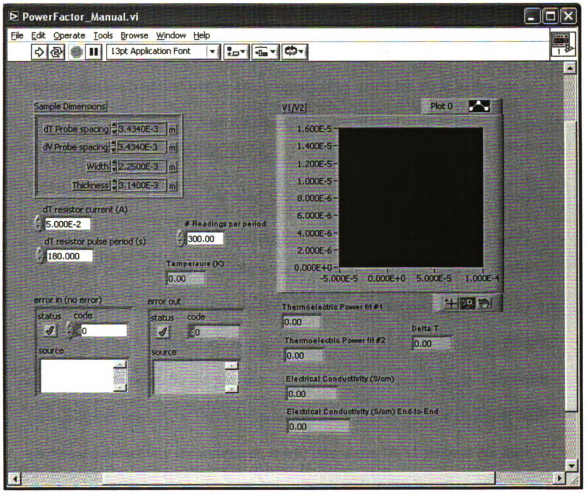

Figure 4. 25 PowerFactor_Manual.vi

4. In "PowerFactor_Manual.vi", enter the geometry of the sample, dT and dV probe spacing are the probe spacing of the thermocouples and voltage leads. In our case, these two values are the same because the two single-ended thermocouples are also used as voltage leads. The number of reading per period is default to 300 but it can be changed depending on your needs. The *dT* resistor current is the amount of current supply to the heater resistor for heat pulsing. For metals, a higher current is required, for instance 30-50 mA, for typical sample dimensions to create a temperature gradient of less than 1K. For semiconductors of typical sample dimensions, a heater current of 5-10 mA is sufficient. The *dT* resistor pulse period is default to 180 seconds and can be adjusted depends on the steady-state condition. The first step of this program is by using the pulse technique, construct a heat pulse and measure the voltage and temperature gradient across the sample simultaneously. To develop the temperature gradient across the sample, a platinum resistor was used. The second step is to measure the electrical conductivity by flowing an appropriate current (generally 10mA) through the sample and measuring the resulting voltage gradient. There are two fits for the thermopower values and will be discussed later in this section.
5. The "PowerFactor_Manual.vi" is designed to construct a 2.2 temperature gradient period per data point. So the program run time per data point is about 2.2 x pulse period. In this case, 2.2 x 180 = 6.6 minutes. Also, including the delay time and electrical conductivity measurement, it will take about 10-12 minutes per data point.

6. When running this program, it is also recommended to open another program "Thermopower slope fit.vi". This program will display the temperature gradient of the sample and allows checking if steady-state condition is met.
7. When the run is finished, the display is on Figure 4.26. The "Thermopower slope fit.vi" is on Figure 4.27. If the values look fine, then continue with the temperature dependent measurements.

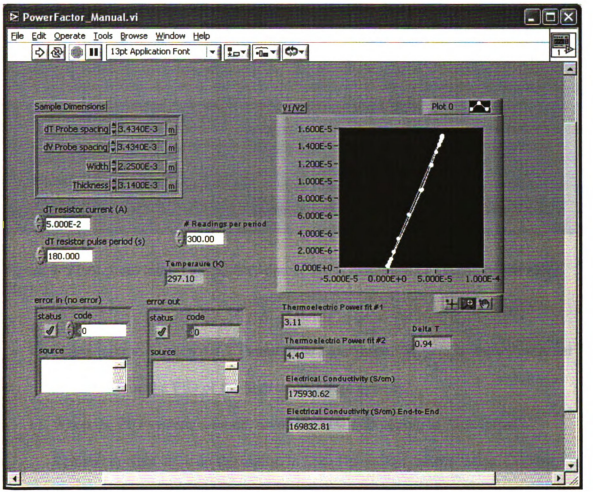

Figure 4. 26 After the measurement, the values are displayed in PowerFactor_Manual.vi

8. Since different samples have different heat capacity and emissivity, the temperature controlling parameters, PID, needed to be tuned for each sample.

9. Choose the "Temp_controller_sim3.vi" to display the temperature of the system verses time. The "330 TUNE PID_sim.vi" allows changing the PID setting manually.

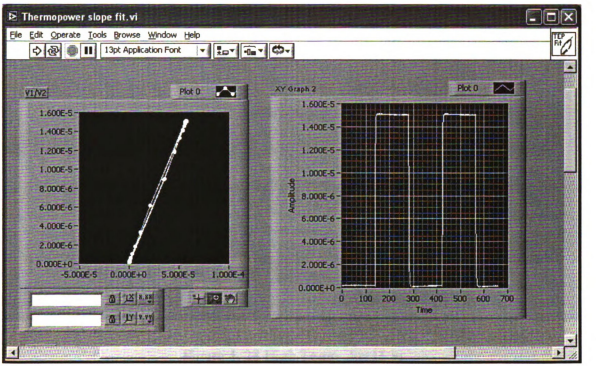

Figure 4. 27 At room temperature, the value of Mo is displayed in Thermopower slope fit.vi

10. Please refer to Section 4.4.2 Tunning the LakeShore 330 Temperature Controller in how to tune the PID of the high temperature system.
11. When the PID system is tuned, saved the new PID setting to "330 Init.vi". Remember right click on the mouse in Data Operations, select "Make Current Values Default" and saved the changes.
12. "High Temp_Apr16.vi" is the automatic run with temperature ranges and the display can be seen in Figure 4.28. This program measures and saves data to a file as a function of temperatures.

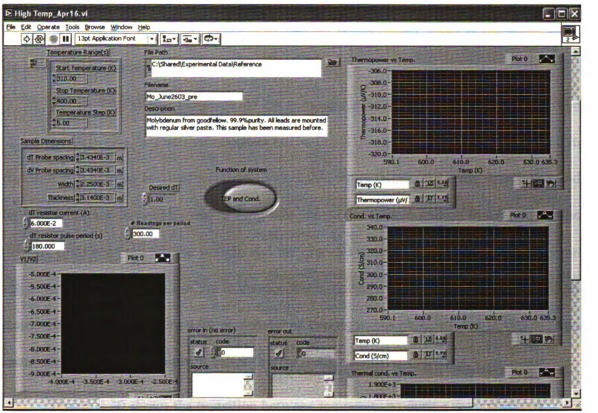

Figure 4. 28 High Temp_Apr16.vi

13. "Temp_controller_sim3.vi" can be run simultaneously with the "High Temp_Apr16.vi".

14. Most of the time, once the PID is properly tuned for the system at around 310K or higher, the PID is usually good till 700K. Sometimes, temperature instabilities might occur during the run. Then, the system needs to be re-tuned by following the tuning procedures previously described. An example is shown in the last part of this section.

In measuring the thermopower, the dT vs. dV curve must be fit and the slope extracted from the data. In this software, there are two types of curve fitting routines used. In fit#1 the regions where the dT data are rapidly changing in time are not used, but

an upper and lower region of the dT vs. dV data are independently fit and an average of the fits between the upper and lower slopes/arrays is calculated. Fit#2 is the linear fit to the overall slope/array of data.

Figure 4.26 shows the result of the manual run of the molybdenum sample. The difference between the two thermopower curve fits is due to the looping that occurred in the plot. The looping is usually caused by unstable temperatures but it also can be caused by the difference in cooling and heating rate across the sample and on the quality of the thermal interface between the sample and the cryostat sample stage. When looping is not apparent in the data, then fit#2 is less susceptible, noise in the data and will give a better result than fit #1. In Figure 4.29, the shape of the slope has changed due to temperature instabilies. Fit#1 is now a much better fit than fit#2.

Figure 4.30 shows the transition between temperatures during the automated temperature measurement. It is obvious that small oscillations have occurred and this has affected the measurement. Figure 4.31 shows the distortions in the temperature gradient plot and slope caused by the oscillation of the temperatures.

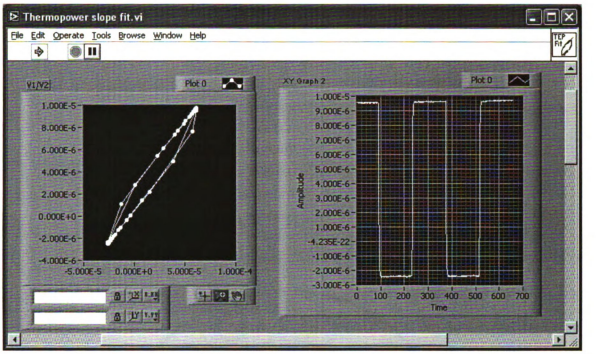

Figure 4. 29 At 530K, the value of Mo is displayed in Thermopower slope fit.vi

Figure 4. 30 The transition between temperatures during the temperature dependent measurement.

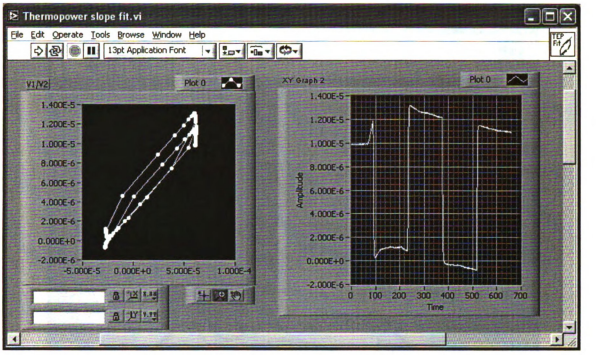

Figure 4. 31 Distorted plots due to temperature instability.

When distorted waveforms are observed, the system has to be re-tuned for better temperature stabilization. Try to choose a reasonable value for P so oscillation will occur. In this case, the PID was set to 100, 0, 0 with a new P value that is twice the old P value. Remember to do the tuning in the beginning of the next set temperature. If the amplitude of the oscillation decreases, change the P to a higher value, like 150. In Figure 4.32, a white straight line indicated when the PID is changed to 100, 0, 0.

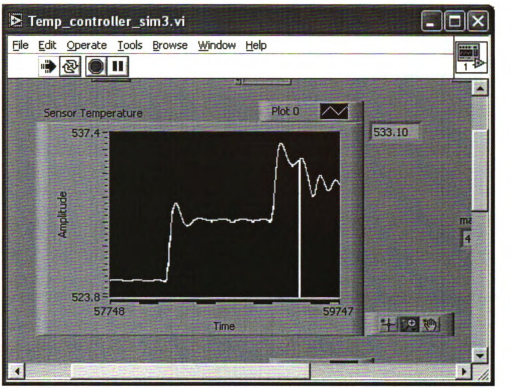

Figure 4. 32 Reset the PID values to 100, 0, 0. The white vertical line indicated when the PID was changed.

After the PID was tuned to 100, 0, 0, the oscillation occurred but with a decreasing amplitude in time as shown in Figure 4.33. Now, re-tune the PID to 150, 0, 0, this will allow more power to the controller. In Figure 4.34, the system obtains oscillations with constant amplitude. The plot is then magnified so the period of oscillation can be determined since this will be used to determine the I and D values. Figures 4.35 and 4.36 have shown the different magnifications of the waveform.

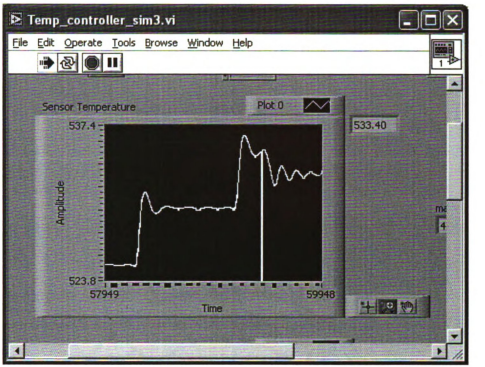

Figure 4. 33 The amplitude of the oscillation decreases.

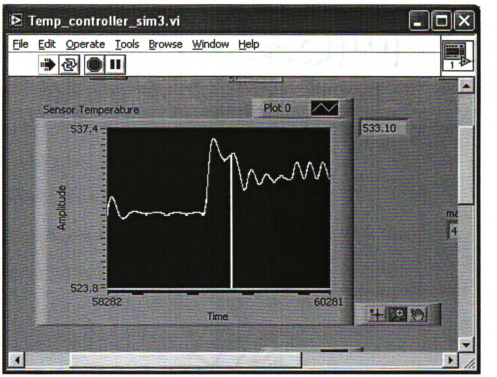

Figure 4. 34 The PID is reset to 150, 0, 0 and it then sustains a constant amplitude oscillation.

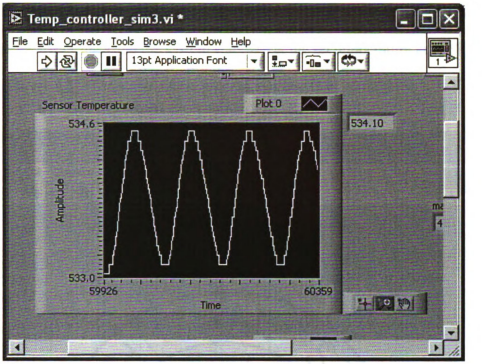

Figure 4. 35 The magnified view of the oscillation.

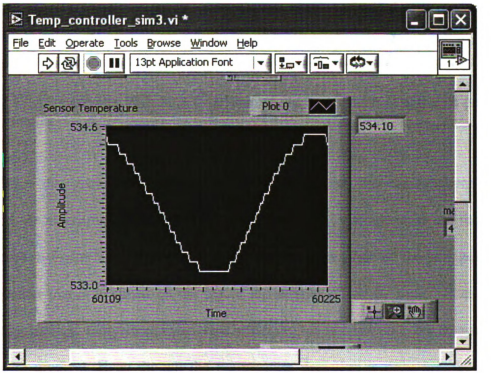

Figure 4. 36 Calculate the period, period=116s.

The period was calculated to be 116 second and thus the new PID is 50, 8, 29. With the new PID values and the system stablizes at the set temperature at 535K as shown in Figure 4.37. The stabilization process was less than 10 minutes.

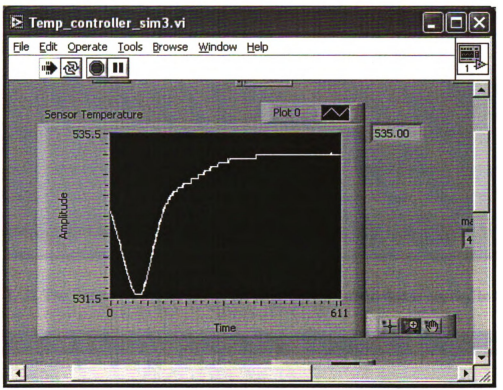

Figure 4. 37 After the new PID: 50,8,29 is entered, the system stables at the set point less than 10 minutes.

Once the system is stable at the set temperature, the measurement can be continued. As an example, in a measurement for this study, a temperature oscillation was observed as in Figure 4.38. This temperature oscillation is affect by the heat pulse from the HT heater that is mounted on the top of the sample. Since the sample that is being measured is a metal, molybdenum, a larger heater current is required to create a sufficient temperature gradient. Even though the temperature deviation is only + /- 0.2 K, it is enough to create looping in the measurement as shown in Figure 4.39.

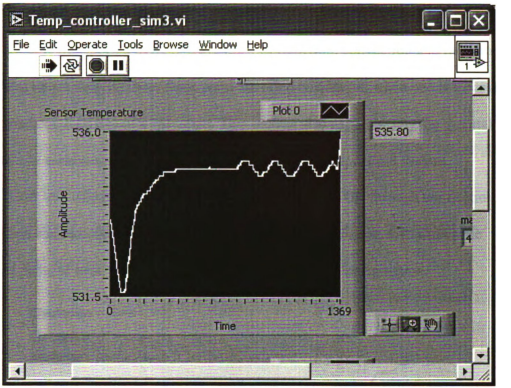

Figure 4. 38 The instability occurs due to the large heater current that is applied to the sample.

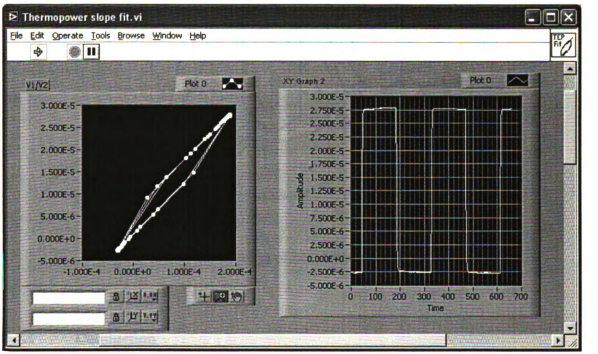

Figure 4. 39. Looping occurs due to the instability of the system.

4.7 Thermal Loss Calculation

Heat is transported in three ways [56]: Conduction, convection and radiation. Thus, heat losses through these three ways are often considered when one is measuring the thermal conductivity of a specimen. This section also explains why the thermal conductivity measurement is not considered in the high temperature system.

Heat loss calculations at room temperature and at 800K through conduction, convection and radiation will be performed in this section. Figure 4.40 shows the different paths of heat loss in the high temperature sample configuration.

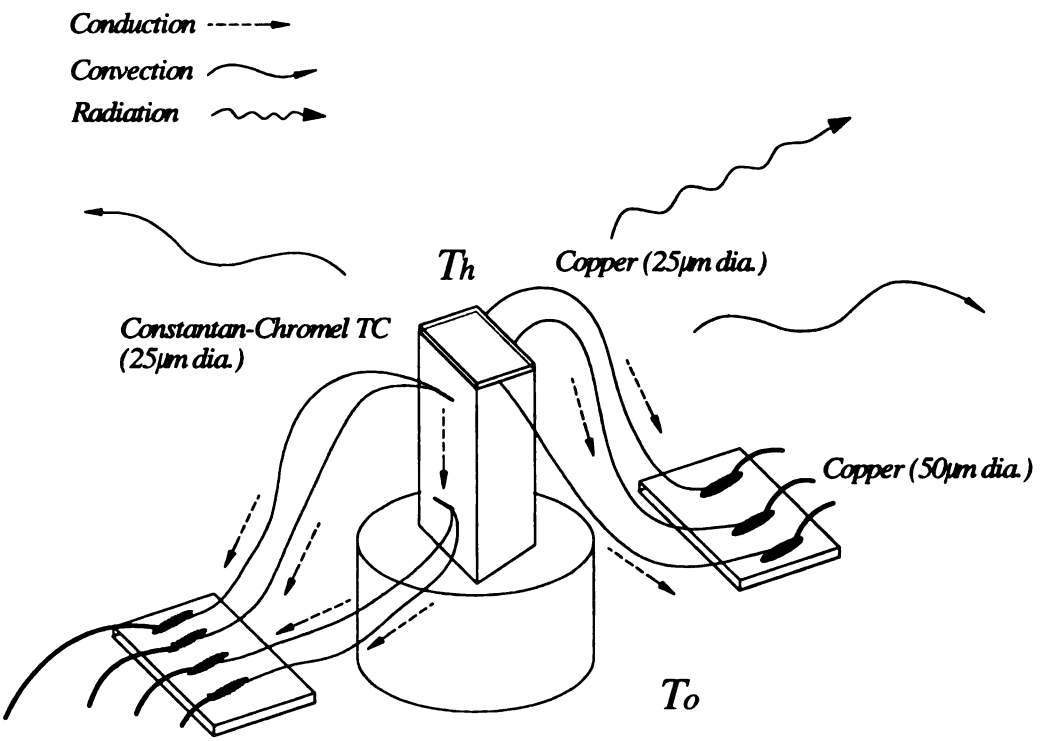

Figure 4. 40 Various ways of heat transfer from the sample.

4.7.1 Conduction

The equation for heat conduction is

$$Q_{cond} = \kappa(T_h - T_o)\frac{A}{l}$$

and the thermal conductance is equal to $\kappa\frac{A}{l}$.

There are three 25μm diameter copper wires, two 25μm constantan wires and two 25μm chromel wires required in the HT system and all these wires are connected to thicker (50μm diameter) copper wires with silver paint. Table 4.1 and 4.2 are the electrical and thermal properties of various metals and alloys.

Material	Electrical Resistivity (10^{-8} Ωm) @300K	Thermal Conductivity (W/m·K) @300K
Copper (Cu)	1.725 [57]	401 [57]
Nickel (Ni)	7.2 [57]	90.7 [57]
Chromium (Cr)	12.7 [57]	93.7 [57]
Constantan (Ni45Cu55)	52 [58]	19.5 [58]
Chromel (Ni90Cr10)	70.6 [58]	19 [58]

Table 4. 1 The electrical resistivity and thermal conductivity of some metals and alloys at room temperature.

Material	Electrical Resistivity (10^{-8} Ωm) @800K	Thermal Conductivity (W/m·K) @800K
Copper (Cu)	5.262 [57]	366 [57]
Nickel (Ni)	35.5 [57]	67.6 [57]
Chromium (Cr)	34.6 [57]	71.3 [57]

Table 4. 2 The electrical resistivity and thermal conductivity of some metals and alloys at 800K.

At room temperature (300K), the thermal conductance for each copper wire (3 cm long) is $401*\pi*(12.5\mu)^2/0.03 = 6.56$ μW/K

For three Cu wires, the thermal conductance is 19.68 μW/K. Similar calculations can be applied to other metal wires. Table 4.3 shows the result of the thermal conductance of each wire at 300K.

Material (3 cm long)	Thermal Conductance (μW/ K) @300K	Total Thermal Conductance (μW/ K)
Copper (Cu)	6.56	6.56*3 = 19.68
Constantan (Ni45Cu55)	0.319	0.319*2 = 0.638
Chromel (Ni90Cr10)	0.31	0.31*2 = 0.62
	Total	**20.938**

Table 4. 3 The thermal conductance of each wire at 300K.

Since the thermal and electrical properties of chromel at high temperatures were not found in the literature, a simple method can be used to estimate the values based on the available properties of nickel.

This method is called Nordheim rule [59], and is used to predict the resistivity of an alloy. The Nordheim rule relates the alloy resistivity, ρ_{alloy} (in this case, chromel), to the atomic fraction X of the solute atoms (Nickel) in a solid solution.

$$\rho_{alloy} = \rho_{matrix} + CX(1-X)$$

where C is the Nordheim coefficient. There is an important assumption in this rule which is that the alloying does not significantly vary the number of conduction electrons per atom in the alloy. Even though, it is only true for the alloys with the same valency, i.e. from the same column in the Periodic chart, it still gives very good prediction for dilute alloys. In this case, we consider chromel to be a dilute alloy since the impurity (chromium) is only 10%.

In order to find the thermal conductivity value of Chromel at 800K, the Nordheim coefficient can be determined from the room temperature values by assuming the Nordheim coefficient is constant between these temperature ranges. At 300K, the resistivity of Chromel is 70.6×10^{-8} Ωm, nickel is 7.2×10^{-8} Ωm and Chromel has the composition of 90% nickel and 10% Chromium. So the equation becomes

$$70.6 \times 10^{-8} = 7.2 \times 10^{-8} + C(0.1)(1-0.1)$$

$$\mathbf{C = 7.04 \times 10^{-8}\ \Omega m}$$

Once C is found, the high temperature value for the resistivity is

$$\rho_{chromel} = 35.5 \times 10^{-8} + 7.04 \times 10^{-8} \times (0.1)(1-0.1)$$

$$= 9.886 \times 10^{-7} \Omega m$$

The thermal conductivity of Chromel at 800K can be found from the Wiedemann-Franz-Lorenz Law, which gives

$$\kappa_{chromel} = \sigma T L$$

$$= TL / \rho_{chromel}$$

$$= 800 * 2.44 \times 10^{-8} / 9.886 \times 10^{-7}$$

$$= 19.745 \text{ W/m K}$$

This value is very similar to the nickel alloys $Ni_{80}Cr_{20}$ as shown in Figure 4.41 and it shows that the estimation is pretty good.

The experimental value of thermal conductivity of Constantan from 80-400K is shown in Figure 4.42 and the 800K value was obtained by extrapolating from the curve fit as shown in Figure 4.43. The thermal conductivity at 800K is about 130 W/m K. If using the Nordheim rule, we obtained about 119 W/mK. Figure 4.44 shows the

temperature dependent thermal conductivity[57] of copper. For a temperature gradient of 1 K, the thermal conductance of copper is shown in Figure 4.45.

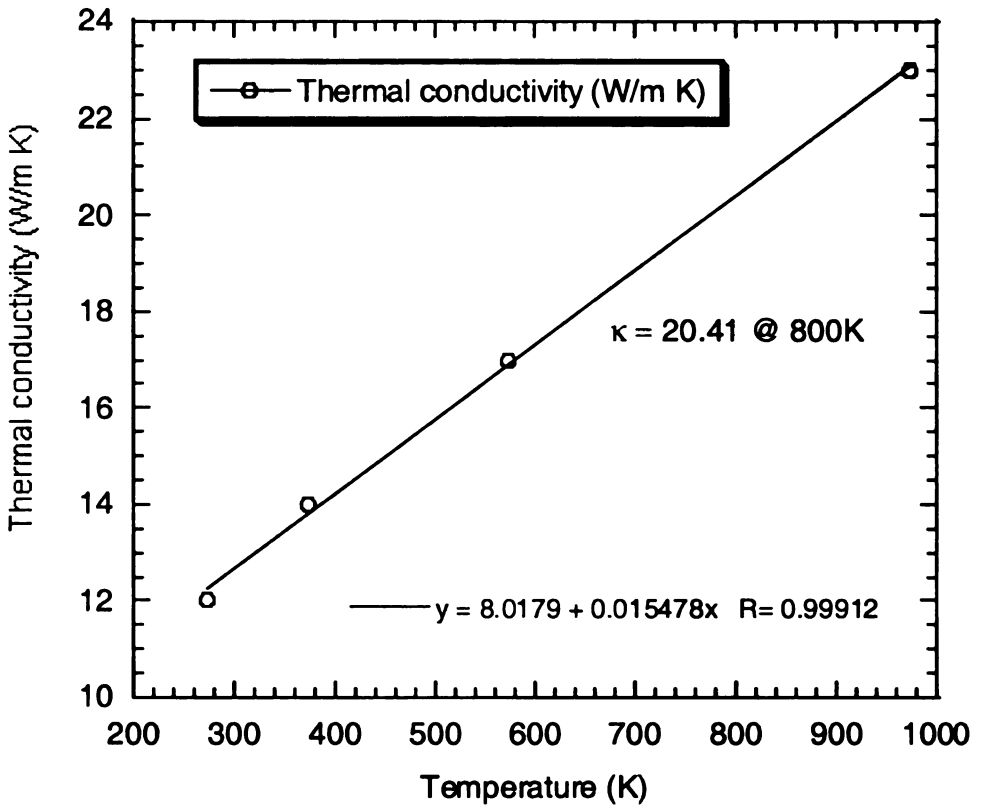

Figure 4. 41 The thermal conductivity of Cr_{20} Ni_{80}.

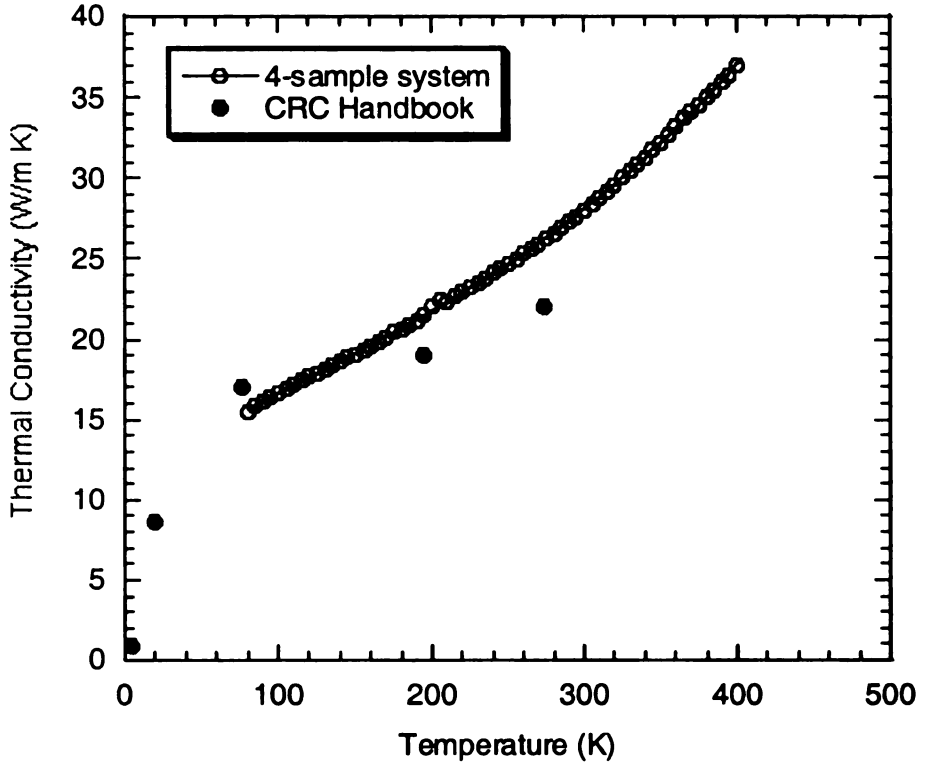

Figure 4. 42 The comparison between the Reference and 4-sample system measurement in thermal conductivity of constantan.

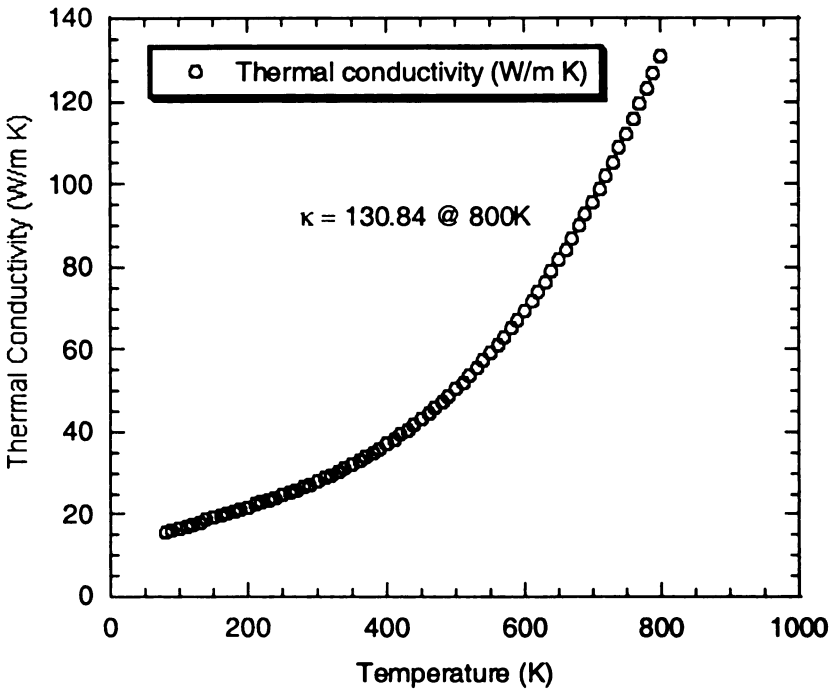

Figure 4. 43 Use the curve fit equation in Figure 4.42 to extrapolate the thermal conductivity of constantan at 800K.

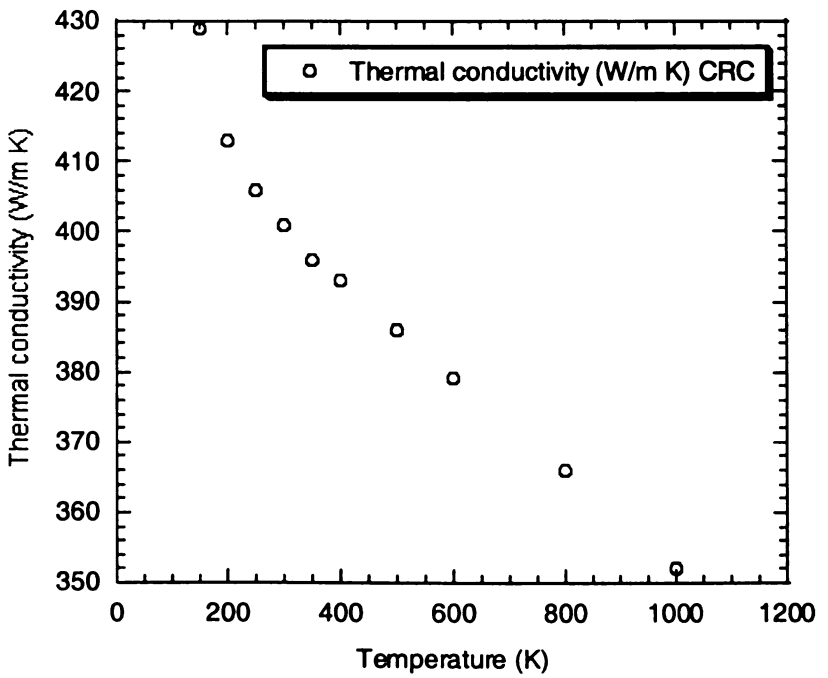

Figure 4. 44 Thermal conductivity of Copper

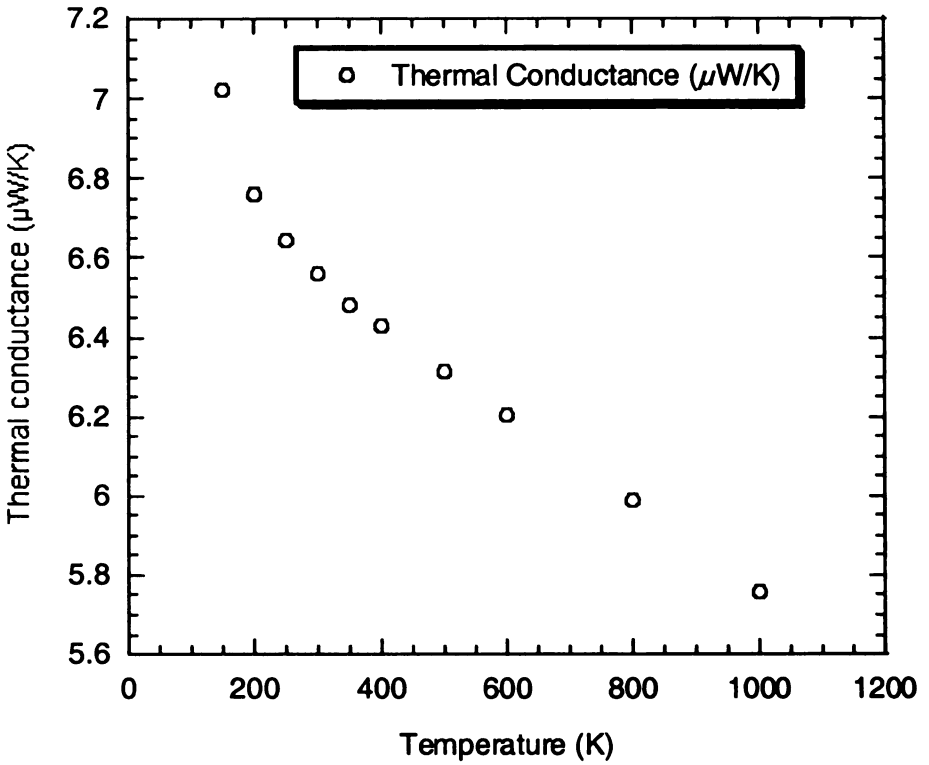

Figure 4. 45 Thermal conductance of Copper, assuming a temperature gradient of 1K.

Table 4.4 has listed the thermal conductance of each wire at 800K. The total thermal conductance of all wires at 300K and 800K are very similar, in the range of μW/ K.

Material (3 cm long)	Thermal Conductivity (W/m K) @800K	Thermal Conductance (μW/ K) @800K	Total Thermal Conductance (μW/ K)
Copper (Cu)	366	5.98	5.98*3 = 17.94
Constantan (Ni45Cu55)	130.84	2.127	2.127*2 = 4.254
Chromel (Ni90Cr10)	19.745	0.323	0.323*2 = 0.646
		Total	**22.84**

Table 4. 4 The thermal conductance of each wire at 800K.

4.7

to a

fron

whe

is th

mole

coeff

The

is 29

For

Q_{con}

is 14

R_{univ}

So f

$\gamma = 2$

At 3

4.7.2 Convection

At low pressure (< 10^{-4} Torr), the gas molecules generally travel from one place to another without colliding with other molecules. These gas molecules will transfer heat from a surface at temperature T_h to a parallel surface at T_c at a rate Q per unit area, thus

$$Q_{conv} = a\frac{\gamma+1}{\gamma-1}\sqrt{\frac{R}{8\pi}}\frac{P}{\sqrt{MT}}(T_h - T_c)$$

where γ is the ratio of *Cp/Cv*, *Cp* is the specific heat capacity at constant pressure and *Cv* is the specific heat capacity at constant volume. *P* is pressure in Torr and *M* is the molecule weight of the gas, *a* is an accommodation coefficient related to individual coefficients. For dirty surfaces, *a* approaches a maximum value of 1. *R* is the gas constant The specific heat capacity, *Cp* of nitrogen is 1.04 J/gK and the molar heat capacity of N_2 is 29.124 J/mol K.

For most measurements, pressures in the range below 10^{-5} Torr are sufficient to make Q_{conv} negligible. In our case, assume *a* is 1 and the residual gas is nitrogen (atomic weight is 14), the pressure is 10^{-5} Torr and at 300K,

$R_{univ} = C_p - C_v = 8.3143$ J/mol K

So for nitrogen $C_v = 29.124 - 8.3143 = 20.8097$ J/mol K

$\gamma = 29.124/20.8097 \sim 1.4$

At 300K, assume $T_h - T_c = 1$K

$$Q_{conv} = 1\times\frac{1.4+1}{1.4-1}\sqrt{\frac{8.3143}{8\pi}}\frac{10^{-5}\times 133.32}{\sqrt{14*2*300}}(1)$$

$$= 157.7\ \mu W/m^2$$

$$= 15.77\ nW/cm^2$$

At

So

Thu

4.7.

of th

radi

seco

near

100F

an ic

are 7

Assu

temp

At 80

At 800K, $Q_{conv} = 96.58\ \mu W/m^2 = 9.658\ nW/\ cm^2$

So for a one centimeter square surface area, the heat loss is only in nano watts range. Thus, at high enough vacuum, heat convection can be neglected.

4.7.3 Radiation

A black body has a surface emissivity of 1. It means that this body will absorb all of the thermal radiation to it. When this body is heated up, it will emit all the thermal radiation it has. At some temperature, T, a black body emits radiant energy, $E = \sigma T^4$ per second per unit area, where σ is the Stefan constant, 5.7×10^{-8} W/m^2 K^4. At temperature near absolute zero, such losses are small but they become more significant at above 100K.

Surface emissivity, ε, is the relative emissive power of a body compare to that of an ideal blackbody.

If the emissivities are equal for the shield and the sample, and their temperatures are T_{shield} and T_{sample}. The radiation heat loss is

$$Q_{rad} = \frac{\sigma\varepsilon}{2-\varepsilon}\left(T_{sample}^4 - T_{shield}^4\right)$$

Assume a sample with an ε of 1, and the sample temperature is 301K and shield temperature is 300K. So

$$Q_{rad} = \frac{5.7*10^{-8}\times 1}{2-1}\left(301^4 - 300^4\right)$$

$$= 6.1868\ W/m^2$$

$$= 618.68\ \mu W/cm^2$$

At 800K, the radiation becomes

bec

me

me

$$Q_{rad} = \frac{5.7 * 10^{-8} \times 1}{2-1}\left(800^4 - 799^4\right)$$

$$= 116.5 \text{ W/m}^2$$

$$= 11.65 \text{ mW/cm}^2$$

So for a one centimeter square surface area, the heat loss through radiation becomes very large and it is difficult to eliminate this loss in thermal conductivity measurement at high temperature. It is for this reason that thermal conductivity measurements have not been pursued in this high temperature system.

Chapter 5 Experimental Results

The high temperature system is designed to investigate cubic materials which perform well at high temperatures. The result of one of the first samples received by the lab is shown in Figure 5.1. This cubic material, $Ag_{0.8}Pb_{10}Sb_{0.88}Bi_{0.02}Te_{12}$, exhibits electrical conductivity of about 700 S/cm and a thermopower value of –150 μV/K at room temperature (300K). The negative value of thermopower indicates that it is an *n*-type semiconductor material. The thermoelectric power value at high temperatures has approached -300 μV/K which is very encouraging, while the electrical conductivity decreases with temperature. This is indicative of metallic behavior. The sudden turning point of the thermopower measurement at 680K was unexpected. Though some materials exhibit a minimum or maximum in the thermopower values, the curve showed in Figure 5.1 was not symmetric about the peak as would normally be expected.

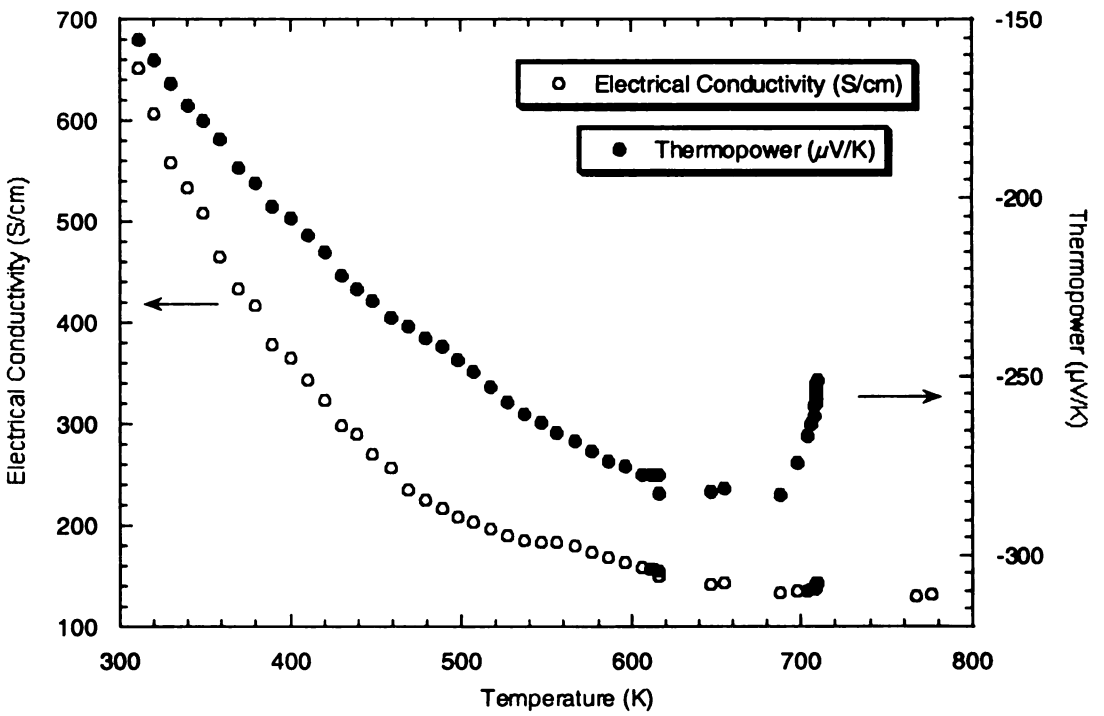

Figure 5. 1 The electrical conductivity and thermopower of $Ag_{0.8}Pb_{10}Sb_{0.88}Bi_{0.02}Te_{12}$

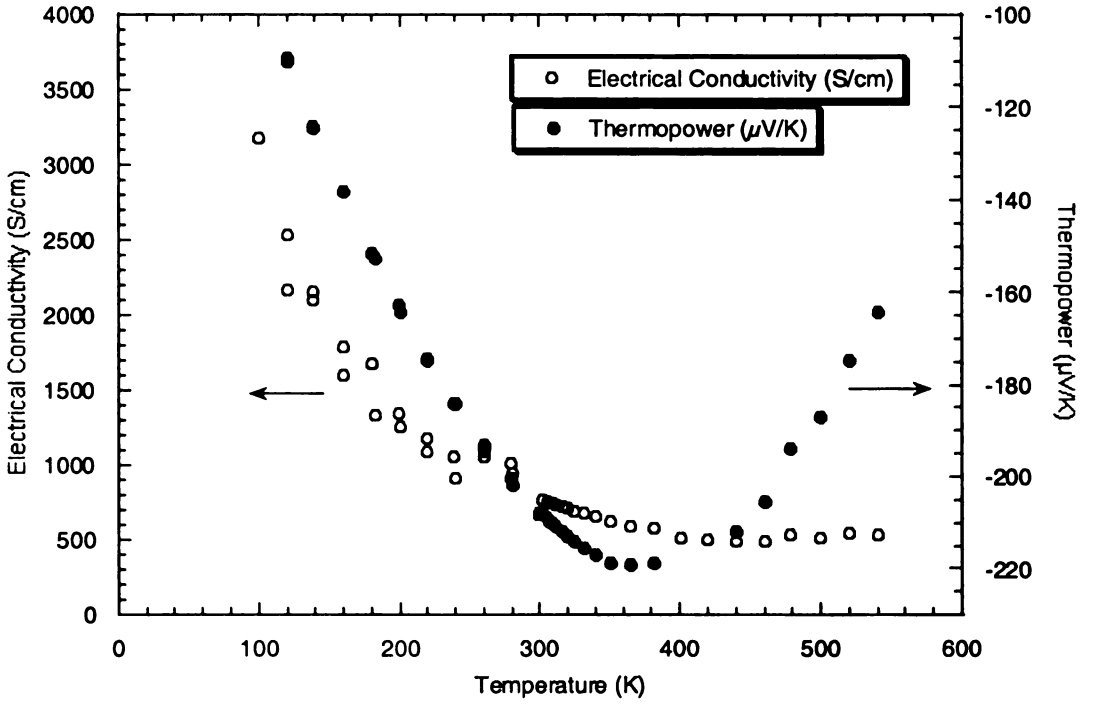

Figure 5. 2 Electrical conductivity and thermopower of Bi_2Te_3.

A standard material, bismuth telluride, was measured in the system again to verify the performance of the system. In Figure 5.2, the measured values of bismuth telluride agree very well with the reference data. A sample of a third material, $Ag_{0.78}Pb_{18}SbTe_{20}$, was mounted and tested but the turning point was still observed where it was not expected, and it happened at the same temperature as seen in Figure 5.1. This indicated a problem with the measurement, either in the system or the sample mounting, at that particular temperature. Figure 5.3 shows a repeated measurement to confirm that the turning point did not appear randomly. Again there is an upturn in the data for the points above approximately 660K, however based on measurements for the Bi_2Te_3 reference material (Figure 5.2) it is expected that the results on this sample are accurate for the

300-660K range in Figure 5.3. Further investigations were necessary for the data points above this temperature range.

This material has a higher composition of lead and tellurium and did not contain bismuth. It has higher values of electrical conductivity and thermopower at room temperature compared to the $Ag_{0.8}Pb_{10}Sb_{0.88}Bi_{0.02}Te_{12}$.

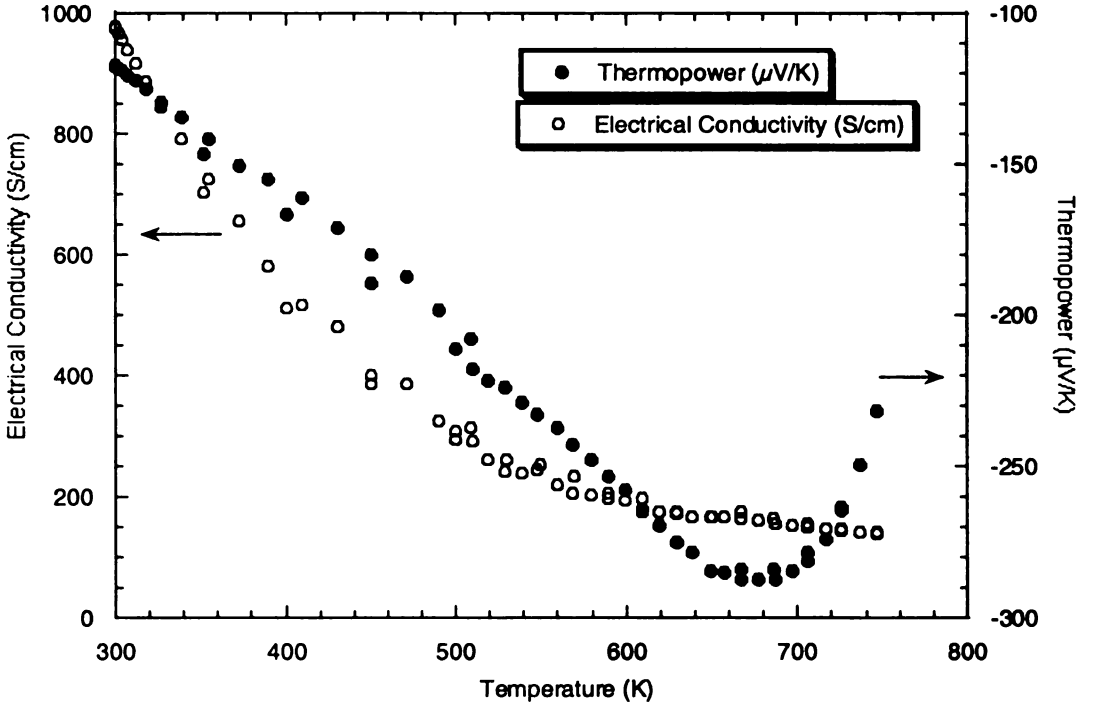

Figure 5. 3 Electrical conductivity and thermopower of $Ag_{0.78}Pb_{18}SbTe_{20}$

After some investigation, it was discovered that the problem associated with the data above 660K came from the type of thermocouple used in the measurement. The type T thermocouples (copper-constantan TC) that were used in these measurements are not rated for high temperature applications, and the polynomial used for converting the thermocouple voltage to a temperature was valid only up to 660 K. The temperature gradient across the sample is determined by comparing the voltage drop across the

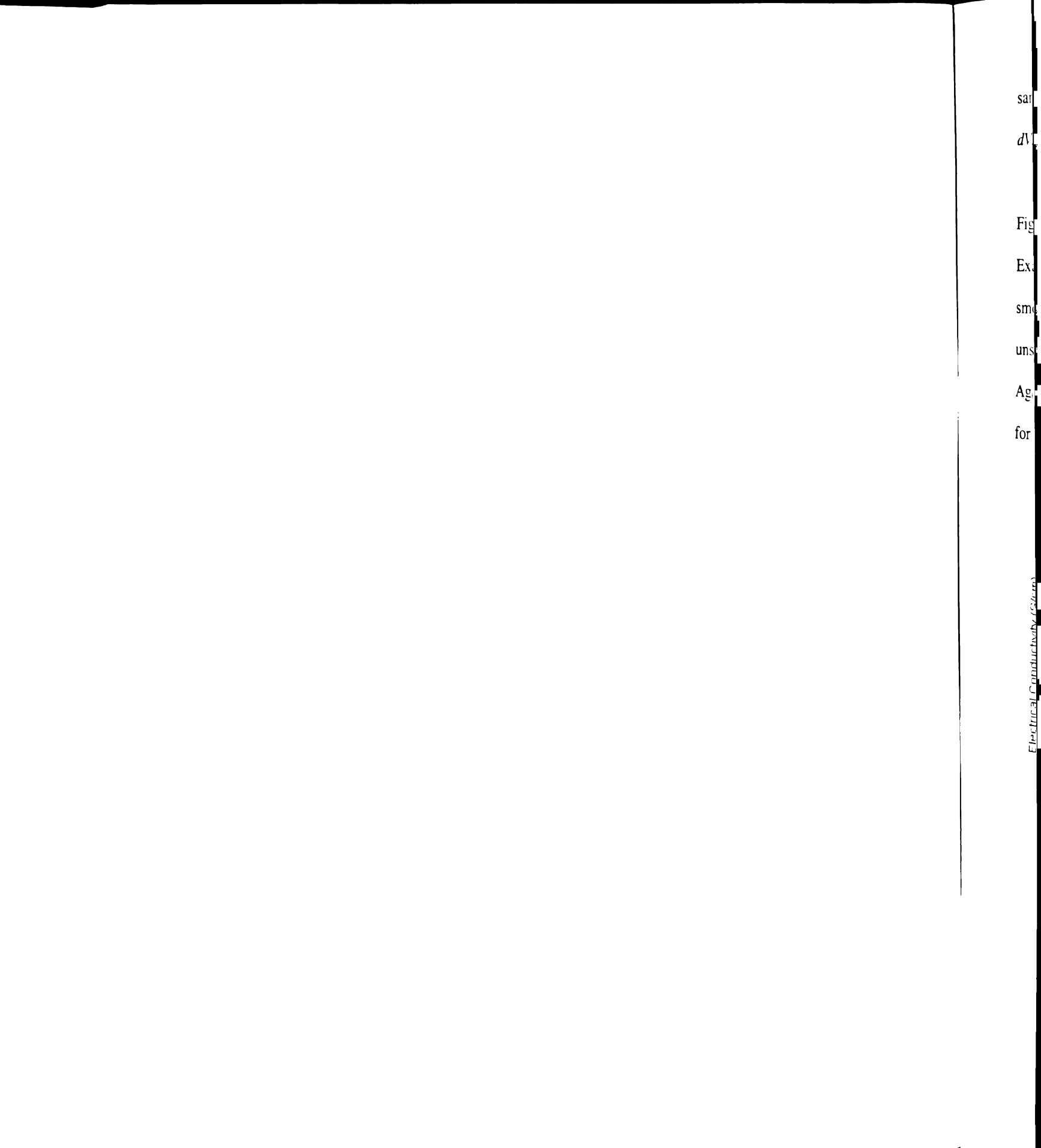

sample to the derivative (*dV/dT*) of the absolute voltage drop of the thermocouple. The *dV/dT* curve of the type T thermocouples has a sharp drop above 660K.

Type K thermocouples (Chromel-Alumel thermocouples) were used next and Figure 5.4 shows one of the results of a sample mounting with this type of thermocouple. Examination of the *dV/dT* curve of the type K thermocouple, however, is not very smooth, which can cause large errors in the *dT* value if the temperature is slightly unstable. In Figure 5.4, the sample has the same composition as the sample in Figure 5.3, $Ag_{0.78}Pb_{18}SbTe_{20}$, though; the electrical conductivity is much higher (about 1000 S/cm) for the latter material.

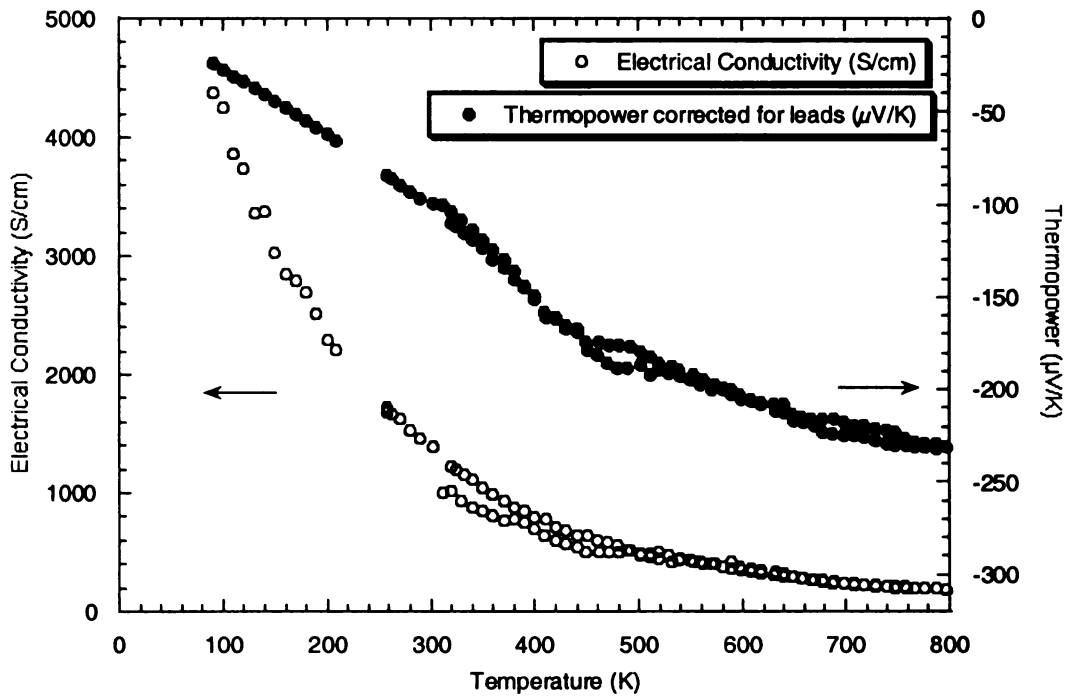

Figure 5. 4 Electrical conductivity and thermopower of $Ag_{0.78}Pb_{18}SbTe_{20}$

One thing that needs to be noted is that the PID temperature control of this system was not properly tuned yet. Therefore, the type K thermocouple was not suitable for use then.

Finally, a Type E TC (Chromel-Constantan) was used for its very smooth derivative curve. Figure 5.5, 5.6 and 5.7 are results of the reference samples – Bismuth Telluride and constantan foil. The figures show the comparison between the 4-sample system and the high temperature system. The 4-sample system [60] is a well-established low temperature (80-400 K) TE measurement system in the lab. It is used to verify the functionality of the high temperature system. In Figure 5.5, the maximum thermopower of bismuth telluride is -227 μV/K at 390K. According to Goldsmid [61], the energy band gap, E_g, can be determined from the maximum thermopower value and the corresponding temperature,

$$E_g = 2 \times e \times S_{max} \times T_{max}$$

From Figure 5.5, $E_g = 2 \times e \times 227 \times 390$

$$= 0.177 \text{ eV}$$

This band gap value agrees very well with the literature values of 0.17 eV [62].

Figu
syste

Figur
samp

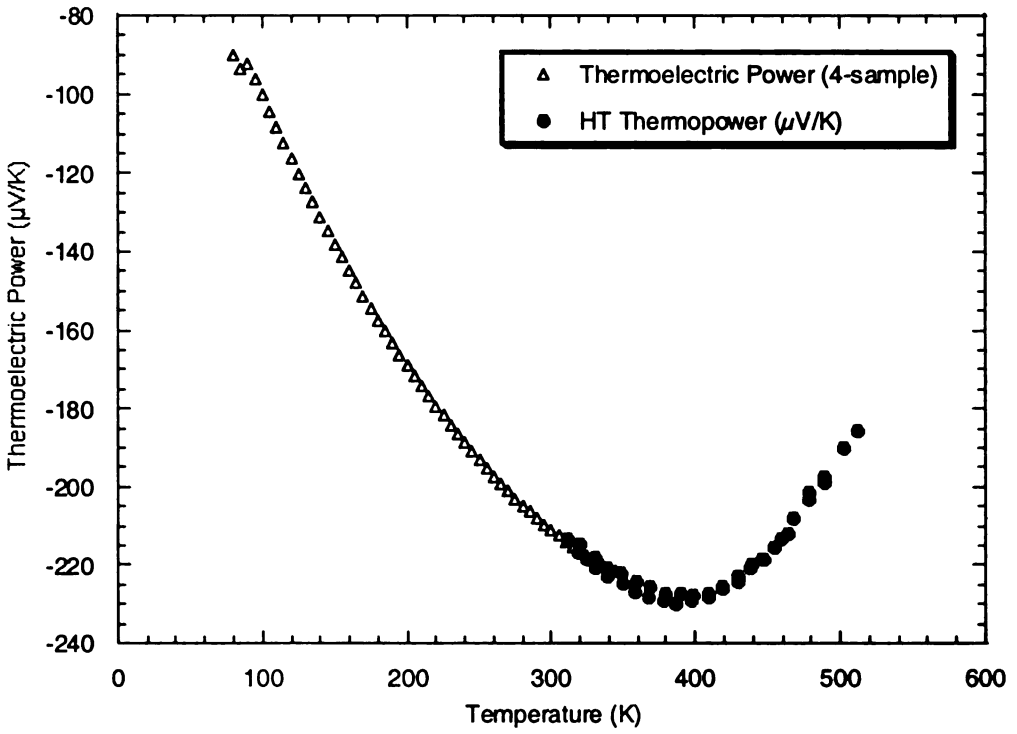

Figure 5. 5 The comparison of the thermopower of bismuth telluride between 4-sample system and high-temperature system.

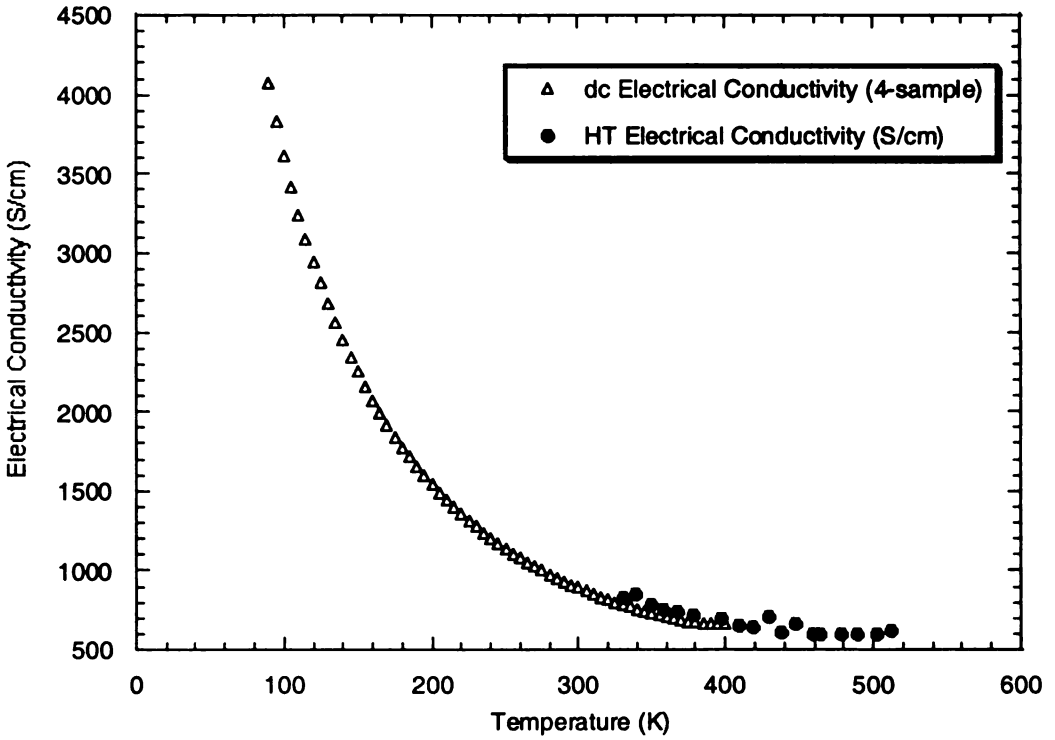

Figure 5. 6 The comparison of the electrical conductivity of bismuth telluride between 4-sample system and high-temperature system

wa

an

du

(di

per

in T

Figur

and h

In Figure 5.7, Constantan ($Cu_{55}Ni_{45}$ alloy) foil was measured in the system and was compared with the literature values. Negative thermopower values indicate that it is an *n*-type alloy. The small disagreement occurred at higher temperatures which might be due to the shape and/or purity of the sample – voltage and temperature gradient (distribution) across a foil might be slightly different than those across a wire. The error percentage of this measurement can be obtained from

Error% = (Reference – Measured)/Reference

The error percentage of the HT Constantan thermopower measurement is shown in Table 5.1. The overall error percentage of this measurement falls between 5-8%.

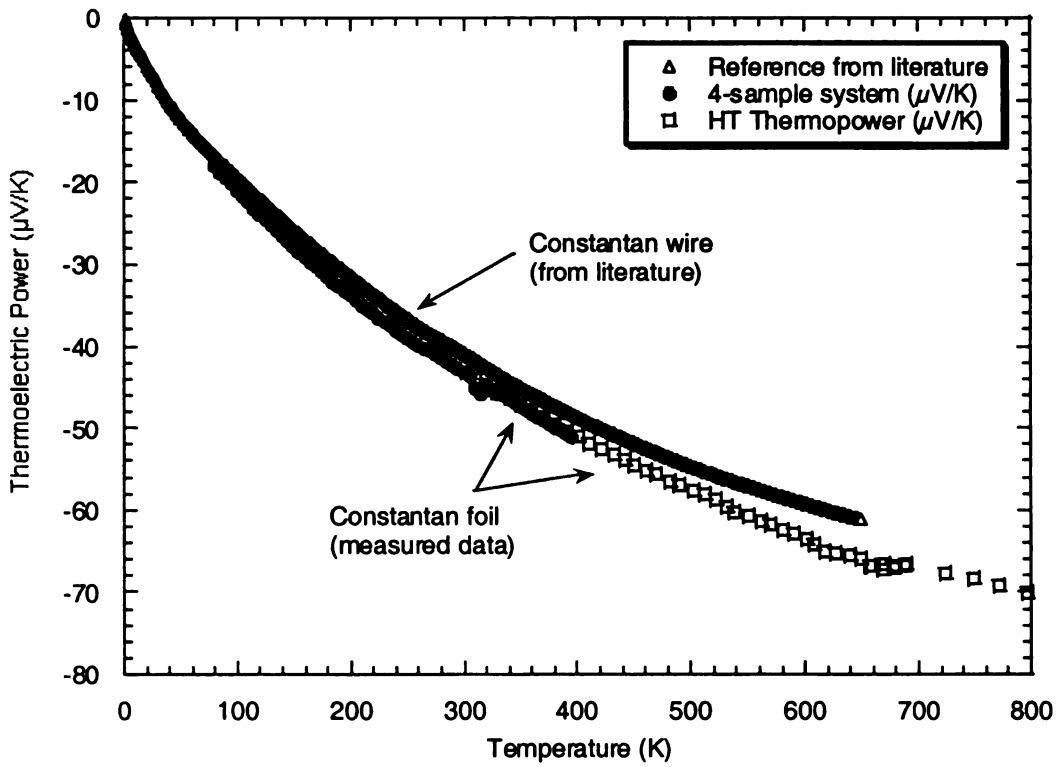

Figure 5. 7 The comparison of the thermopower of Constantan between 4-sample system and high-temperature system to the literature values.

Temperature (K)	Reference TEP (μV/K)	Measured TEP (μV/K)	Error %
302	- 41	- 43.207	5.38%
502	-54.72	-57.654	5.24%
649	-61.13	-65.99	7.95%

Table 5. 1 Error percentage calculation of the HT Constantan thermopower measurement.

Cubic materials are the main focus when the high temperature system is ready for measurement. Silver paste was used as an electrically and thermally conductive adhesive. In one case, however, the surface of the sample showed a change in which the composition of the sample was found to be more silver rich after the run, than before the run. To eliminate the possibility that the excess silver was from the silver paste, other conductive pastes were used. Figure 5.8 shows the electrical conductivity and thermopower data of the cubic sample KF2229R1D ($Ag_{0.82}Pb_{18}SbTe_{20}$) from 300-700K. The result agreed very well with the 4-sample system and the percentage error of the HT system measurement for this sample is in Table 5.2. However, the properties of the sample changed after it was heated to 780K. Figure 5.9 shows the change of properties as the sample was measured from 760K to 300K.

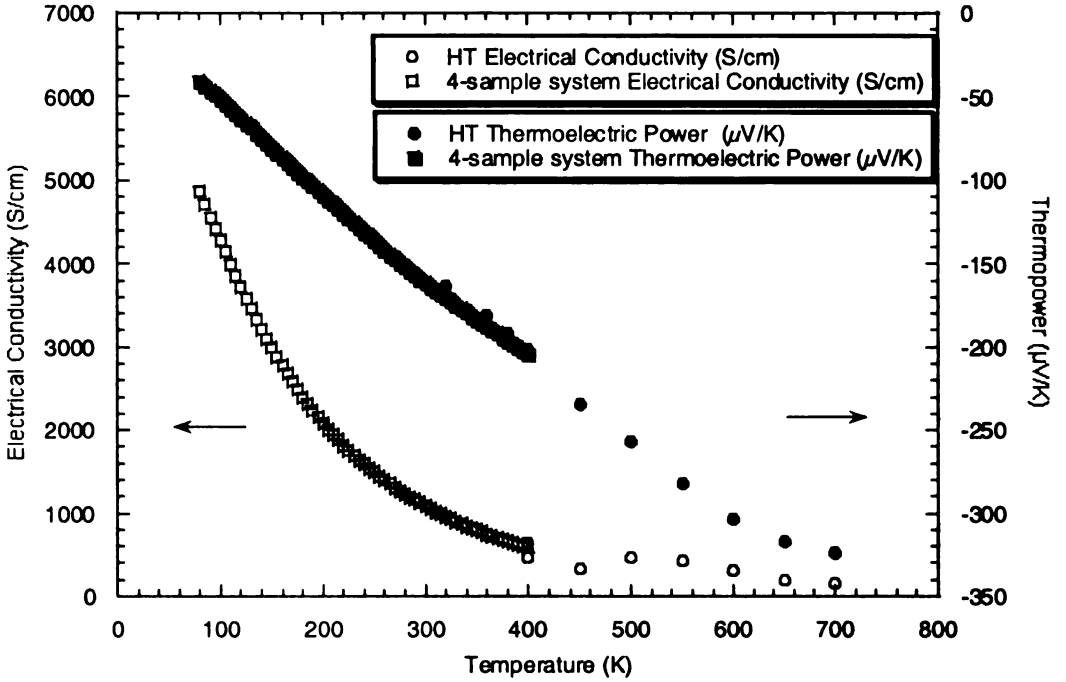

Figure 5. 8 The comparison of the electrical conductivity and thermopower of cubic material KF2229R1D between 4-sample system and high-temperature system (Oct. 25)

Temperature (K)	4-sample system		High T system		Error %	
	S (μV/K)	σ (S/cm)	S (μV/K)	σ (S/cm)	S (μV/K)	σ (S/cm)
320	-170.36	956.59	-163.37	960.13	4.1%	0.37%
400	- 204.52	587.77	- 201.22	640.86	1.6%	8.3%

Table 5. 2 Error percentage calculation of the sample KF2229R1D.

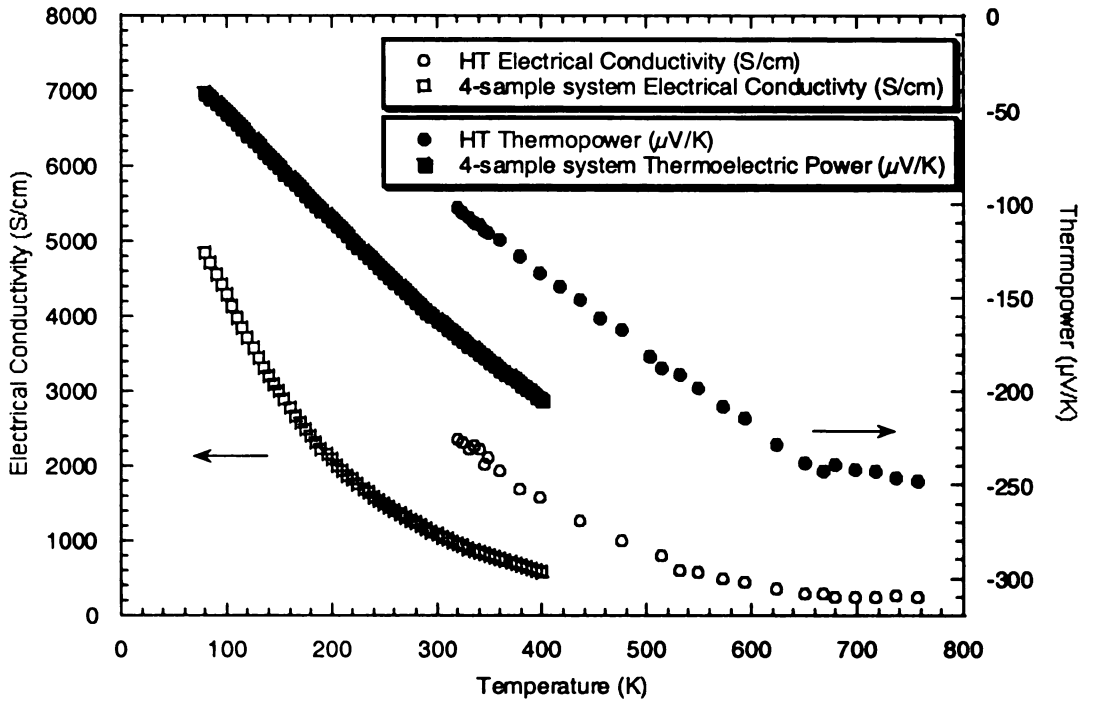

Figure 5. 9 The comparison of the electrical conductivity and thermopower of cubic material KF2229R1D between 4-sample system and high-temperature system (Oct. 26).

The scanning electron microscopy (SEM), energy dispersive spectrometry (EDS) analysis showed that the sample surface included excess silver as well as copper. An EDS comparison between the inside and the surface of the sample shows that it was a surface effect instead of total reaction throughout the whole sample. The EDS results are summarized in Table 5.3 and 5.4. It was believed that the extra silver might have come from the silver paint or that some of the other elements in the sample were evaporated from the surface layers at the high temperatures leaving the sample silver rich on the surface. For example, if tellurium was evaporated from the surface at the high temperatures, this would leave the samples surface with less tellurium, and with higher relative compositions of all other elements. In either case, the excess composition of

silver might have changed the measured voltages at the surface of the sample and caused the electrical conductivity to increase and thermopower to decrease.

Element	Atom%	Element Wt. %	Wt. % Error
Te	45.4	36.6	+/- 0.4
Pb	44.3	57.9	+/- 1.4
Ag	3.6	2.4	+/- 0.2
Cu	2.9	1.2	+/- 0.1

Table 5. 3 The EDS result for surface of the cubic materials KF2229R1D [63].

Element	Atom%	Element Wt. %	Wt. % Error
Te	49.8	38.6	+/- 0.8
Pb	48.2	60.6	+/- 8.1
Ag	0.3	0.2	+/- 0.2
Cu	0.3	0.1	+/- 0.4

Table 5. 4 The EDS result for inside of the cubic materials KF2229R1D [64].

It was rather difficult to determine where the copper elements came from. Even though the sample stage is made of OFHC copper, it is nickel/gold plated and it is difficult for the copper ions to penetrate into the sample through the nickel and gold layer. Furthermore, the change of color of the stainless steel bolts was observed, this is an indication of alloy annealing at high temperature. It is not known if elemental copper was released from the stainless steel during the annealing process.

Figu
KF2

are

pow

diffe

Figu

elect

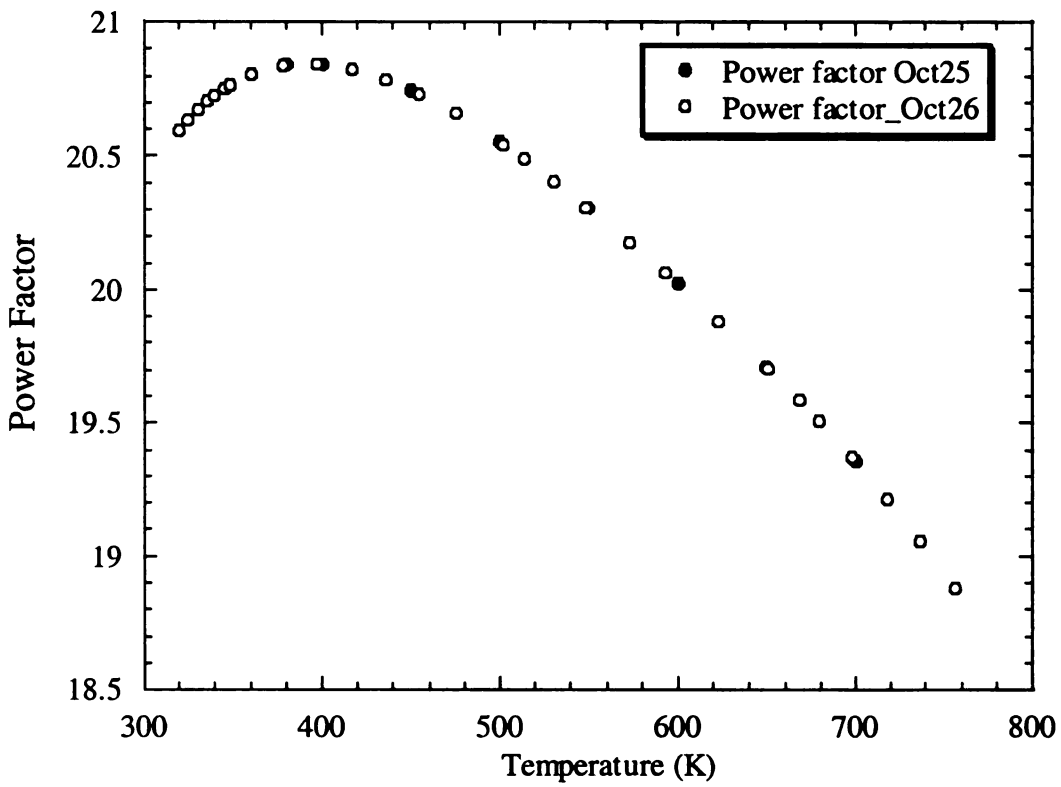

Figure 5. 10 The power factor comparison between the two runs (Oct. 25 & 26) of KF2229R1D.

Even though the thermopower and electrical conductivity values of KF2229R1D are different before and after heating to high temperatures, Figure 5.10 shows that the power factor appears the same. Another sample from the same ingot of KF2229R1D but different section is measured and similar surface composition problem occurred. Figure 5.11 shows the comparison of the 4-sample and high temperature system in electrical conductivity and thermopower of sample, KF2229R1C, from 300K to 700K.

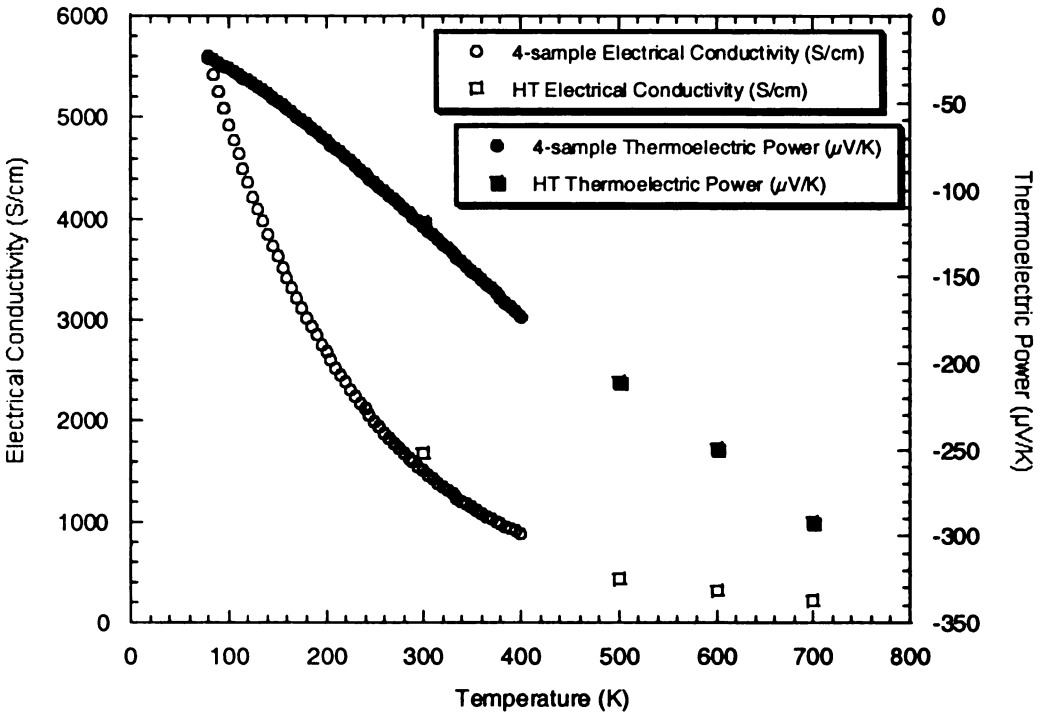

Figure 5. 11 The comparison of the electrical conductivity and thermopower of cubic material KF2229R1C between 4-sample system and high-temperature system [65].

After this experience, all stainless steel bolts were replaced with titanium bolts. The use of different paint for mounting, such as carbon and platinum paints, was also investigated. As has been stated in the experimental set-up section, silver paint was still determined to be the most suitable paint as long as the measurement is not on a cubic sample at more than 700K.

As a conclusion, most of these cubic materials have metallic-like electrical conductivity and the conductivity becomes constant at high temperatures while the thermopower values linearly increase as the temperature increases. Due to the high thermopower at high temperature, these compounds have great potential in TE power generation applications.

More reference materials were measured in the high temperature system to verify its performance. Figure 5.12 shows the thermopower measurement of 99.9% purity molybdenum and it agreed very well with the reference data found in Pollock [2]. This measurement was taken before the PID temperature controller was properly tuned so there were not many data points.

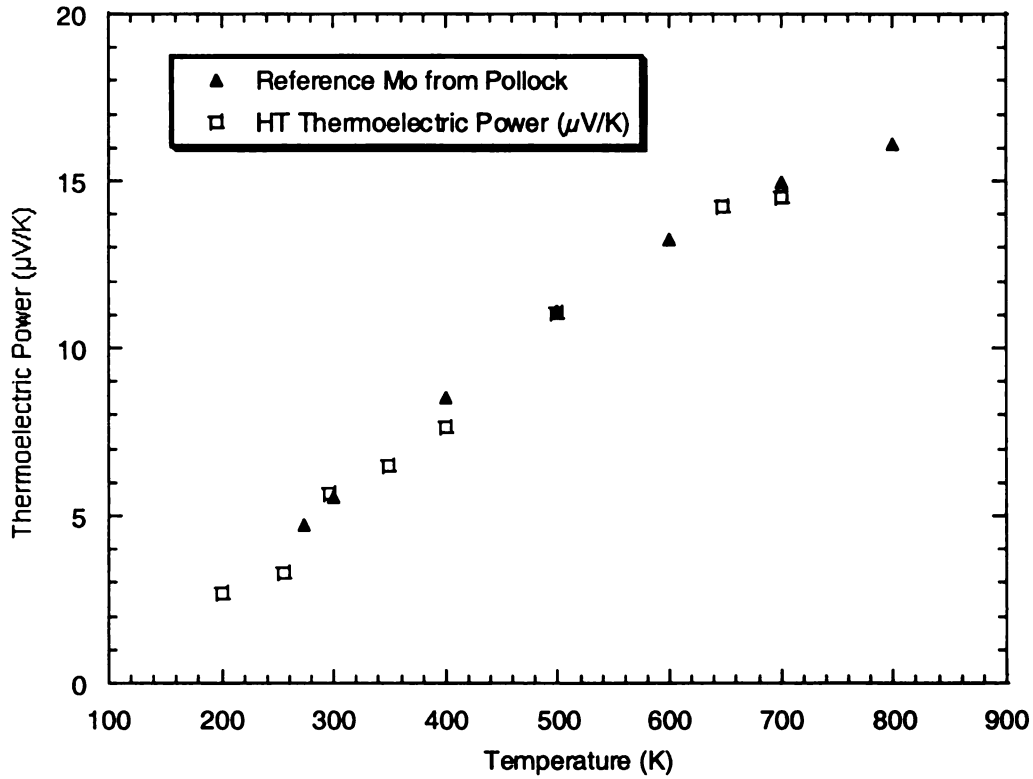

Figure 5. 12 The comparison of the thermopower of molybdenum between the reference (Pollock [2]) and high-temperature system (before the temperature controller is properly tuned).

After the temperature controller was properly tuned, large amount of data points were collected in each run. Figure 5.13 has shown another measurement of molybdenum after the proper tuning, the measured values agree very well with the reference, except that at lower temperatures, small deviation is shown. Table 5.5 shows the error percentage of HT system measurement for molybdenum. The deviation might results in

different purity between the sample and the reference. The discontinued data between 550-580K is due to unexpected electronic noise during the thermopower measurement, so those data has been removed.

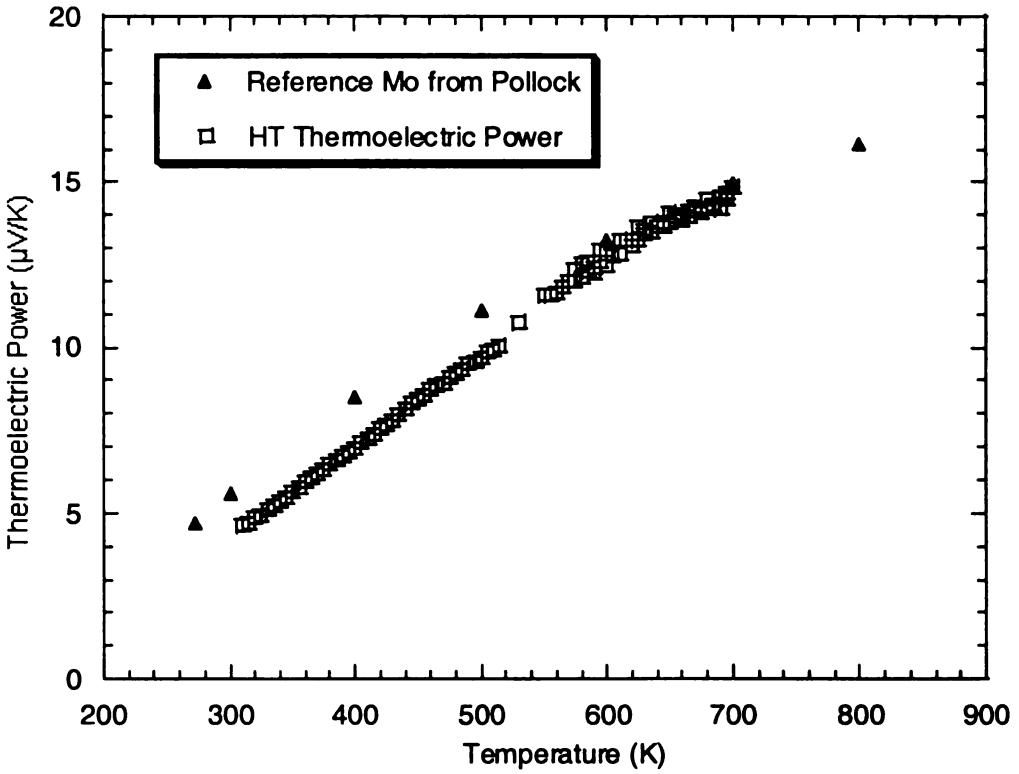

Figure 5. 13 The comparison of the thermopower of molybdenum between the reference (Pollock [2]) and high-temperature system (after the temperature controller is properly tuned).

Temperature (K)	Reference TEP (μV/K)	Measured TEP (μV/K)	Error %
400	8.52	6.973	18.16%
500	11.12	9.6987	12.78%
600	13.27	12.496	5.8%
700	14.94	14.821	0.8%

Table 5. 5 Error percentage calculation of the molybdenum HT thermopower measurement with the Reference.

The HT measured electrical resistivity data of molybdenum was also compared with the reference in Figure 5.14 and they agree very well as shown in Table 5.6.

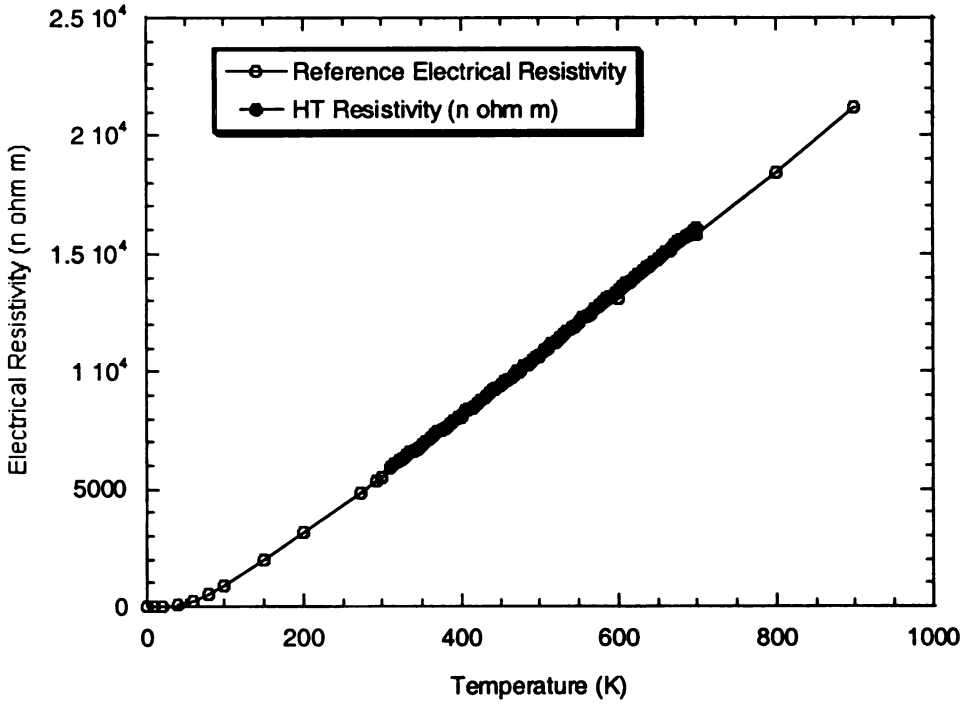

Figure 5. 14 The comparison between the reference [57] and measured electrical resistivity of Mo.

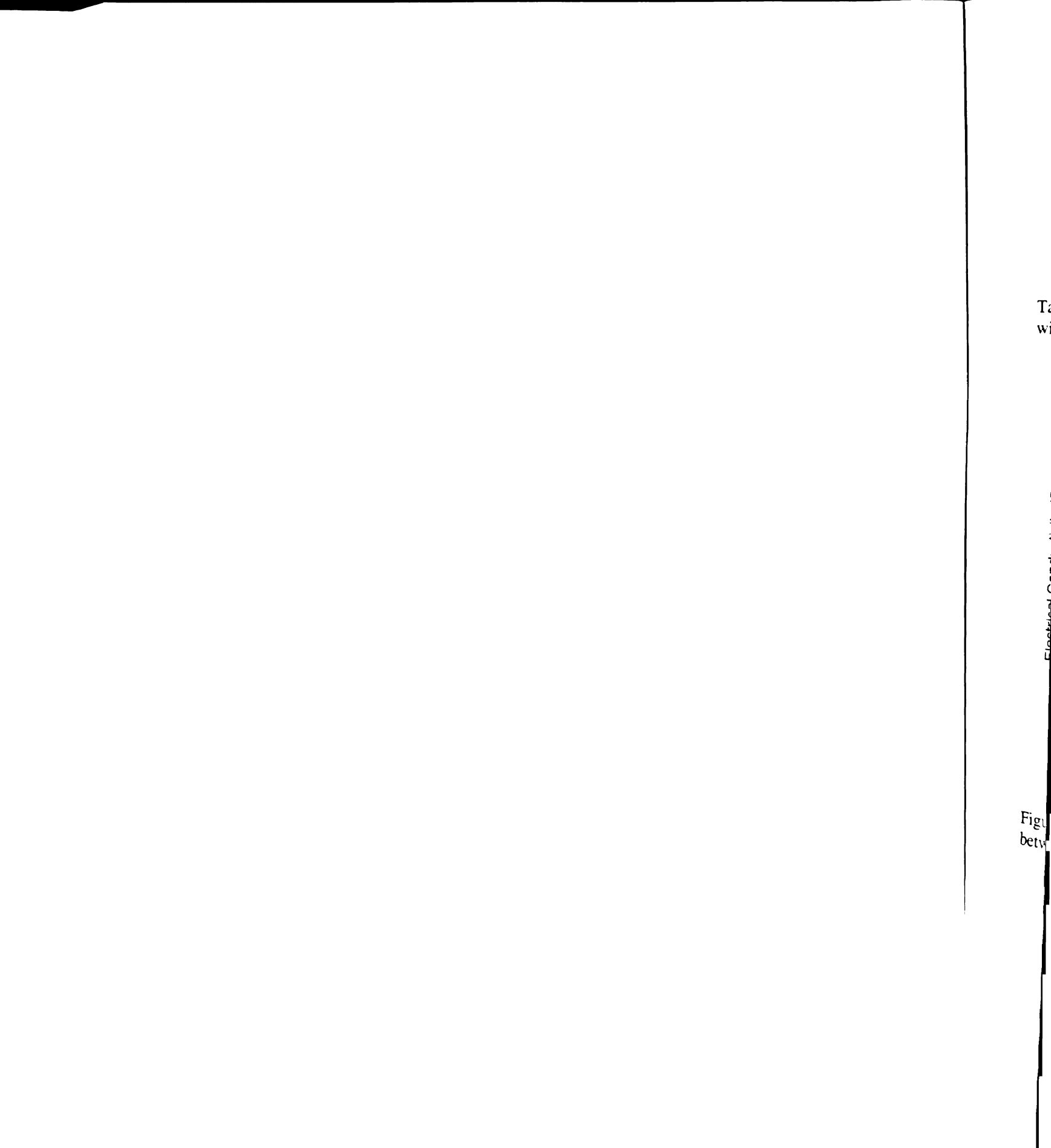

Temperature (K)	Reference resistivity (n Ω m)	Measured resistivity (n Ω m)	Error %
400	8020	8140.9	1.5%
500	10600	10708	1.02%
600	13100	13439	2.58%
700	15800	16116	2%

Table 5. 6 Error percentage calculation of the molybdenum HT resistivity measurement with the Reference.

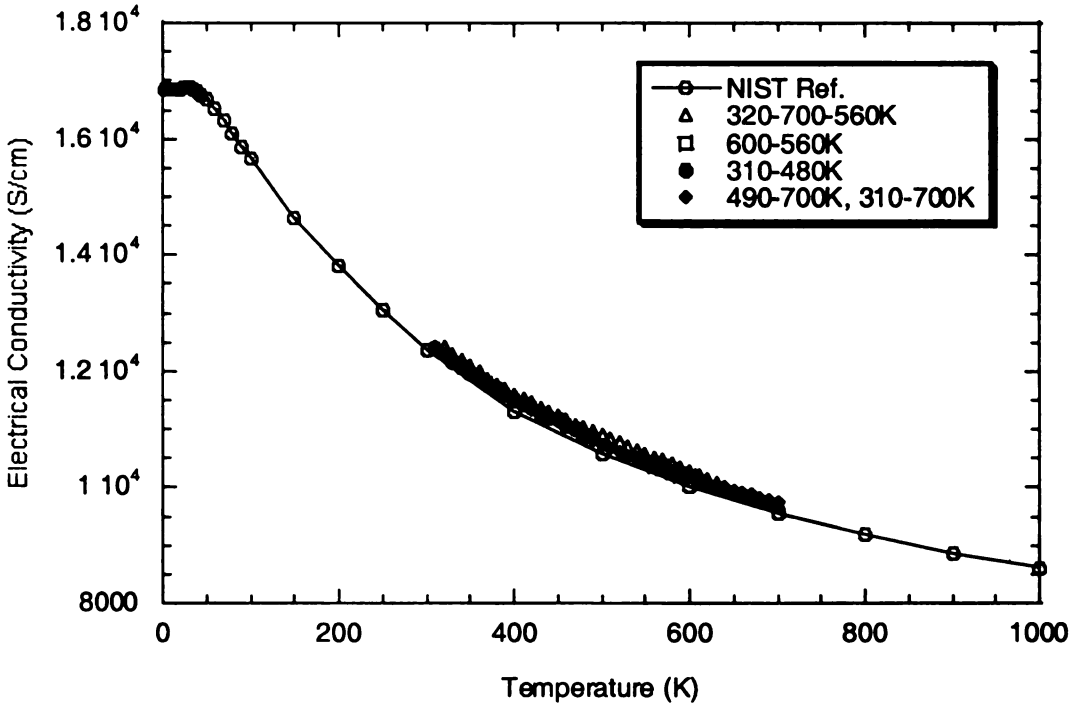

Figure 5. 15 The comparison of the electrical conductivity of NIST 1461 stainless steel between the reference (NIST [66]) and high-temperature system.

T (K)	σ (S/cm) at 400 (K)	Error %	σ (S/cm) at 700 (K)	Error %
Reference	11299	----	9569.4	----
Run1 (320-700-560K)	11611	2.76%	9721.1	1.58%
Run2 (600-560K)	----	----	----	----
Run3 (310-480K)	11516	1.92%	----	----
Run4 (490-700, 310-700K)	11535	2.08%	9753.9	1.93%

Table 5. 7 Error percentage calculation of the NIST stainless steel HT electrical conductivity measurement with the Reference.

Figure 5.15 shows the NIST 1461 Stainless steel measured in high temperature system and it agreed very well with the NIST standard data. Refer to Table 5.7 for error percentage calculation.

Figure 5.16, 5.17 and 5.18 show the measurement results of another series of cubic material, the composition is $Ag_{0.84}Pb_{18}SbTe_{20}$. The sample was grown in ingot and was cut to three different sections (See Figure 5.19). Figure 5.16 shows the electrical conductivity of the three sections. The samples have metallic behavior since the conductivities reduce as the temperature increases. Section A was measured in 4-sample system from 80-400K and it was measured in HT from 300K to 700K. The two measurement agreed very well as shown in Figure 5.16. Section B was measured in HT system before the temperature controller is properly tuned so the data points were less than the other two sections that were measured after the tuning. Figure 5.17 shows the thermopower of the three samples. The thermopower values increase linearly with temperature until around 600-700K. The power factors of the three samples are shown in Figure 5.18. The power factors of sections B and C are obtained from the curve fits of the

electrical conductivities and thermopowers plots. The EDS analysis of these samples can be found in Appendix A [67].

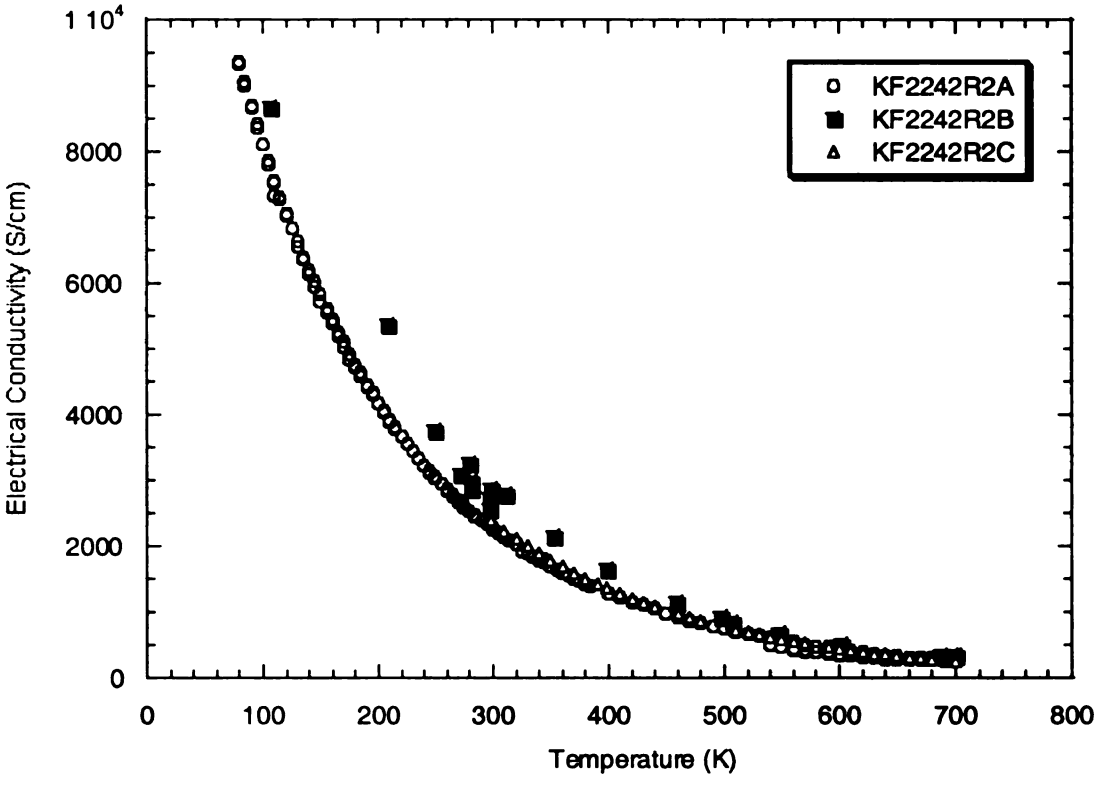

Figure 5. 16 Electrical conductivity of $Ag_{0.84}Pb_{18}SbTe_{20}$ and the sample ID is KF2242R2 with A, B and C sections.

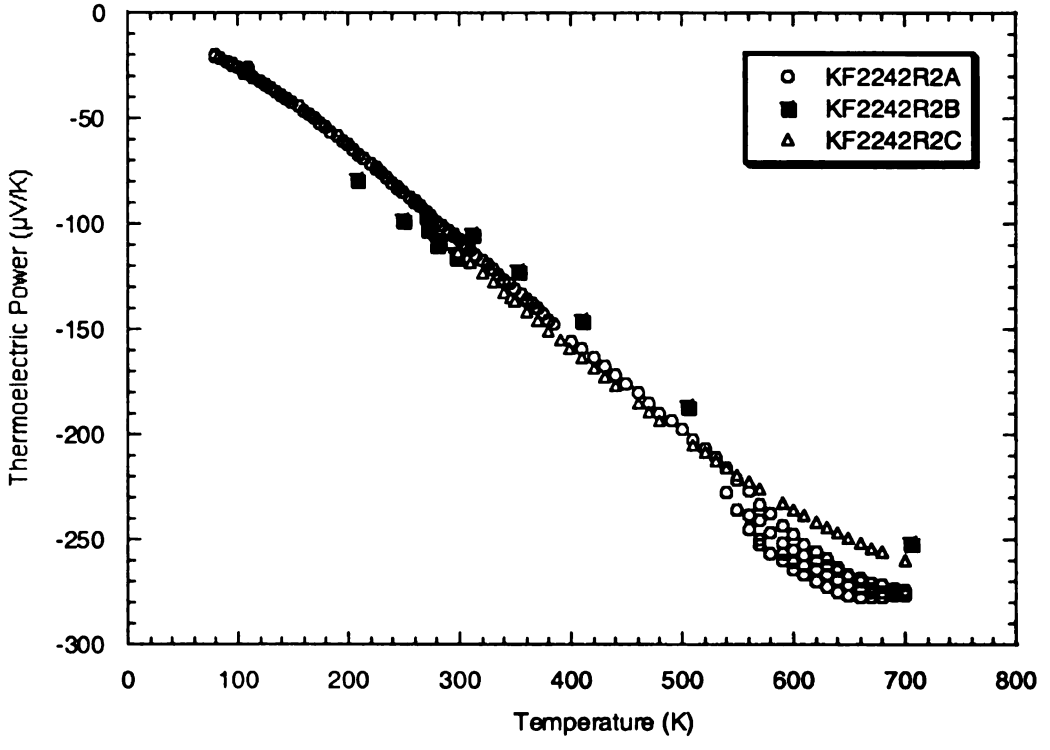

Figure 5. 17 Thermopower of $Ag_{0.84}Pb_{18}SbTe_{20}$ and the sample ID is KF2242R2 with A, B and C sections.

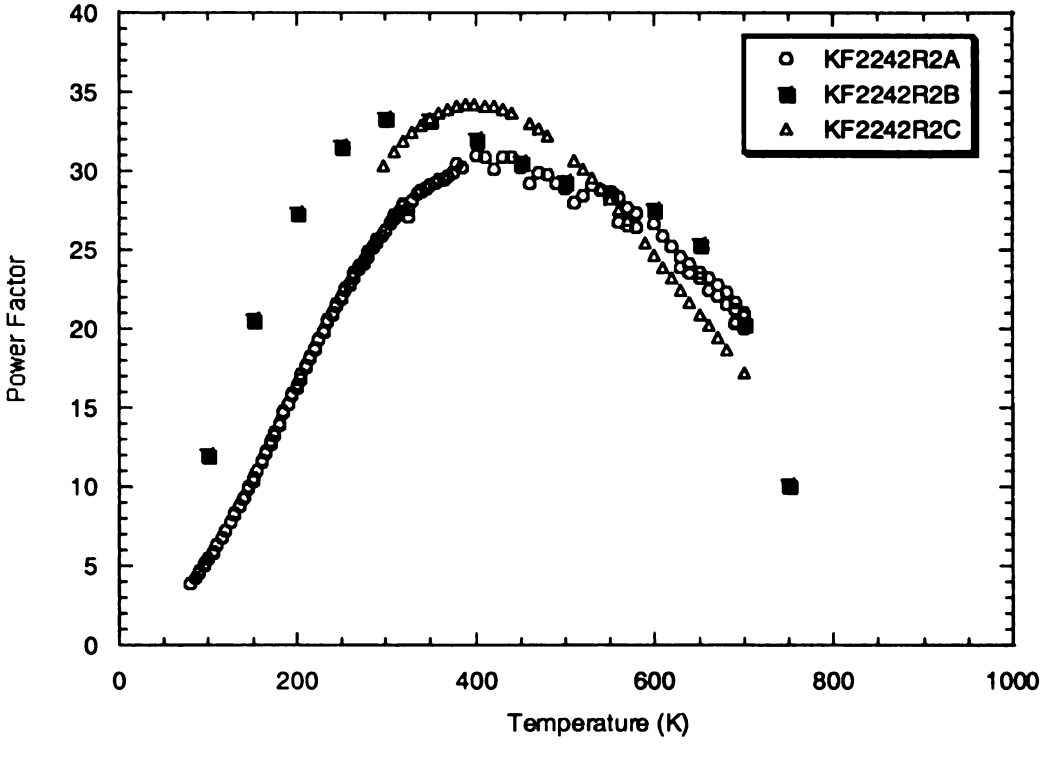

Figure 5. 18 Power factor of $Ag_{0.84}Pb_{18}SbTe_{20}$ and the sample ID is KF2242R2 with A, B and C sections.

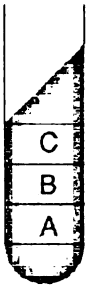

Figure 5. 19 KF series materials are grown as ingot and cut to different sections for measurement.

The high temperature system only measures the power factor of materials, as explained in the experimental set-up chapter that why high temperature thermal conductivity measurement was not considered. In order to estimate the figure of merit of a material, a theoretical calculation is included here to roughly derive the thermal conductivity of the materials based on the existing HT data and 4-sample (low-temperature) measured thermal conductivity data.

The electrical conductivity can be expressed as

$$\sigma = ne^2\langle\tau\rangle / m_e$$

and the electronic thermal conductivity is

$$\kappa_e = L\sigma T = \mathscr{L}(k^2/e^2)\sigma T$$

where $\mathscr{L} = \dfrac{\langle\tau\rangle\langle E^2\tau\rangle - \langle E\tau\rangle^2}{k^2T^2\langle\tau\rangle^2}$ and $\mathscr{L}$ is a pure number and $L = \mathscr{L}(k^2/e^2)$ is the Lorentz number. For a non-degenerate semiconductor, the relaxation time is $\tau = aE^s$ so

$$\langle\tau\rangle = a\Gamma(\tfrac{5}{2} - s)/\Gamma(\tfrac{5}{2})$$

$$\langle\tau E\rangle = akT\Gamma(\tfrac{7}{2} - s)/\Gamma(\tfrac{5}{2})$$

$$\langle \tau E^2 \rangle = ak^2T^2\Gamma(\tfrac{9}{2} - s)/\Gamma(\tfrac{5}{2})$$

Since $\Gamma(1+x)=x\Gamma(x)$, so $\mathscr{L} = \frac{5}{2} - s$, where s is the scattering parameter and for various scattering mechanisms, the s value is different. For scattering by the acoustical modes, $s = ½$ ($\mathscr{L} = 2$), and for ionized impurities scattering $s = -3/2$ ($\mathscr{L} = 4$).

For a fully degenerate semiconductor (metal), a better approximation is used to obtain the Lorentz number, please see Appendix B for more information [68]. We have

$$\langle \tau \rangle \langle E^2\tau \rangle - \langle E\tau \rangle^2 = \tfrac{1}{3}\pi^2k^2T^2\langle \tau \rangle^2$$

so $\mathscr{L} = 1/3\pi^2 = 3.289$ and $L = 2.44\text{x}10^{-8}\ \text{V}^2/\text{K}^2$. If a semiconductor which is degenerately doped but not fully degenerate, we can assume a $\mathscr{L} = 2.15$ and thus $L = 1.596\text{x}10^{-8}\ \text{V}^2/\text{K}^2$.

For the cubic materials, the latter Lorentz number is more suitable for calculating the electronic contribution of the thermal conductivity. However, since the materials are very highly doped, both Lorentz numbers are used for calculation comparisons.

Figure 5.20 shows the total thermal conductivity of sample KF2242R2A measured in 4-sample system from 80-400K. Figure 5.21 shows the calculated electronic thermal conductivity based on the measured electrical conductivity values measured from the 4-sample and HT systems. Equation is used for this calculation. Since the total thermal conductivity is known from 80-400K. We can approximate the lattice term for both L values as shown in Figure 5.22.

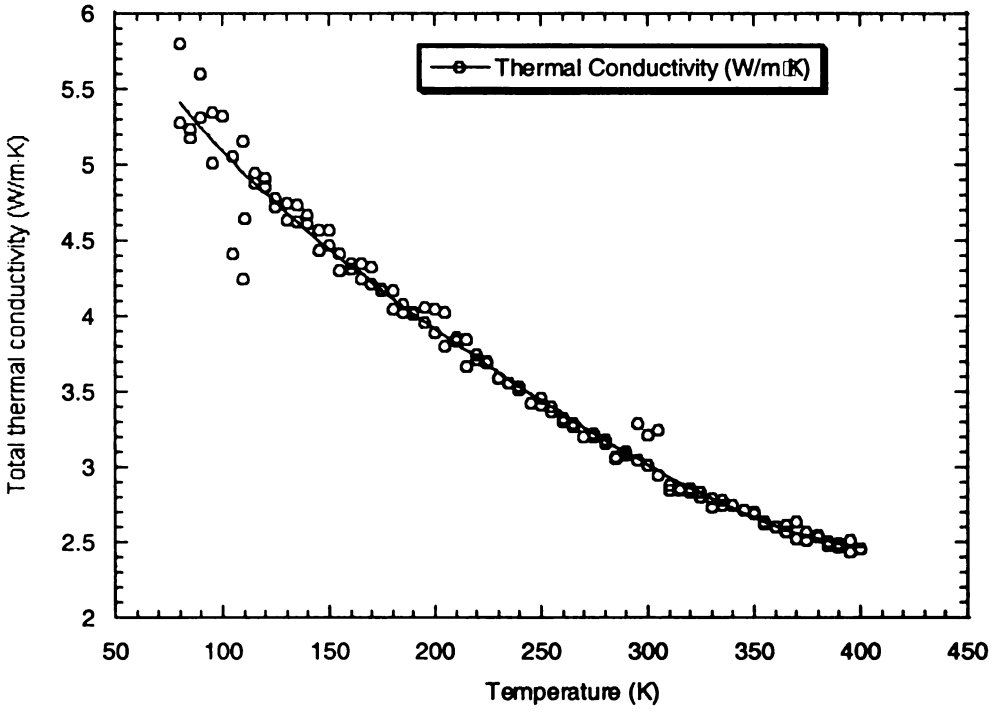

Figure 5. 20 The total thermal conductivity of KF2242R2A from the 4-sample system in Hogan's lab.

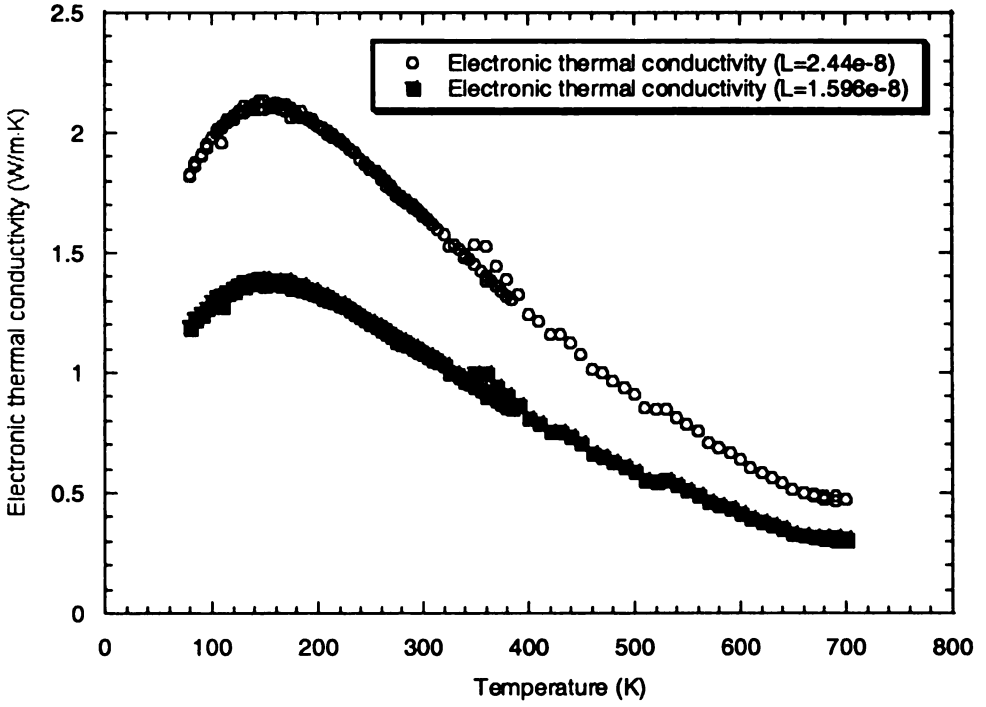

Figure 5. 21 The electronic thermal conductivity of KF2242R2A calculated from the electrical conductivity and with two different Lorentz numbers.

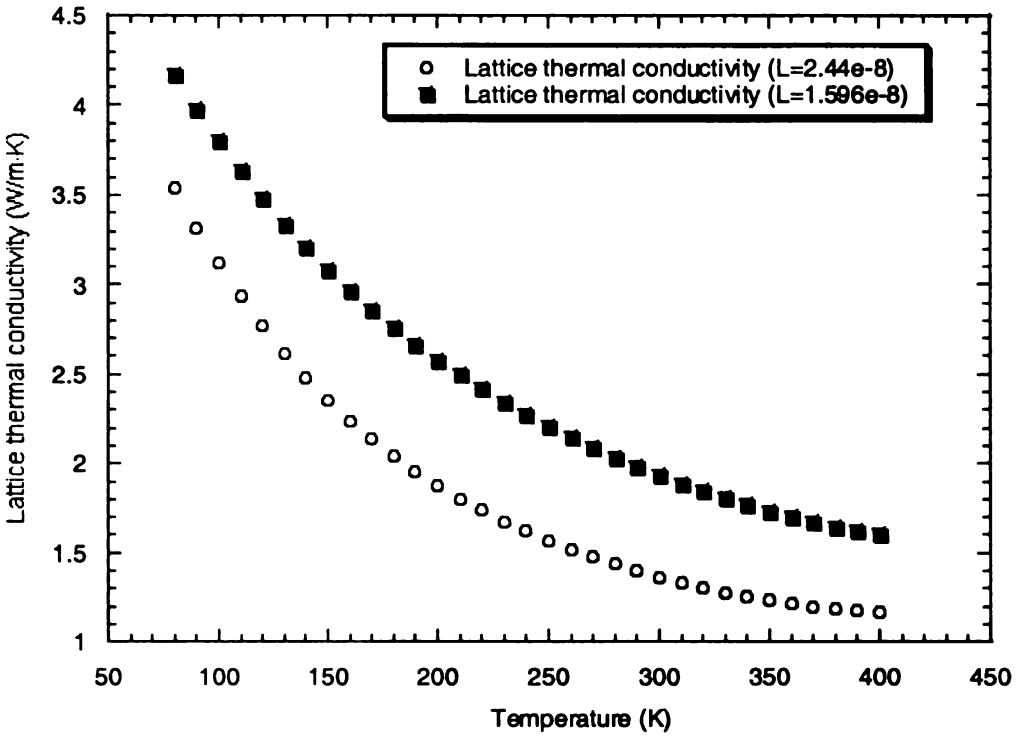

Figure 5. 22 The lattice thermal conductivity of KF2242R2A is calculated from subtractions of electronic thermal conductivity from the total thermal conductivity. These data are calculated through the equations of the sixth polynomial fit of the electronic thermal conductivity and the fourth polynomial fit of the total thermal conductivity.

The two basic scattering mechanisms in conduction are the lattice scattering and impurity scattering. Lattice scattering is when the carriers scattered by vibration of lattice. This vibration results from the temperature. Thus, as the temperature increases, lattice scattering is dominant and causes the carriers' mobility decrease. Impurity scattering, on the other hand, is dominant at low temperature. At low temperature, the thermal motion is low and the carriers have lower mobilities so they are more likely to be scattered by charged ions (impurities) than with greater momentum carriers.

In Figure 5.23, the lattice thermal conductivities are assumed to be constant at high temperatures because lattice scattering is dominant. Once the lattice thermal conductivities are predicted, the electronic thermal conductivities can be added to obtain

the total thermal conductivities as shown in Figure 5.24. Finally, the *ZT* of the material can be estimated as shown in Figure 5.25.

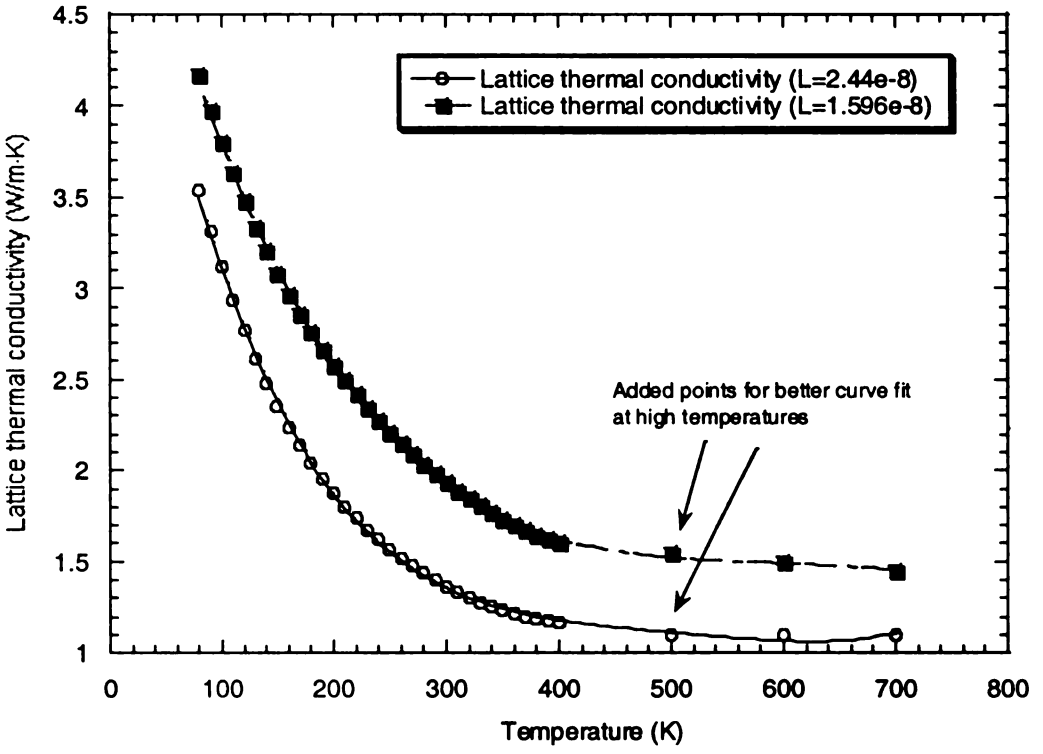

Figure 5. 23 The lattice thermal conductivity of KF2242R2A with curve fit till 700K.

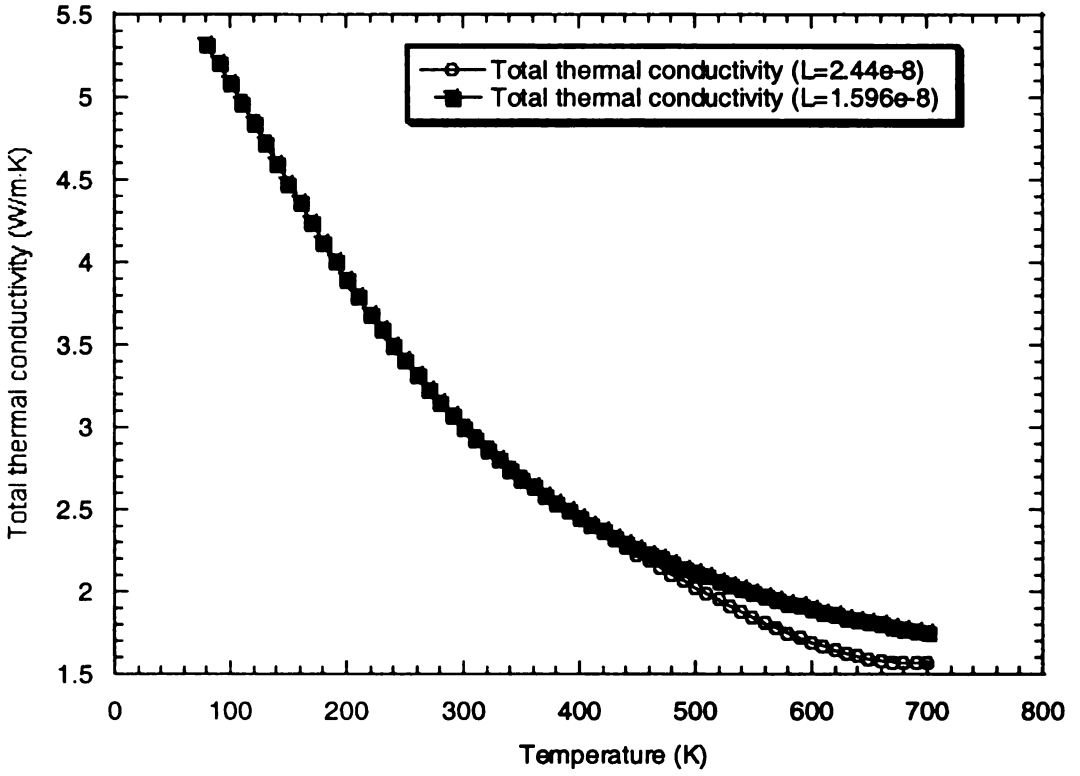

Figure 5. 24 The total thermal conductivity of KF2242R2A with two different Lorentz number.

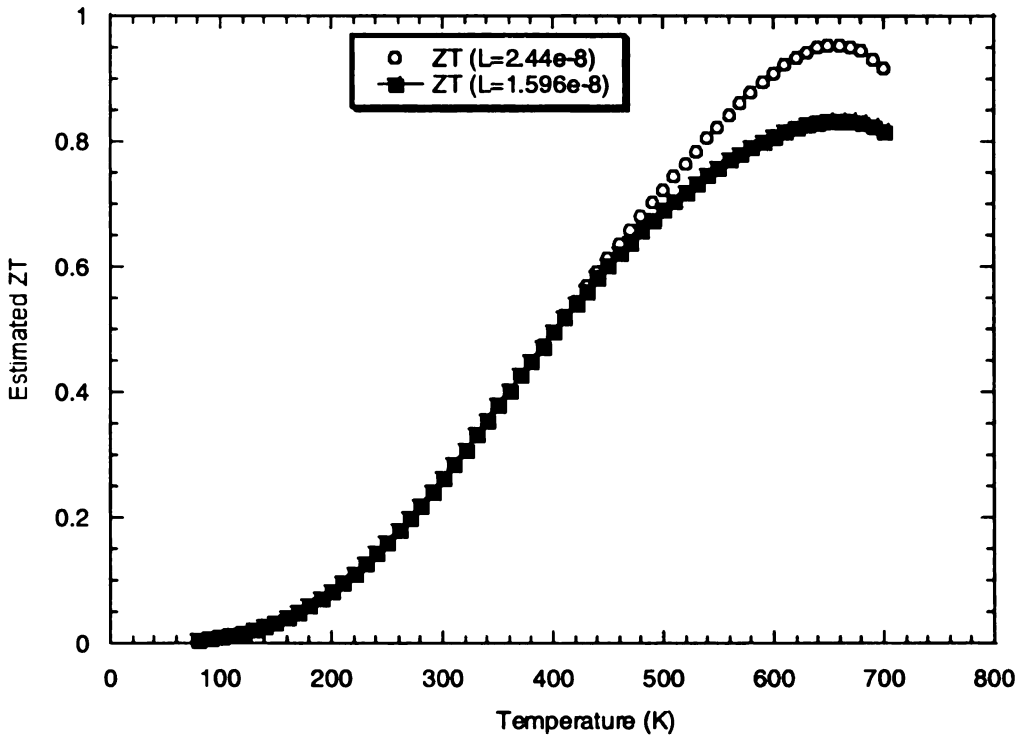

Figure 5. 25 The estimated ZT of KF2242R2A with two different Lorentz number.

In some of the latter materials, we have observed a change of electrical conductivity and thermopower as the sample is measured from 300 to 700K in a step of 10K versus measurements on the same sample from 700 to 300K. The electrical conductivity decreases as the thermopower increases as shown in Figure 5.26. Two hypotheses were made: the first hypothesis is that there might be oxide growth on the surface of the sample. Even though the sample is measured under relatively high vacuum ($5x10^{-5}$ Torr). There is still significantly large amount of particles inside the chamber. Taking the equation from Ohring [69],

Number of molecules that strike an element of surface per unit time and area is

$$\Phi = 3.513\times10^{22}\frac{P}{\sqrt{MT}} \text{ molecule/cm}^2\text{-sec}$$

where P is pressure in Torr, M is the mass of gas molecules and T is temperature in K. For our case, at 700K, vacuum is $5x10^{-5}$ Torr, the number of oxygen molecules (O_2) that strike an element of surface per unit time and area is (molecule weight for O_2 is 16 x 2 = 32g)

$$\Phi = 3.513\times10^{22}\times\frac{5\times10^{-5}}{\sqrt{32\times700}}$$

$$= 1.17\ x10^{16} \text{ oxygen molecules/ cm}^2\text{-sec}$$

The second hypothesis is that microcracks might appear inside the materials. This is a whole new area of research to investigate the material science of cubic materials.

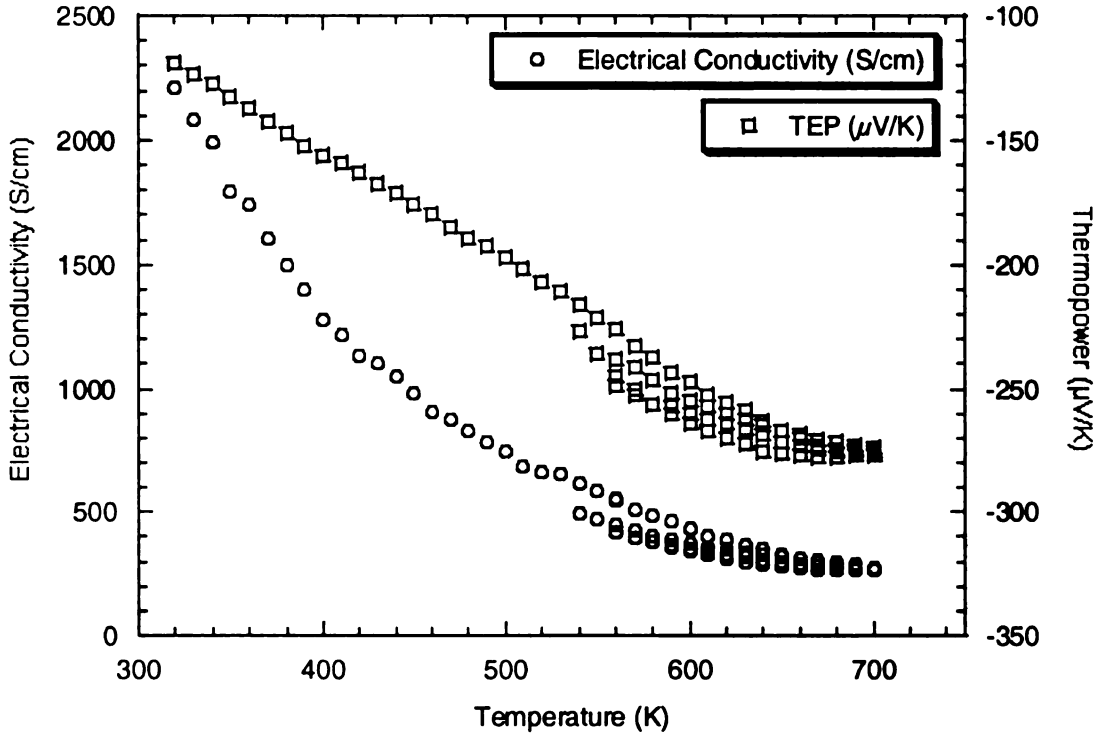

Figure 5. 26 The electrical conductivity and thermopower of KF2242R2A.

A sample with more silver composition KF2242R3C, $Ag_{0.86}Pb_{18}SbTe_{20}$, was measured with the electrical conductivity and thermopower shown in Figures 5.27 and 5.28. The sample has been measured repeatedly as to show consistency. The electrical conductivity data repeated very well. The magnitude of the thermopower values decreases a bit after one cycle but it remained same values after that. After the measurement, the sample was observed under the microscope. Figure 5.29 shows a layer of thin film is formed on the surface of the material. Figure 5.30 shows crack lines appear on the surface of the sample, this might explain the deviation in thermopower data. Since the electrical conductivity measurement did not change, it is believed that the cracks have affected the sample thermal conduction only. It is suspected that the cracks on the sample are due to the difference in thermal expansion between the sample itself and the sample

stage. The thermal expansion coefficient of a sample with similar composition was measured using TMA (Thermomechanical Analyzer) and it gives about 21.4 μm/(m °C) [70]. It is compares with the thermal expansion coefficient of copper at 16 μm/(m °C).

In addition to the thermal expansion problem, some evidence also suggests that elements might have evaporated from the sample. As shown in Figure 5.31, after the high temperature run with the sample KF2242R3C, the copper plate used to mount the sensor had a grayish coating on the surface. Only one face of the copper plate changed color, this indicates a coating on the plate, as opposed to an alloying. EDS analysis shows that the surface of the copper plate was coated with tellurium [71] and this is one of the main components of the sample. However, this was not observed before so not all cubic materials will evaporate elements.

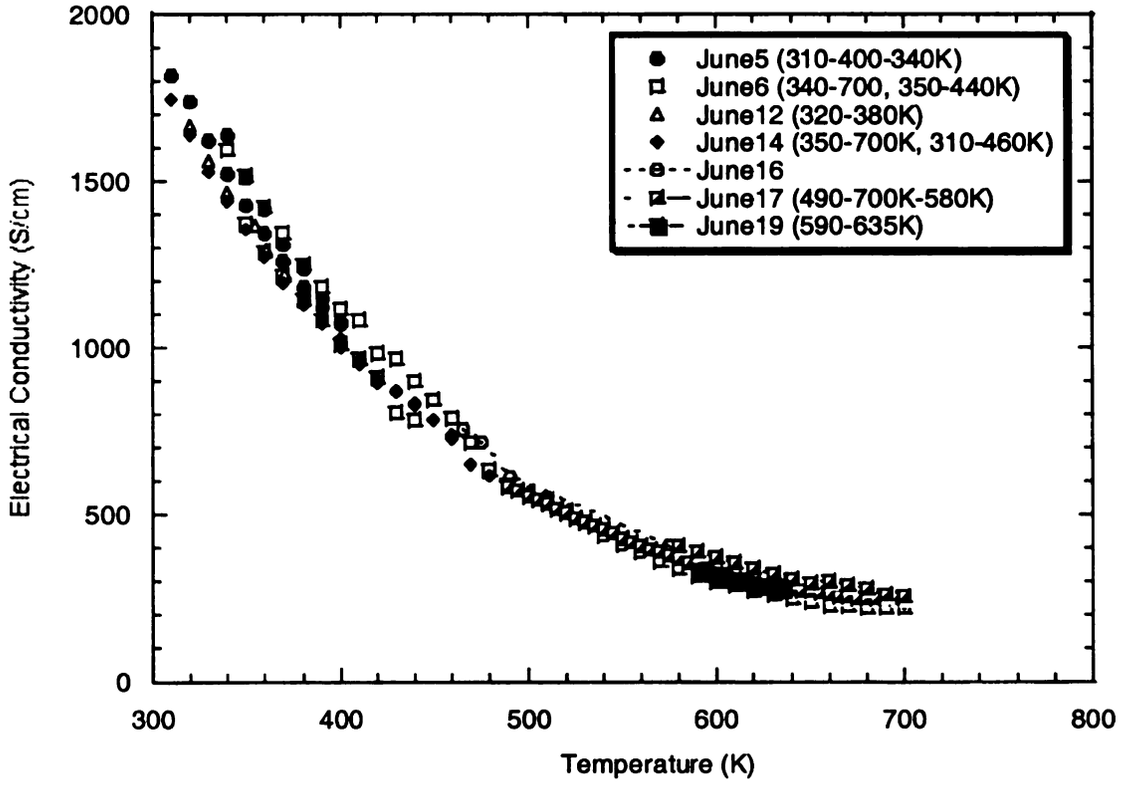

Figure 5. 27 The electrical conductivity of sample KF2242R3C $Ag_{0.86}Pb_{18}SbTe_{20}$ with repeated runs.

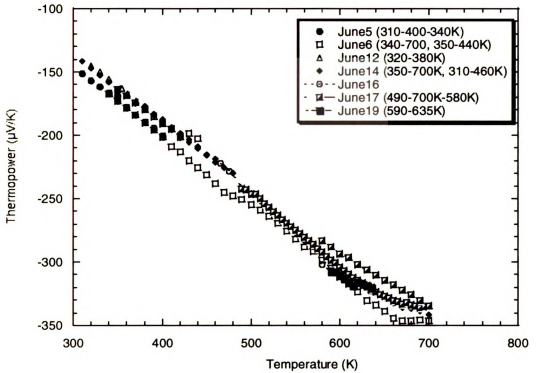

Figure 5. 28 The thermopower of sample KF2242R3C $Ag_{0.86}Pb_{18}SbTe_{20}$ with repeated runs.

Figure 5. 29 A layer of thin film formed on the surface of sample KF2242R3C $Ag_{0.86}Pb_{18}SbTe_{20}$ after running in high temperature.

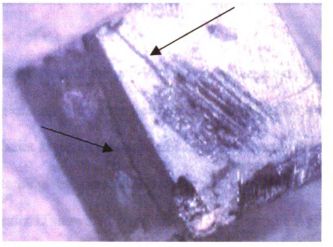

Figure 5. 30 Crack lines occurred on the surface of sample KF2242R3C $Ag_{0.86}Pb_{18}SbTe_{20}$ after running in high temperature.

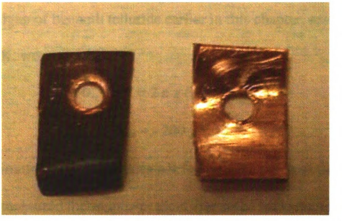

Figure 5. 31 The copper plate coated with tellurium (left) and a clean copper plate (right).

Figure 5.31, 5.32, and 5.33 show the thermopower, electrical conductivity, and the power factor of cubic materials with various composition of silver. This allows us to determine the best properties of the cubic materials among various composition of silver. For this series of cubic materials, the sample that contains the most silver has the best properties (the highest power factor). Some of the samples labeled "fit" indicates those power factor plots were generated from curve fits of the thermopower and electrical conductivity measurements. This was done because some of the measurements were

taken before the system was properly tuned and having fewer data points made it difficult to determine the trends of the power factor.

In Figure 5.32 or some of the previous thermopower plots, the thermopower values of some samples stayed constant between 660-700K. At first, it appears to be a turning point but it is not as defined as expected. Further investigation on the energy band gap of the cubic material gives some information on how to interpolate the shape of the thermopower. Appendix D shows the bandgap of a cubic sample $AgPb_{18}SbTe_{20}$ to be 0.26 eV at room temperature (300K). If we assume a constant energy bandgap from room temperature to high temperatures and use the same calculation that was performed to estimate the bandgap of bismuth telluride earlier in this chapter, assuming the turning point occurs at 650K, we get,

$$0.26\ eV = 2\ e \times 650 \times S_{max}$$

$$S_{max} \sim -200\ \mu V/K$$

The estimated maximum thermpower does not fall into the range of the measured thermopower. The measured thermopower plots suggested maximum thermopower should be larger than -250μV/K. If we assume a higher T_{max} = 700K or 800K, the S_{max} value will be even lower.

If we take another approach, taking the sample $Ag_{0.86}Pb_{18}SbTe_{20}$ as example, if the turning point really occurs and the estimated bandgap will be

$$E_g = 2\ e \times 680 \times 350$$

$$E_g \sim 0.476\ eV$$

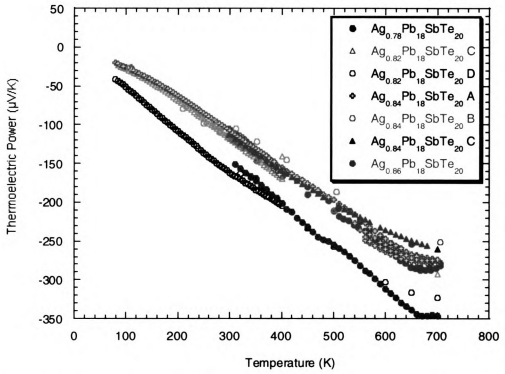

Figure 5. 32 The Thermopower of cubic materials with various composition of silver.

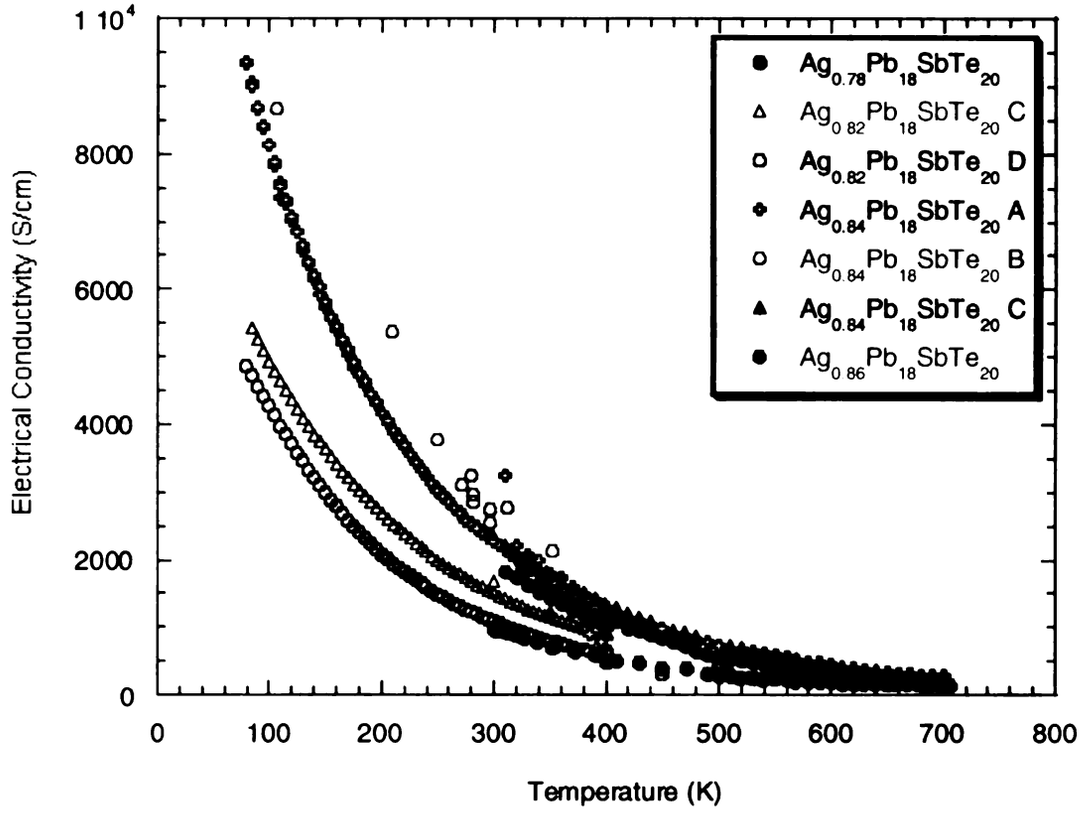

Figure 5. 33 The electrical conductivity of cubic materials with various composition of silver.

If this is true, it suggests that this sample exhibits increasing bandgap with increasing temperatures. This property can be found in PbTe and since cubic materials are mainly PbTe derivation. Further investigation on the change of bandgap vs. temperatures will be helpful.

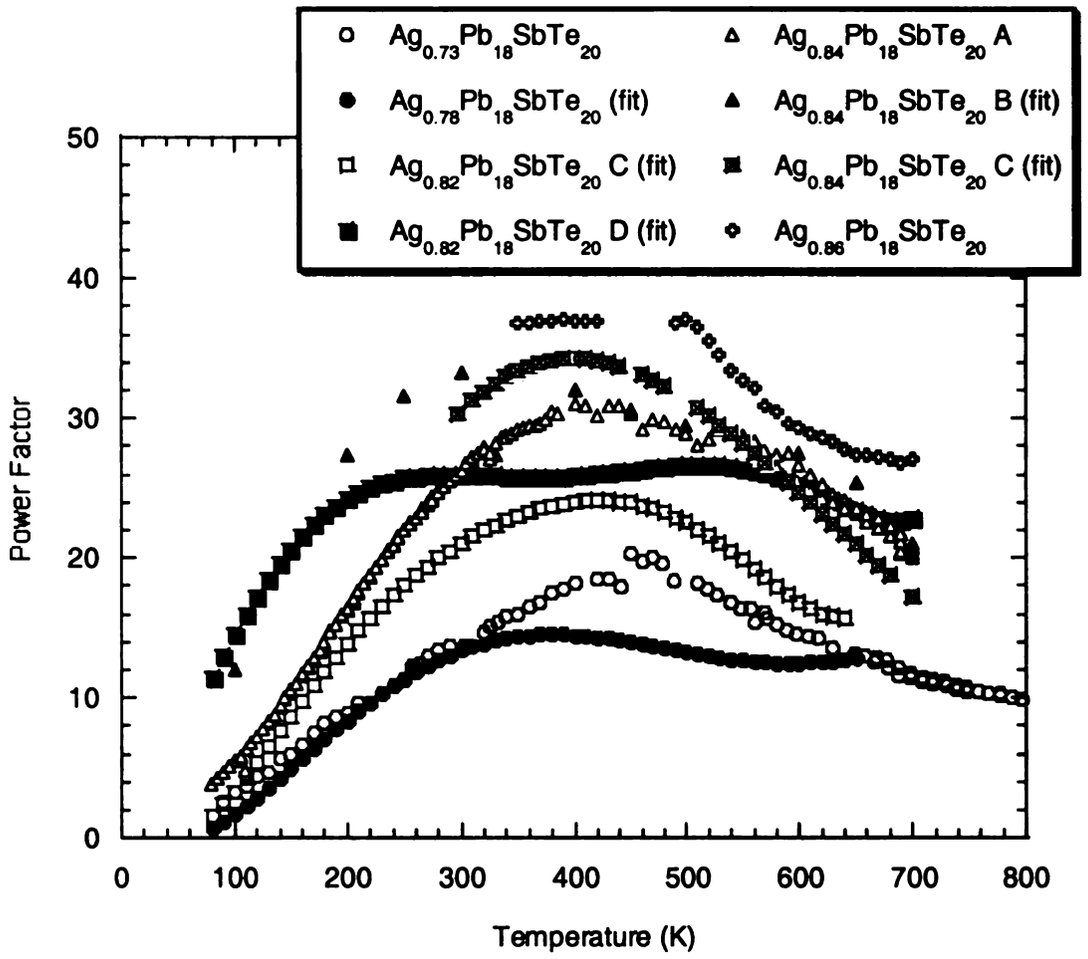

Figure 5. 34 The power factor of cubic materials with various composition of silver.

Chapter 6 Simulation and Experimental Results of the Module

Theoretical simulations of the device's performance can be obtained by utilizing the results from the 4-sample and high-temperature measurement systems. TE modules for low temperature applications, i.e. for cooling purpose, have been investigated [72] and models for the high temperature modules are being developed.

Before building a TE module, some performance simulations are needed to estimate the best pairing of *p*- and *n*-type legs for the device. MathCAD® simulation was used to determine the module's ZT, TE efficiency, and maximum power output of a TE module. Most of the important parameters for the simulations can be obtained from the transport measurements of each material individually.

The performance of a TE power generator depends on the hot side temperature, T_h, the temperature difference between the hot and cold ends, ΔT, and the Figure of merit of the materials, ZT. The efficiency of a single-couple TE generator without contact resistance is given by

$$\eta_t = \frac{W_e}{Q_h} \qquad \text{or}$$

$$\eta_t = \frac{\mu\eta_c}{\left[(\mu+1)^2 / ZT_H + (\mu+1) - \eta_c/2\right]}$$

A TE module made up of an *n*-type cubic material, $Ag_{0.82}Pb_{18}SbTe_{20}$, and a *p*-type cubic material, $Ag_{0.9}SnSb_{1.1}Te_3$, was fabricated. Both samples have similar thermoelectric efficiency. The *n*-type cubic materials have been heavily investigated as discussed in Chapter 5. The optimized material was not used to fabricate the module because optimized *p*-type material has not yet been discovered. Therefore, the *n*-type sample that

was used in building the module was selected to match the ZT of the *p*-type samples that we have. The following sections compare experimental and simulated results.

6.1 Simulations

MathCAD® software was used to simulate the TE modules performance. The code and results from these calculations can be found in Appendix E.

Since these two materials have been characterized by measurements from the low and high temperature systems, the thermoelectric properties are taken directly from experimental results. These properties are then used in simulation to determine the performance of the TE module, and finally compared to experimental results. A list of important parameters used in the simulation of the TE module are given below:

$S_p(T)$: Temperature dependent thermopower of p-type material (μV/K)
$S_n(T)$: Temperature dependent thermopower of n-type material
$S_M(T)$: Temperature dependent thermopower of the TE module

$\rho_p(T)$: Temperature dependent resistivity of p-type material (Ω cm)
$\rho_n(T)$: Temperature dependent resistivity of n-type material
$R_{int}(T)$: Temperature dependent internal resistance of TE module (Ω)
R_{cont}: Contact resistance of TE module
$R_M(T)$: Total TE module resistance
$R_L(T)$: Load resistance

$\kappa_p(T)$: Temperature dependent thermal conductivity of p-type material (W/m K)
$\kappa_n(T)$: Temperature dependent thermal conductivity of n-type material
$K_M(T)$: Temperature dependent thermal conductance of TE module

I_L: Load current (A)
$V_{oc}(T)$: Open circuit voltage (V)

A_p and A_n are the surface area of p and n-type materials respectively (m^2)
L_p and L_n are the length of p and n-type materials respectively (m)

η_c: Carnot efficiency (%)
η: TE module efficiency or conversion efficiency

W_e: Electrical output power (W)
Q_h: Thermal power input (W)

ΔT: Temperature gradient
T_h and T_c are the hot side and cold side temperatures respectively
T_M: The mean temperature

Important Equations: (these are the general equations, unit conversion is not included)

$$\Delta T = T_h - T_c$$

$$T_M = \frac{T_h + T_c}{2}$$

$$S_M(T) = |S_p(T)| + |S_n(T)|$$

$$R_{\text{int}}(T) = \left(\frac{\rho_n(T)}{A_n} + \frac{\rho_p(T)}{A_p} \right) * L_p$$

$$R_M(T) = R_{\text{int}}(T) + R_{cont}$$

$$K_M(T) = \left(\kappa_n(T) * A_n + \kappa_p(T) * A_p \right) * L_p$$

$$\eta_c = \frac{\Delta T}{T_h} \qquad W_e = I_L^2 R_L$$

$$\eta = \frac{W_e}{Q_h}$$

$$Q_h = S_M(T) * I_L * \Delta T + K_M(T) * \Delta T - \frac{I^2 * R_M(T)}{2}$$

Assume a constant temperature gradient, constant module contact resistance of 3 mΩ. Table 6.1 shows the performance parameters obtained from the simulation. A conversion efficiency of 3.6% is obtained for a fixed temperature gradient of 200K, T_h=500K and T_c=300K. Figure 6.1 shows the simulated ZT of the module vs. temperatures. The ZT is 0.5 at 500K. The simulation was done only till 500K because the module is suppose to operate less than 550K since the p-type sample will melt above this temperature. Figure 6.2 shows the heat flow through the module with temperature gradient of 100K and 200K vs. current output. It verifies that higher temperature gradient will give larger heat flow.

Performance Parameters	Simulation Results
Open circuit voltage, V_{oc} (V)	0.064
Load current, I_L (A)	2.148
Load voltage, V_L (V)	0.028
Total internal resistance, R_{int} (Ω)	0.017
Electrical output power, W_e (W)	0.06
Conversion efficiency, η (%)	3.6
Input thermal power, Q_h (W)	1.662

Table 6. 1 The performance parameters obtained from simulation.

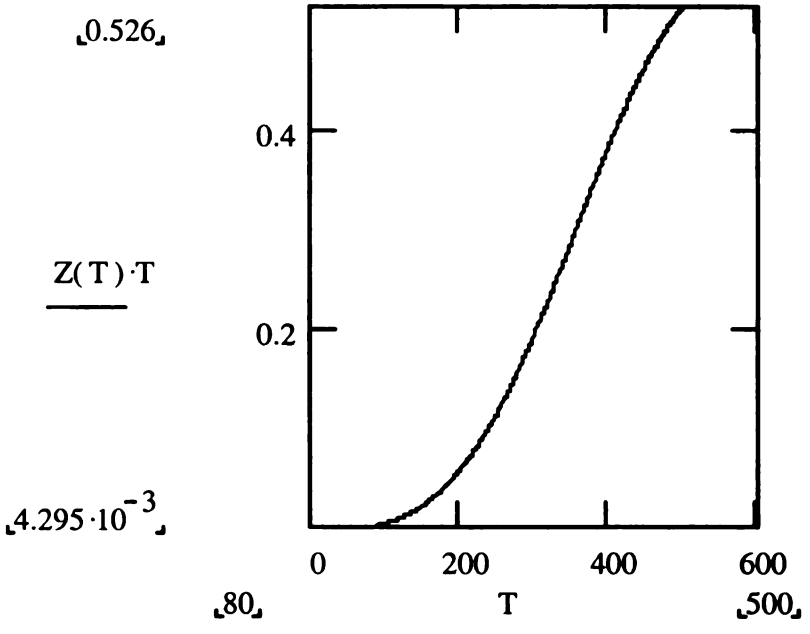

Figure 6. 1 Simulated ZT of the module vs. temperature.

Figure 6.3 shows that the efficiency also increases as the temperature gradient increases. Figure 6.4 and 6.5 show the power output of the module vs. efficiency and temperature gradient.

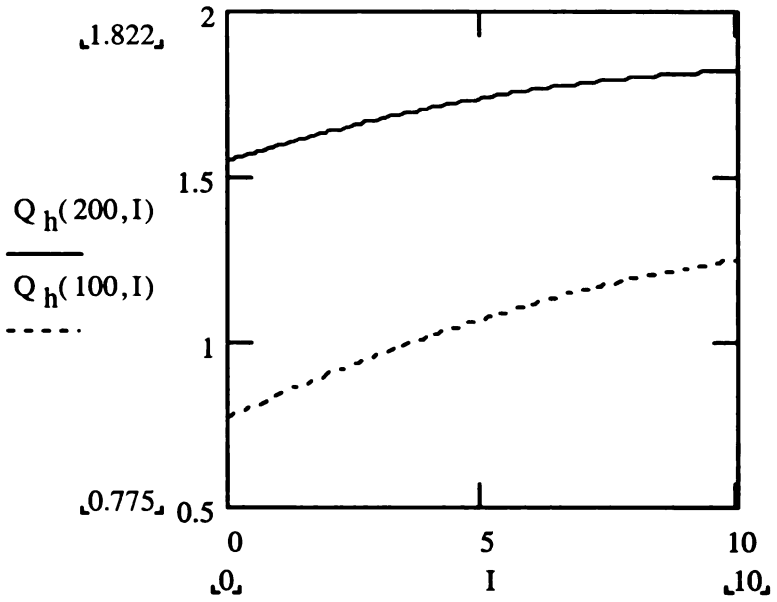

Figure 6. 2 Heat flow through the module vs. current output.

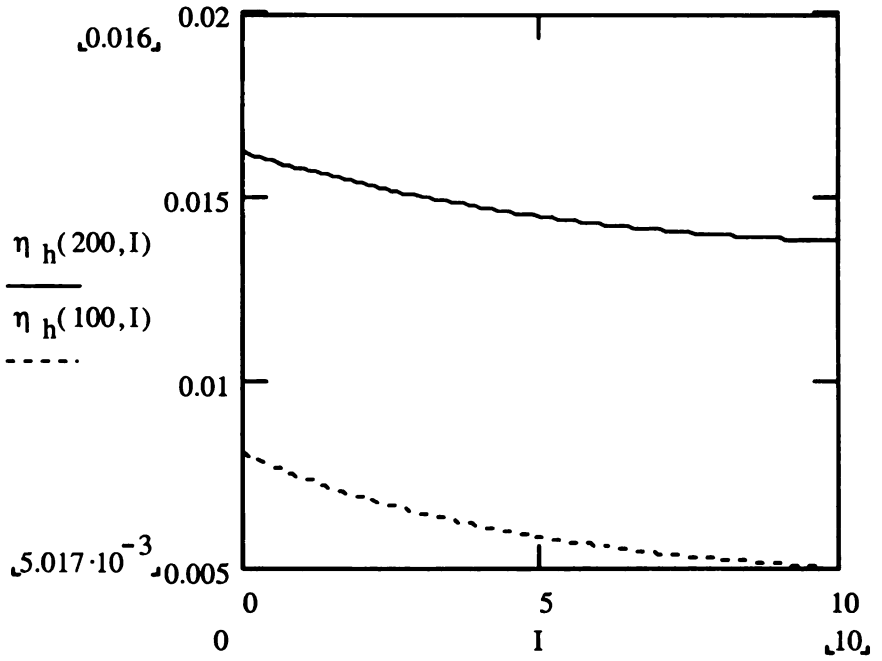

Figure 6. 3 Efficiency of the module vs. Current Output.

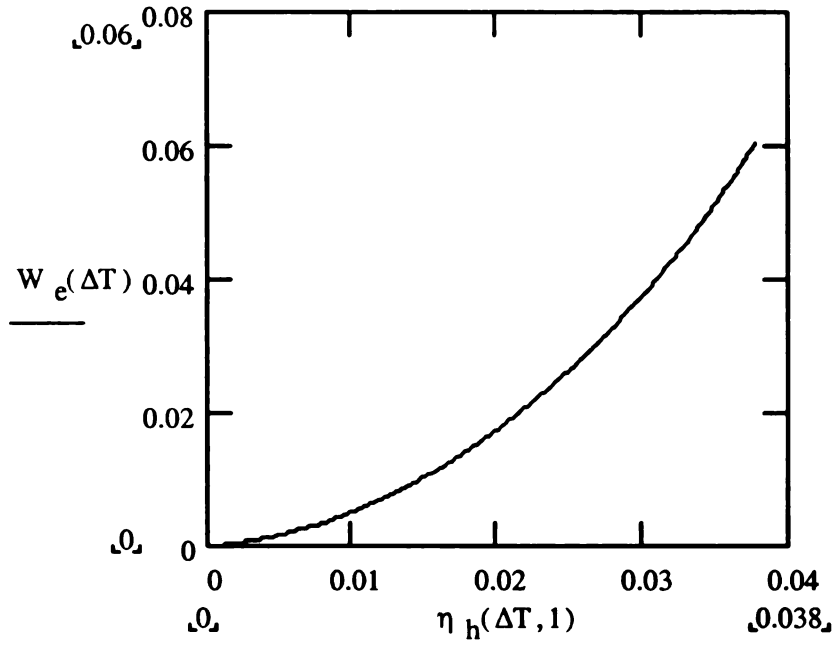

Figure 6. 4 Power output of the module vs. efficiency.

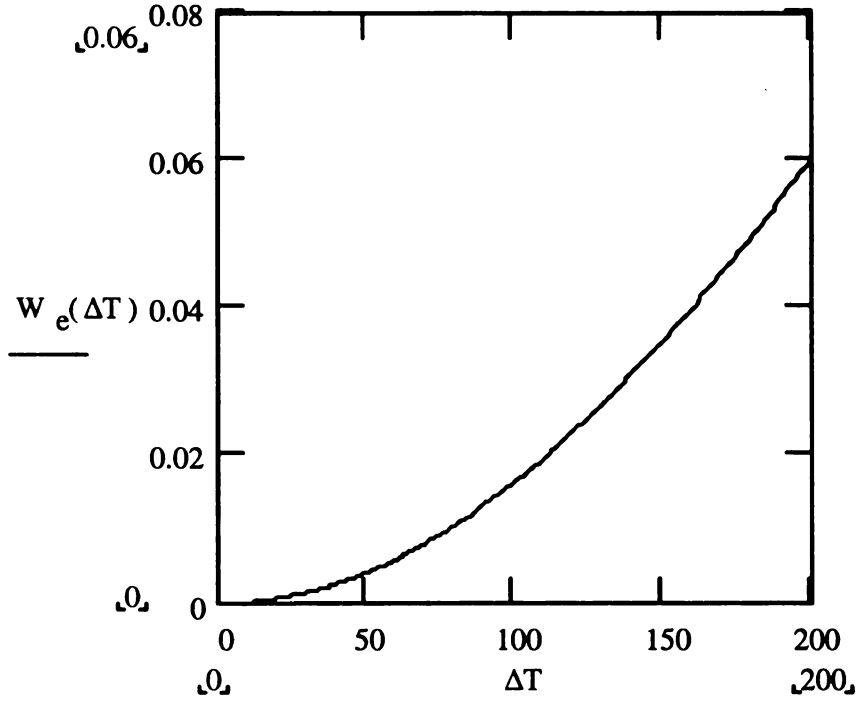

Figure 6. 5 Power output of the module vs. temperature gradient.

6.2 Module Testing

Figure 6.6 shows the TE module made of an *n*-type cubic material, $Ag_{0.82}Pb_{18}SbTe_{20}$, and a *p*-type cubic material, $Ag_{0.9}SnSb_{1.1}Te_3$. The *p* and *n*-type samples are sandwiched between two alumina plates with nickel traces. The samples are soldered to the bottom plate with a standard tin-lead solder. If the sample does not bond with solder easily it is helpful to nickel plate the ends of the sample allowing the solder to bond. The samples are bonded to the top plate with platinum paste since the top plate is exposed to high temperatures where standard tin-lead solder would melt. The total resistance including the contact resistance of the module was tested to be about 0.1 Ω by a handheld multimeter. Unfortunately, the *p*-type sample was broken laterally during the process of mounting the module onto the cryostat. Although the platinum paste gives very good electrical contact, the paste becomes flaky after it is dried and the mechanical bonding is weakened. It was clear from this experience, that the solder bond was stronger than the bond of the platinum paste, as one might expect. After this, one of the broken pieces of the *p*-type sample was reoriented (to match the length of the *n*-type leg) and used as the *p*-type leg of the module and the samples were connected to the top plate using silver paste. The total module resistance then became approximately 0.2 Ω indicating an increase in contact resistance. During the re-assembly of this module, the same sample preparation (polishing and nickel plating) was followed as in the first assembly.

The thermal conductance measurement technique, which is described in Section 2.5.2.1, was used to characterize the module, in the same HT system. The module was mounted on the sample stage with silver paste and the system was maintained in a

vacuum environment of 10^{-5} Torr with the temperature of the sample stage held constant at 300K. Two single-ended Chromel-Constantan thermocouples were used to monitor the temperature gradient across the module. A platinum RTD was used as a heater and mounted on top of the module to establish the desired temperature gradient. The pulse technique was used to obtain the temperature gradient. Two voltage leads were added to the RTD heater to measure the power applied to the heater. The temperature of the sample stage was maintained at 300K with some flow of liquid nitrogen through the cryostat. The PID temperature control was easily tuned to maintain a constant temperature.

First, the thermal conductance of the open-circuit module was measured with various source currents (or temperature gradients). Then the thermal conductance of the short-circuit module was measured. Each of the bottom nickel traces was soldered to a thick copper wire (1 mm diameter) and these wires were connected to one of the pins in the connector A (which was not used before). In open-circuit condition, just leaving the two pins unconnected. In short-circuit condition, simply shorted these two pins from outside. Figure 6.7 show the capture image displayed the temperature gradient across the sample vs. time. Table 6.2 and 6.3 show the results of the open and short circuit tests.

Thermal conductance is $K = \frac{Q}{\Delta T}$, where Q is the power supplied to the heater.

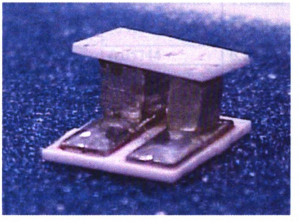

Figure 6. 6 Single couple TE module with n-type cubic material, $Ag_{0.82}Pb_{18}SbTe_{20}$, and a p-type cubic material, $Ag_{0.9}SnSb_{1.1}Te_3$.

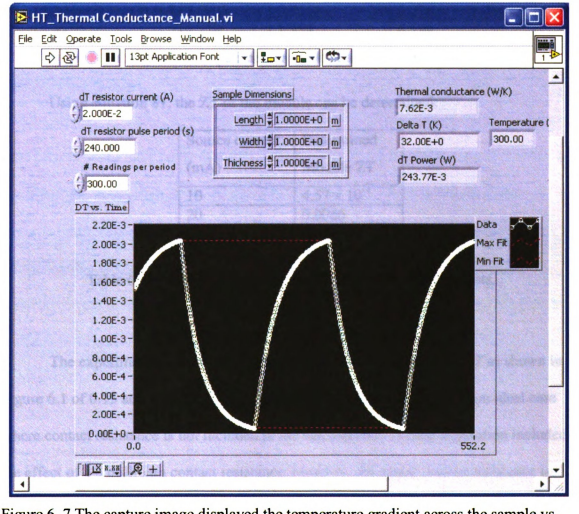

Figure 6. 7 The capture image displayed the temperature gradient across the sample vs. time.

Source current (mA)	Temperature Gradient (K)	Power Supplied to Heater (W)	Thermal Conductance (W/K)
10	9.38	0.05744	6.1237
20	42.199	0.2573	6.097
30	118.71	0.71726	6.042
37	220.7	1.3625	6.174

Table 6. 2 The experimental result of the open circuit test.

Source current (mA)	Temperature Gradient (K)	Power Supplied to Heater (W)	Thermal Conductance (W/K)
10	9.36	0.057344	6.1265
20	41.8843	0.25705	6.1372
30	117.6757	0.7164	6.088
37	219.238	1.359	6.199

Table 6. 3 The experimental result of the short circuit test.

Using equation 81, the ZT of the module can be determined:

Source current (mA)	Determined Module ZT
10	4.57×10^{-4}
20	0.0066
30	0.00761
37	0.004

Table 6. 4 The determined *ZT* of the module from the two tests.

The experimental results for *ZT* do not agree with the simulated *ZT* as shown in Figure 6.1 of 0.15 at 300K. This is because the simulation value is based on ideal case where contact resistance is not included in the calculations. A later simulation included the effect of a 3 milliohm contact resistance; however, the actual contact resistance is much higher than this value. Since the module is characterized through an open and short circuit method, the accuracy of this experiment was suspected to be affected by the non-

ideal short circuit measurement. In addition, the simulated ZT is calculated at an average temperature, however the actual module operates over a temperature gradient. Improvement of the contact resistance to these new materials is an area of study presently being investigated along with variable load measurements on these modules.

Chapter 7 Conclusion/Future Work

A high temperature thermoelectric transport measurement system has been successfully built and new quaternary cubic materials have been characterized. Various reference materials, including bismuth telluride, Constantan, molybdenum, and NIST 1461 stainless steel have been measured in the HT system to verify the accuracy of the system. Since some variation is expected between the reference samples that were measured and the reference samples that were shown in the literature, the error percentage calculation is subjective to each material. Overall measurements show a very low error percentage of < 3% in electrical conductivity measurement. A slightly higher error percentage of 5-8% (for Constantan) and 6-18% (for Molybdenum) are observed for thermopower measurements.

On some samples, it was observed that after the HT measurement a thin grayish film formed on the surface of material. In some measurements of the new cubic materials, the repeatability between runs was also a challenge and it was suspected that these samples underwent elemental redistribution and/or evaporation of elements from the material at the high temperatures used in the measurement. The evidence of this hypothesis came from the SEM/EDS analysis, collected on samples before and after the temperature dependent measurements, which indicated a change in the surface composition. Further EDS analysis on copper taps placed near the samples showed films deposited on the copper tabs included a tellurium component (one of the constituent elements of the new materials). In some of the cases, when changes in electrical conductivity and thermopower were observed between runs, the power factor remained the same. This suggests that the redistribution of elements near the surface of the

materials has not significantly changed the thermoelectric efficiencies of these samples. Cracks were also observed after the HT measurement in some cubic materials. The coefficient of thermal expansion (CTE) between the sample (21μm/m K) and the copper (16μm/m K) stage is significant, however, for a reference sample of molybdenum (6μm/m K) the measurement did not experience difficulties. Further investigations on the cause of such cracking are needed to better understand these materials.

The results of the investigations show that the higher the silver composition of the compounds $Ag_xPb_{18}SbTe_{20}$ with x = 0.78, 0.82, 0.84 and 0.86, the higher the power factor. Some of thermopower values of these cubic materials have reached saturation at around 650-700K, these phenomena was suspected to be associated with the characteristic of increasing bandgap with increasing temperature. Goldsmid's S_{max} T_{max} estimates were used to calculate the bandgap of this material based on the thermopower measurement. The estimates were not accurate and this suggests that Goldsmid's method cannot be applied to all materials.

Experimental results have helped to further understand these novel materials and to determine the doping trends in order to achieve property optimization. In general, these new cubic materials are all *n*-type semiconductors with metallic electrical conductivity behavior indicating these are degenerately doped semiconductors. Some of the power factors reach > 30μW/K^2 cm in a large temperature range of 300-600K.

A prototype TE module based on these new materials has been presented along with performance measurements of the overall module. Both *p* and *n*-type cubic samples are used to construct the module. Since the properties of the *p*-type cubic materials are not optimized, an *n*-type cubic sample was selected to match the ZT of the *p*-type sample.

Both of these samples have a maximum ZT of 0.5 at 500K. The module was fabricated and later tested using the open and shorted circuit technique. The measured ZT of the module did not match with the estimation. The main difficulty in the module fabrication is in obtaining low contact resistances. In addition, the simulated ZT was based on the ideal case where ZT was estimated at the average module temperature but the actual module was operated with a temperature gradient rather than a fixed temperature. More investigation of various materials for making low resistance electrical and thermal contacts to these materials, as well as further investigations of material preparation are recommended for future studies.

Some of the suggestions for further improvement on this HT system include different sample mounting configuration, different design of cryostat, replacement of the sample stage material as well as the shield material, adding an extra thermocouple on the stage. A different sample mounting configuration might require a redesign of the sample stage, one of the ideas is using spring-loaded pressure contact instead of conductive paste contact, however, since most of the samples are small in sizes, extra care must be taken in designing the contact tips/areas. The spring-loaded contact might also help eliminate problems associated with the difference in thermal expansion between the sample and the stage. Since it was suspected that oxide was form on the surface of the samples, an idea is to replace the existing single inlet cryostat with a two inlets cryostat. This allows continuously flushing the chamber with nitrogen gas while pumping the system to vacuum. Replacement of the OFHC copper stage and shield with another more inert metals or alloys or ceramics might help reduce the maintenance effort. Although, the OFHC copper stage is nickel/gold plated on the surface, the high operating temperatures

and constant cooling and heating process in the measurement caused the coating to degrade. The addition of an extra thermocouple on the stage will help determine the contact quality between the sample and the base. This would help to investigate the quality of the thermal interface between the module and the cryostat sample stage. High thermal resistance at this interface would lead to inaccuracies in the module characterization. Continuous improvement in the software, especially in the PID temperature controller implementation, can make the system function more efficiently and more reliably.

APPENDIX A

EDS ANALYSIS FROM SEM IMAGING

Fri Nov 08 16:35:25 2002

KF2229R1C

Refit _Sb-L' _Sb-L" _Cu-L' _Cu-L" _Ni-L' _Ni-L" _Zn-L' _Zn-L" _Fe-L' _Fe-L"
Refit _Ni-L _Fe-L
Filter Fit Method
Chi-sqd = 118.49 Livetime = 100.0 Sec.
Standardless Analysis

Element	Relative k-ratio	Error (1-Sigma)	Net Counts	Error (1-Sigma)
Te-L	0.30336	+/- 0.00361	75389	+/- 896
Sb-L	0.00358	+/- 0.00157	911	+/- 399
Pb-L	0.66727	+/- 0.01676	23727	+/- 596
Cu-L	0.00555	+/- 0.00053	1021	+/- 97
Ni-L	0.00000	+/- 0.00001	0	+/- 0
Zn-L	0.00413	+/- 0.00039	1120	+/- 105
Ag-L	0.01610	+/- 0.00145	4775	+/- 431
Fe-L	0.00000	+/- 0.00001	0	+/- 0

Adjustment Factors	K	L	M
Z-Balance:	0.00000	0.00000	0.00000
Shell:	1.00000	1.00000	1.00000

PROZA Correction Acc.Volt.= 20 kV Take-off Angle=30.00 deg
Number of Iterations = 4

Element	k-ratio (calc.)	Z	A	F	Atom %	Element Wt %	Wt % Err. (1-Sigma)
Te-L	0.260	0.97	1.39	1.00	43.9	35.1	+/- 0.4
Sb-L	0.003	0.94	1.47	1.00	0.6	0.4	+/- 0.2
Pb-L	0.571	1.04	1.00	1.00	46.1	59.9	+/- 1.5
Cu-L	0.005	0.83	3.90	1.00	3.8	1.5	+/- 0.1
Ni-L	0.000	0.78	2.62	1.00	0.0	0.0	+/- 0.0
Zn-L	0.004	0.82	3.82	1.00	2.7	1.1	+/- 0.1
Ag-L	0.014	0.90	1.58	0.99	2.9	1.9	+/- 0.2
Fe-L	0.000	0.80	3.25	1.00	0.0	0.0	+/- 0.0
Total					100.0	100.0	

Figure A. 1 The EDS analysis of the surface of the sample KF2229R1C after the High Temperature (HT) measurement.

Fri Nov 08 16:38:35 2002

KF2229R1C-unscraped

Refit _Sb-L' _Sb-L" _Cu-L' _Cu-L" _Ni-L' _Ni-L" _Zn-L' _Zn-L" _Fe-L' _Fe-L"
Refit _Ni-L _Fe-L
Filter Fit Method
Chi-sqd = 115.24 Livetime = 100.0 Sec.
Standardless Analysis

Element	Relative k-ratio	Error (1-Sigma)	Net Counts	Error (1-Sigma)
Te-L	0.29474	+/- 0.00363	71715	+/- 884
Sb-L	0.00162	+/- 0.00159	402	+/- 396
Pb-L	0.67365	+/- 0.01695	23453	+/- 590
Cu-L	0.00815	+/- 0.00057	1467	+/- 103
Ni-L	0.00000	+/- 0.00001	0	+/- 0
Zn-L	0.00725	+/- 0.00042	1923	+/- 111
Ag-L	0.01459	+/- 0.00146	4237	+/- 425
Fe-L	0.00000	+/- 0.00001	0	+/- 0

Adjustment Factors	K	L	M
Z-Balance:	0.00000	0.00000	0.00000
Shell:	1.00000	1.00000	1.00000

PROZA Correction Acc.Volt.= 20 kV Take-off Angle=30.00 deg
Number of Iterations = 4

Element	k-ratio (calc.)	Z	A	F	Atom %	Element Wt %	Wt % Err. (1-Sigma)
Te-L	0.250	0.97	1.39	1.00	41.6	33.8	+/- 0.4
Sb-L	0.001	0.95	1.47	1.00	0.2	0.2	+/- 0.2
Pb-L	0.571	1.05	1.00	1.00	45.5	60.1	+/- 1.5
Cu-L	0.007	0.83	3.83	1.00	5.4	2.2	+/- 0.2
Ni-L	0.000	0.78	2.59	1.00	0.0	0.0	+/- 0.0
Zn-L	0.006	0.83	3.80	1.00	4.6	1.9	+/- 0.1
Ag-L	0.012	0.90	1.59	0.99	2.6	1.8	+/- 0.2
Fe-L	0.000	0.80	3.22	1.00	0.0	0.0	+/- 0.0
Total					100.0	100.0	

Figure A. 2 The EDS analysis of another surface of the sample KF2229R1C after the High Temperature (HT) measurement.

Wed Dec 11 19:54:34 2002

KF2229R1C-center

Refit _Ag-L' _Ag-L" _Cu-L' _Cu-L" _Cu-K' _Cu-K" _Zn-K' _Zn-K"
Refit _Pb-L" _Cu-L _Cu-K _Zn-K
Filter Fit Method
Chi-sqd = 2.87 Livetime = 100.0 Sec.
Standardless Analysis

Element	Relative k-ratio	Error (1-Sigma)	Net Counts	Error (1-Sigma)
C -K	---	---	790	+/- 43
Pb-M	---	---	41466	+/- 427
Te-L	0.37568	+/- 0.00808	17056	+/- 367
Pb-L	0.61855	+/- 0.09056	683	+/- 100
Ag-L	0.00576	+/- 0.00198	339	+/- 116
Cu-L	---	---	0	+/- 0
Cu-K	0.00000	+/- 0.00001	0	+/- 0
Zn-K	0.00000	+/- 0.00001	0	+/- 0

Adjustment Factors	K	L	M
Z-Balance:	0.00000	0.00000	0.00000
Shell:	1.00000	1.00000	1.00000

PROZA Correction Acc.Volt.= 15 kV Take-off Angle=30.00 deg
Number of Iterations = 4

Element	k-ratio (calc.)	Z	A	F	Atom %	Element Wt %	Wt % Err. (1-Sigma)
Te-L	0.340	0.96	1.23	1.00	52.0	40.3	+/- 0.9
Pb-L	0.560	1.05	1.00	1.00	47.0	59.1	+/- 8.7
Ag-L	0.005	0.89	1.36	0.99	1.0	0.6	+/- 0.2
Cu-K	0.000	0.75	1.05	0.99	0.0	0.0	+/- 0.0
Zn-K	0.000	0.75	1.04	0.99	0.0	0.0	+/- 0.0
Total					100.0	100.0	

Figure A. 3 The EDS analysis inside the sample KF2229R1C after the High Temperature (HT) measurement.

Fri Nov 08 16:31:28 2002

KF2229R1D

Refit _Sb-L' _Sb-L" _Cu-L' _Cu-L" _Ni-L' _Ni-L" _Zn-L' _Zn-L" _Fe-L' _Fe-L"
Refit _Ni-L _Fe-L
Filter Fit Method
Chi-sqd = 143.89 Livetime = 100.0 Sec.
Standardless Analysis

Element	Relative k-ratio	Error (1-Sigma)	Net Counts	Error (1-Sigma)
Te-L	0.31916	+/- 0.00345	92516	+/- 1000
Sb-L	0.00579	+/- 0.00150	1716	+/- 445
Pb-L	0.64590	+/- 0.01519	26788	+/- 630
Cu-L	0.00420	+/- 0.00049	900	+/- 106
Ni-L	0.00000	+/- 0.00001	0	+/- 0
Zn-L	0.00452	+/- 0.00036	1429	+/- 115
Ag-L	0.02042	+/- 0.00144	7065	+/- 497
Fe-L	0.00000	+/- 0.00001	0	+/- 0

Adjustment Factors	K	L	M
Z-Balance:	0.00000	0.00000	0.00000
Shell:	1.00000	1.00000	1.00000

PROZA Correction Acc.Volt.= 20 kV Take-off Angle=30.00 deg
Number of Iterations = 4

Element	k-ratio (calc.)	Z	A	F	Atom %	Element Wt %	Wt % Err. (1-Sigma)
Te-L	0.272	0.97	1.38	1.00	45.4	36.6	+/- 0.4
Sb-L	0.005	0.94	1.45	1.00	0.9	0.7	+/- 0.2
Pb-L	0.551	1.05	1.00	1.00	44.3	57.9	+/- 1.4
Cu-L	0.004	0.83	3.95	1.00	2.9	1.2	+/- 0.1
Ni-L	0.000	0.78	2.65	1.00	0.0	0.0	+/- 0.0
Zn-L	0.004	0.82	3.85	1.00	3.0	1.2	+/- 0.1
Ag-L	0.017	0.90	1.57	0.99	3.6	2.4	+/- 0.2
Fe-L	0.000	0.80	3.29	1.00	0.0	0.0	+/- 0.0
Total					100.0	100.0	

Figure A. 4 The EDS analysis on the surface of the sample KF2229R1D after the High Temperature (HT) measurement.

Wed Dec 11 19:59:43 2002

KF2229R1D-center

Refit _Ag-L' _Ag-L" _Cu-L' _Cu-L" _Cu-K' _Cu-K" _Zn-K' _Zn-K"
Refit _Pb-L' _Pb-L"
Filter Fit Method
Chi-sqd = 2.98 Livetime = 100.0 Sec.
Standardless Analysis

Element	Relative k-ratio	Error (1-Sigma)	Net Counts	Error (1-Sigma)
C -K	---	---	1054 +/-	49
Pb-M	---	---	43251 +/-	436
Te-L	0.35727 +/-	0.00774	17267 +/-	374
Pb-L	0.63125 +/-	0.08422	742 +/-	99
Ag-L	0.00170 +/-	0.00189	107 +/-	119
Cu-L	---	---	261 +/-	54
Cu-K	0.00173 +/-	0.00540	24 +/-	77
Zn-K	0.00805 +/-	0.00708	83 +/-	73

Adjustment Factors	K	L	M
Z-Balance:	0.00000	0.00000	0.00000
Shell:	1.00000	1.00000	1.00000

PROZA Correction Acc.Volt.= 15 kV Take-off Angle=30.00 deg
Number of Iterations = 4

Element	k-ratio (calc.)	Z	A	F	Atom %	Element Wt %	Wt % Err. (1-Sigma)
Te-L	0.325	0.96	1.24	1.00	49.8	38.6	+/- 0.8
Pb-L	0.574	1.05	1.00	1.00	48.2	60.6	+/- 8.1
Ag-L	0.002	0.89	1.37	0.99	0.3	0.2	+/- 0.2
Cu-K	0.002	0.76	1.05	0.99	0.3	0.1	+/- 0.4
Zn-K	0.007	0.75	1.04	0.99	1.4	0.6	+/- 0.5
Total					100.0	100.0	

Figure A. 5 The EDS analysis inside the sample KF2229R1D after the High Temperature (HT) measurement.

Wed Apr 16 19:57:42 2003

KF2242R2A_beforerun

Refit _O -K' _O -K" _Cu-K' _Cu-K" _Sb-L' _Sb-L" _Ag-L' _Ag-L"
Refit _O -K
Filter Fit Method
Chi-sqd = 6.03 Livetime = 100.0 Sec.
Standardless Analysis

Element	Relative k-ratio	Error (1-Sigma)	Net Counts	Error (1-Sigma)
O -K	---	---	0	+/- 0
C -K	---	---	2608	+/- 79
Cu-K	0.00157	+/- 0.00157	145	+/- 145
Te-L	0.30124	+/- 0.00406	57733	+/- 779
Sb-L	0.00551	+/- 0.00178	1082	+/- 350
Pb-L	0.68854	+/- 0.01904	18552	+/- 513
Ag-L	0.00313	+/- 0.00085	720	+/- 195
Pb-M	---	---	128199	+/- 739

Adjustment Factors	K	L	M
Z-Balance:	0.00000	0.00000	0.00000
Shell:	1.00000	1.00000	1.00000

PROZA Correction Acc.Volt.= 20 kV Take-off Angle=33.81 deg
Number of Iterations = 4

Element	k-ratio (calc.)	Z	A	F	Atom %	Element Wt %	Wt % Err. (1-Sigma)
Cu-K	0.001	0.78	1.09	0.97	0.3	0.1	+/- 0.1
Te-L	0.268	0.96	1.37	1.00	46.6	35.3	+/- 0.5
Sb-L	0.005	0.93	1.44	1.00	0.9	0.7	+/- 0.2
Pb-L	0.613	1.03	1.00	1.00	51.6	63.5	+/- 1.8
Ag-L	0.003	0.89	1.55	0.99	0.6	0.4	+/- 0.1
Total					100.0	100.0	

Figure A. 6 The EDS analysis of the sample KF2242R2A before the High Temperature (HT) measurement.

```
Sat May 31 10:40:53 2003

KF2242R2A_after_run

Refit _O -K' _O -K" _Cu-K' _Cu-K" _Sb-L' _Sb-L"
Refit _Ag-L'
Filter Fit Method
Chi-sqd = 7.46     Livetime = 100.0 Sec.
Standardless Analysis
Element   Relative      Error        Net       Error
          k-ratio    (1-Sigma)     Counts  (1-Sigma)
  C -K       ---          ---       4118 +/-    99
  Pb-M       ---          ---     220117 +/-   968
  Te-L   0.30514 +/- 0.00326      95051 +/-  1017
  Pb-L   0.67974 +/- 0.01553      29769 +/-   680
  O -K       ---          ---        192 +/-    78
  Cu-K   0.00289 +/- 0.00128        432 +/-   192
  Sb-L   0.00372 +/- 0.00141       1185 +/-   448
  Ag-L   0.00852 +/- 0.00135       3184 +/-   505

Adjustment Factors          K           L           M
  Z-Balance:          0.00000     0.00000     0.00000
  Shell:              1.00000     1.00000     1.00000

PROZA Correction  Acc.Volt.= 20 kV  Take-off Angle=33.81 deg
Number of Iterations = 4

Element  k-ratio     Z      A      F     Atom %  Element  Wt % Err.
         (calc.)                                  Wt %   (1-Sigma)
  Te-L     0.271   0.96   1.37   1.00    46.7    35.7    +/-  0.4
  Pb-L     0.604   1.03   1.00   1.00    50.5    62.7    +/-  1.4
  Cu-K     0.003   0.78   1.09   0.97     0.6     0.2    +/-  0.1
  Sb-L     0.003   0.94   1.43   1.00     0.6     0.4    +/-  0.2
  Ag-L     0.008   0.89   1.55   0.99     1.6     1.0    +/-  0.2
  Total                                 100.0   100.0
```

Figure A. 7 The EDS analysis of the sample KF2242R2A after the High Temperature (HT) measurement.

```
Sat May 31 10:53:05 2003

KF2242R2A_after_run_3

Refit _Cu-K' _Cu-K" _Sb-L' _Sb-L"
Refit _Pb-L" _O -K"
Filter Fit Method
Chi-sqd = 6.46     Livetime = 100.0 Sec.
Standardless Analysis
Element   Relative     Error        Net      Error
          k-ratio    (1-Sigma)     Counts  (1-Sigma)
  C -K       ---         ---        4472 +/-   104
  Pb-M       ---         ---      157176 +/-   857
  Te-L   0.35745 +/- 0.00436       94001 +/-  1146
  Pb-L   0.58209 +/- 0.01082       21522 +/-   400
  O -K       ---         ---        1260 +/-    77
  Cu-K   0.00298 +/- 0.00147         377 +/-   186
  Sb-L   0.00724 +/- 0.00240        1949 +/-   646
  Ag-L   0.05024 +/- 0.00203       15860 +/-   641
  In-L       ---         ---       41863 +/-   933

Adjustment Factors          K          L          M
  Z-Balance:            0.00000    0.00000    0.00000
  Shell:                1.00000    1.00000    1.00000

PROZA Correction  Acc.Volt.= 20 kV  Take-off Angle=33.81 deg
Number of Iterations = 4

Element  k-ratio     Z      A      F     Atom %  Element  Wt % Err.
         (calc.)                                  Wt %   (1-Sigma)
  Te-L     0.310   0.97   1.33   1.00    49.6    40.1    +/-  0.5
  Pb-L     0.504   1.05   1.00   1.00    40.4    53.1    +/-  1.0
  Cu-K     0.003   0.79   1.09   0.98     0.5     0.2    +/-  0.1
  Sb-L     0.006   0.94   1.40   1.00     1.1     0.8    +/-  0.3
  Ag-L     0.044   0.90   1.47   0.99     8.4     5.7    +/-  0.2
  Total                                 100.0   100.0
```

Figure A. 8 The EDS analysis of another surface of sample KF2242R2A after the High Temperature (HT) measurement.

Wed Dec 11 19:42:39 2002

KF2242R2B

Refit _Ag-L' _Ag-L" _Cu-L' _Cu-L" _Cu-K' _Cu-K" _Zn-K' _Zn-K"
Refit _Pb-L" _Cu-K
Filter Fit Method
Chi-sqd = 3.13 Livetime = 100.0 Sec.
Standardless Analysis

Element	Relative k-ratio	Error (1-Sigma)	Net Counts	Error (1-Sigma)
C -K	---	---	979	+/- 49
Pb-M	---	---	48727	+/- 465
Te-L	0.38190	+/- 0.00768	19836	+/- 399
Pb-L	0.61115	+/- 0.08233	772	+/- 104
Ag-L	0.00091	+/- 0.00189	61	+/- 128
Cu-L	---	---	183	+/- 54
Cu-K	0.00000	+/- 0.00001	0	+/- 0
Zn-K	0.00605	+/- 0.00704	67	+/- 78

Adjustment Factors	K	L	M
Z-Balance:	0.00000	0.00000	0.00000
Shell:	1.00000	1.00000	1.00000

PROZA Correction Acc.Volt.= 15 kV Take-off Angle=30.00 deg
Number of Iterations = 4

Element	k-ratio (calc.)	Z	A	F	Atom %	Element Wt %	Wt % Err. (1-Sigma)
Te-L	0.347	0.96	1.23	1.00	52.5	40.9	+/- 0.8
Pb-L	0.555	1.06	1.00	1.00	46.3	58.6	+/- 7.9
Ag-L	0.001	0.89	1.36	0.99	0.2	0.1	+/- 0.2
Cu-K	0.000	0.76	1.05	0.99	0.0	0.0	+/- 0.0
Zn-K	0.005	0.75	1.04	0.99	1.1	0.4	+/- 0.5
Total					100.0	100.0	

Figure A. 9 The EDS analysis of the sample KF2242R2B before the High Temperature (HT) measurement.

Tue Dec 17 11:19:15 2002

KF2242R2B_1

Refit _Sb-L' _Sb-L" _Ag-L' _Ag-L"
Filter Fit Method
Chi-sqd = 2.80 Livetime = 100.0 Sec.
Standardless Analysis

Element	Relative k-ratio	Error (1-Sigma)	Net Counts	Error (1-Sigma)
Pb-M	0.64743	+/- 0.00373	172381	+/- 994
Te-L	0.33912	+/- 0.00400	76380	+/- 902
Sb-L	0.00758	+/- 0.00175	1746	+/- 402
Ag-L	0.00587	+/- 0.00084	1577	+/- 225

Adjustment Factors	K	L	M
Z-Balance:	0.00000	0.00000	0.00000
Shell:	1.00000	1.00000	1.00000

PROZA Correction Acc.Volt.= 20 kV Take-off Angle=30.00 deg
Number of Iterations = 5

Element	k-ratio (calc.)	Z	A	F	Atom %	Element Wt %	Wt % Err. (1-Sigma)
Pb-M	0.554	1.02	1.06	1.00	47.6	59.7	+/- 0.3
Te-L	0.290	0.96	1.38	1.00	50.1	38.7	+/- 0.5
Sb-L	0.006	0.94	1.46	1.00	1.2	0.9	+/- 0.2
Ag-L	0.005	0.89	1.58	0.99	1.1	0.7	+/- 0.1
Total					100.0	100.0	

Figure A. 10 The EDS analysis of the sample KF2242R2B after the High Temperature (HT) measurement.

Tue Dec 17 11:26:53 2002

KF2242R2B_2

Refit _Sb-L' _Sb-L" _Ag-L' _Ag-L" _Cu-K' _Cu-K"
Filter Fit Method
Chi-sqd = 2.38 Livetime = 100.0 Sec.
Standardless Analysis

Element	Relative k-ratio	Error (1-Sigma)	Net Counts	Error (1-Sigma)
Pb-M	0.65292	+/- 0.00353	206180	+/- 1116
Te-L	0.33817	+/- 0.00369	90336	+/- 987
Sb-L	0.00203	+/- 0.00160	554	+/- 438
Ag-L	0.00328	+/- 0.00077	1046	+/- 245
Cu-K	0.00360	+/- 0.00138	472	+/- 181

Adjustment Factors	K	L	M
Z-Balance:	0.00000	0.00000	0.00000
Shell:	1.00000	1.00000	1.00000

PROZA Correction Acc.Volt.= 20 kV Take-off Angle=30.00 deg
Number of Iterations = 5

Element	k-ratio (calc.)	Z	A	F	Atom %	Element Wt %	Wt % Err. (1-Sigma)
Pb-M	0.560	1.02	1.06	1.00	48.2	60.4	+/- 0.3
Te-L	0.290	0.96	1.39	1.00	50.2	38.7	+/- 0.4
Sb-L	0.002	0.94	1.46	1.00	0.3	0.2	+/- 0.2
Ag-L	0.003	0.89	1.59	0.99	0.6	0.4	+/- 0.1
Cu-K	0.003	0.79	1.10	0.97	0.7	0.3	+/- 0.1
Total					100.0	100.0	

Figure A. 11 The EDS analysis of another surface of sample KF2242R2B after the High Temperature (HT) measurement.

Mon Mar 17 16:46:39 2003

KF2242r2c (first one)

Refit _O -K' _O -K" _Ag-L' _Ag-L" _Sb-L' _Sb-L"
Refit _O -K
Filter Fit Method
Chi-sqd = 6.17 Livetime = 60.0 Sec.
Standardless Analysis

Element	Relative k-ratio	Error (1-Sigma)	Net Counts	Error (1-Sigma)
C -K	---	---	2125 +/-	73
O -K	---	---	0 +/-	0
Ag-L	0.00432 +/-	0.00091	881 +/-	185
Sb-L	0.00725 +/-	0.00190	1320 +/-	346
Te-L	0.31777 +/-	0.00431	57097 +/-	775
Pb-L	---	---	34364 +/-	623
Pb-M	0.67066 +/-	0.00438	122606 +/-	801

Adjustment Factors	K	L	M
Z-Balance:	0.00000	0.00000	0.00000
Shell:	1.00000	1.00000	1.00000

PROZA Correction Acc.Volt.= 25 kV Take-off Angle=30.98 deg
Number of Iterations = 5

Element	k-ratio (calc.)	Z	A	F	Atom %	Element Wt %	Wt % Err. (1-Sigma)
Ag-L	0.004	0.90	1.78	0.99	0.9	0.6	+/- 0.1
Sb-L	0.006	0.94	1.63	1.00	1.2	0.9	+/- 0.2
Te-L	0.260	0.97	1.53	1.00	49.9	38.5	+/- 0.5
Pb-M	0.548	1.02	1.08	1.00	48.0	60.1	+/- 0.4
Total					100.0	100.0	

Figure A. 12 The EDS analysis of sample KF2242R2C before the High Temperature (HT) measurement.

Thu Apr 10 19:26:39 2003

KF2242R2C_postrun

Refit _Sb-L' _Sb-L" _O -K' _O -K"
Refit _Ag-L' _Ag-L"
Filter Fit Method
Chi-sqd = 7.06 Livetime = 100.0 Sec.
Standardless Analysis

Element	Relative k-ratio	Error (1-Sigma)	Net Counts	Error (1-Sigma)
Ag-L	0.01261	+/- 0.00093	3049	+/- 226
Sb-L	0.00531	+/- 0.00185	1095	+/- 381
Te-L	0.34519	+/- 0.00424	69528	+/- 855
Pb-M	0.63689	+/- 0.00381	155765	+/- 932
C -K	---	---	3076	+/- 86
O -K	---	---	123	+/- 65
Pb-L	---	---	21484	+/- 546

Adjustment Factors	K	L	M
Z-Balance:	0.00000	0.00000	0.00000
Shell:	1.00000	1.00000	1.00000

PROZA Correction Acc.Volt.= 20 kV Take-off Angle=33.81 deg
Number of Iterations = 5

Element	k-ratio (calc.)	Z	A	F	Atom %	Element Wt %	Wt % Err. (1-Sigma)
Ag-L	0.011	0.90	1.52	0.99	2.2	1.5	+/- 0.1
Sb-L	0.005	0.94	1.41	1.00	0.8	0.6	+/- 0.2
Te-L	0.298	0.97	1.35	1.00	50.0	38.8	+/- 0.5
Pb-M	0.550	1.02	1.06	1.00	46.9	59.1	+/- 0.4
Total					100.0	100.0	

Figure A. 13 The EDS analysis of sample KF2242R2C after the High Temperature (HT) measurement.

Thu Apr 10 19:31:46 2003

KF2242R2C_postrun_2

Refit _Ag-L' _Ag-L" _Sb-L' _Sb-L" _O -K' _O -K"
Filter Fit Method
Chi-sqd = 6.65 Livetime = 100.0 Sec.
Standardless Analysis

Element	Relative k-ratio	Error (1-Sigma)	Net Counts	Error (1-Sigma)
Ag-L	0.00399	+/- 0.00091	920	+/- 211
Sb-L	0.00299	+/- 0.00189	589	+/- 371
Te-L	0.34566	+/- 0.00434	66475	+/- 834
Pb-M	0.64736	+/- 0.00392	151165	+/- 915
C -K	---	---	2694	+/- 83
O -K	---	---	3	+/- 64
Pb-L	---	---	21225	+/- 546

Adjustment Factors	K	L	M
Z-Balance:	0.00000	0.00000	0.00000
Shell:	1.00000	1.00000	1.00000

PROZA Correction Acc.Volt.= 20 kV Take-off Angle=33.81 deg
Number of Iterations = 5

Element	k-ratio (calc.)	Z	A	F	Atom %	Element Wt %	Wt % Err. (1-Sigma)
Ag-L	0.003	0.89	1.53	0.99	0.7	0.5	+/- 0.1
Sb-L	0.003	0.94	1.41	1.00	0.5	0.3	+/- 0.2
Te-L	0.300	0.96	1.35	1.00	50.6	39.0	+/- 0.5
Pb-M	0.561	1.02	1.06	1.00	48.2	60.2	+/- 0.4
Total					100.0	100.0	

Figure A. 14 The EDS analysis of another surface of sample KF2242R2C before the High Temperature (HT) measurement.

Thermo NORAN

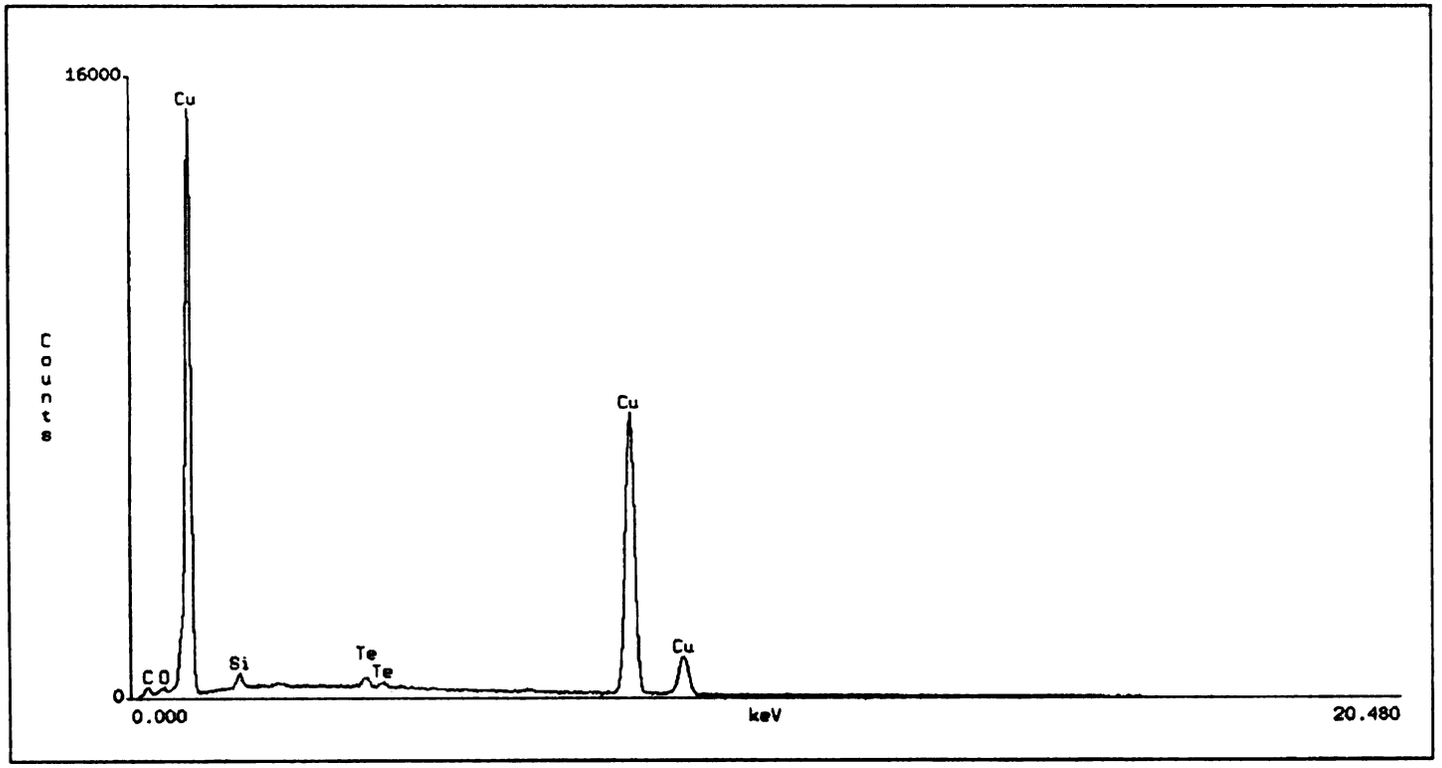

copper plate - 1

Accelerating Voltage: 20 KeV
Live Time: 100 seconds
Take Off Angle: 36.4647°
Dead Time: 24.813

Figure A. 15 The copper plate coated with tellurium (Te).

APPENDIX B

For a fully degenerate semiconductor, a better approximation to obtain $<\tau>$, $<E\tau>$ and $<E^2\tau>$ can be obtained from the equation

$$<\tau>= -E_F^{-\frac{3}{2}} \int_0^{\infty} \tau E^{\frac{3}{2}} \frac{\partial f_o}{\partial E} dE$$

A better approximation

$-\int_0^{\infty} \phi(E) \frac{\partial f_o}{\partial E} dE$ is used and expanding $\phi(E)$ in powers of $(E-E_F)$, we get

$$\phi(E) = \phi(E_F) + (E - E_F)\phi'(E_F) + \tfrac{1}{2}(E - E_F)^2 \phi''(E_F) + ...$$

On integrating, we can obtain the values

$$\int_0^{\infty} \frac{\partial f_o}{\partial E} dE = -1$$

$$\int_0^{\infty} (E - E_F) \frac{\partial f_o}{\partial E} dE = 0$$

$$\int_0^{\infty} (E - E_F)^2 \frac{\partial f_o}{\partial E} dE = -\frac{\pi^2}{3} k^2 T^2$$

So, we have

$$-\int_0^{\infty} \phi(E) \frac{\partial f_o}{\partial E} dE = \phi(E_F) + \frac{\pi^2}{6} (kT)^2 \phi''(E_F) + ...$$

Applying this approximations to $<\tau>$, $<E^2\tau>$, $<E\tau>^2$ and we get

$$\langle\tau\rangle\langle E^2\tau\rangle - \langle E\tau\rangle^2 = \tfrac{1}{3}\pi^2 k^2 T^2 \langle\tau\rangle^2$$

APPENDIX C

THERMOMECHANICAL ANALYZER

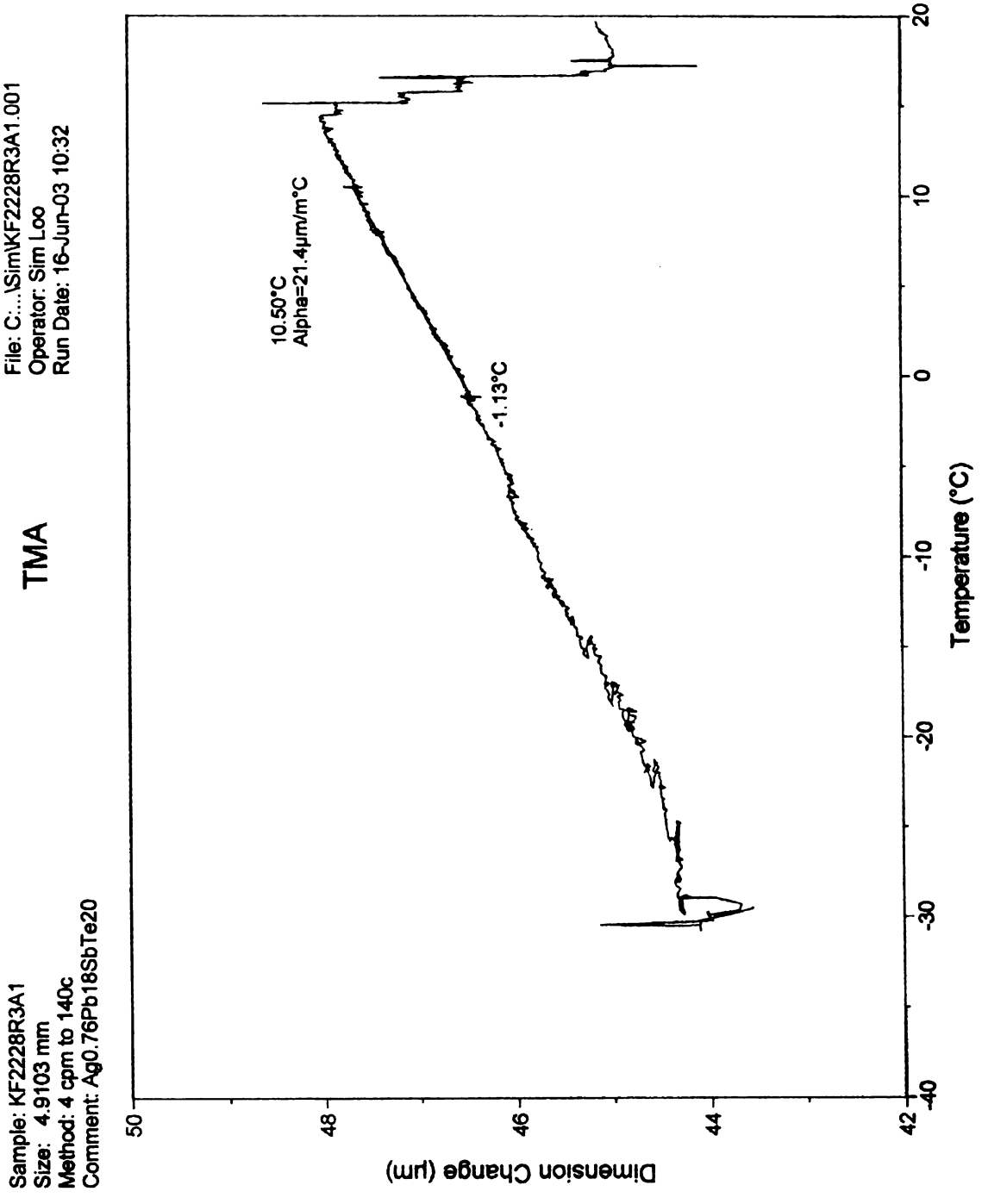

APPENDIX D

Energy Band Gap Measurement

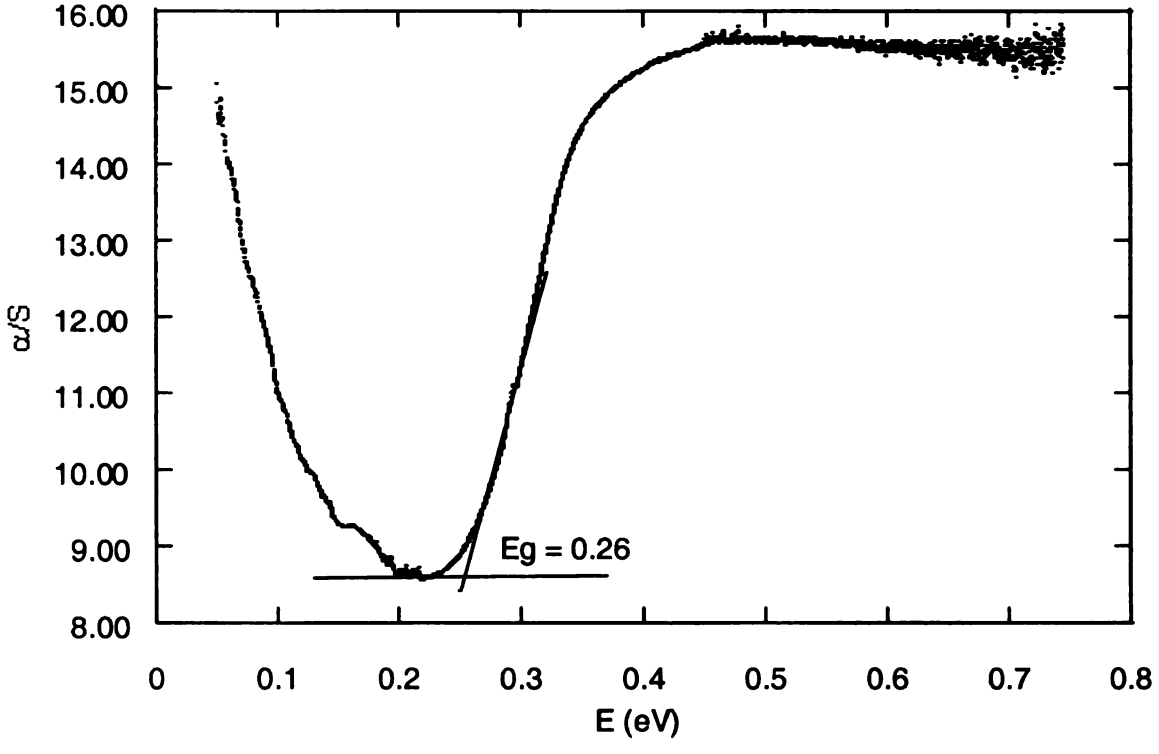

The Energy bandgap (= 0.26 eV) is obtained through the room temperature optical measurement. The composition of this sample is $AgPb_{18}SbTe_{20}$.

APPENDIX E

MathCAD Simulation codes

$T := 80..500$

The Properties of KF2229R1C (n-type)

$S_n(T) := -17.192 + 0.085565 \cdot T - 0.0026058 \cdot T^2 + 4.7082 \cdot 10^{-6} \cdot T^3 - 2.8012 \cdot 10^{-9} \cdot T^4$

$\sigma_n(T) := 9345.7 - 59.938 \cdot T + 0.18984 \cdot T^2 - 0.00034629 \cdot T^3 + 3.3847 \cdot 10^{-7} \cdot T^4 - 1.3493 \cdot 10^{-10} \cdot T^5$

$\kappa_n(T) := 4.9247 - 0.010908 \cdot T + 1.1364 \cdot 10^{-5} \cdot T^2 - 1.2814 \cdot 10^{-9} \cdot T^3$

Dimensions of A and L are in meters

$A_n := 0.0027 \cdot 0.0028 \quad L_n := .0036$

$Z_n(T) := S_n(T)^2 \cdot \frac{\sigma_n(T)}{\kappa_n(T)}$

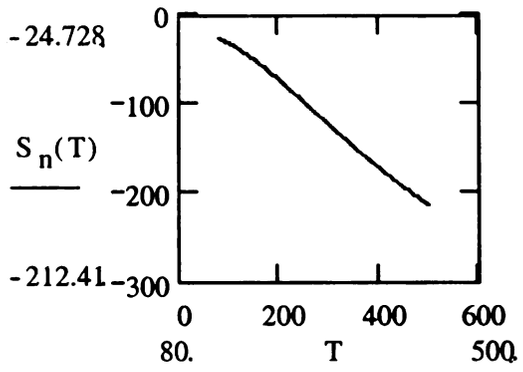

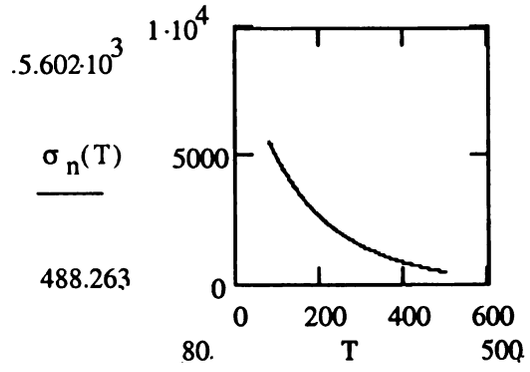

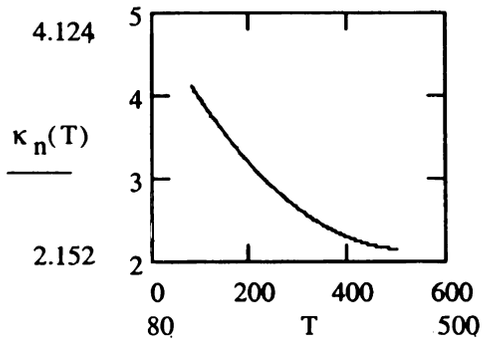

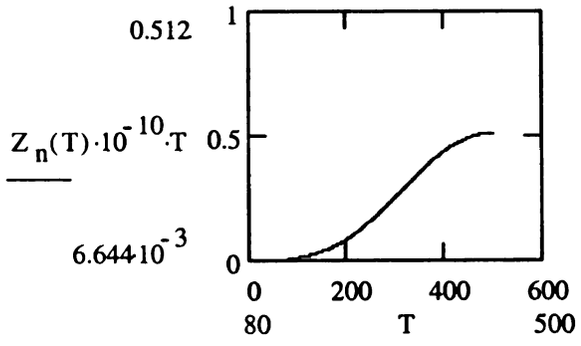

The Properties of Do066a_0118 (p-type)

$$S_p(T) := 6.2407 + 0.35449 \cdot T$$

$$\sigma_p(T) := 1096.3 - 0.5133 \cdot T - 0.0028289 \cdot T^2 + 3.7148 \cdot 10^{-6} \cdot T^3$$

$$\kappa_p(T) := 0.93438 + 0.0031056 \cdot T - 7.6469 \cdot 10^{-6} \cdot T^2 + 1.0122 \cdot 10^{-8} \cdot T^3$$

Dimensions of A and L are in meters

$$A_p := .002 \cdot .0033 \qquad L_p := 0.0036$$

$$Z_p(T) := S_p(T)^2 \cdot \frac{\sigma_p(T)}{\kappa_p(T)}$$

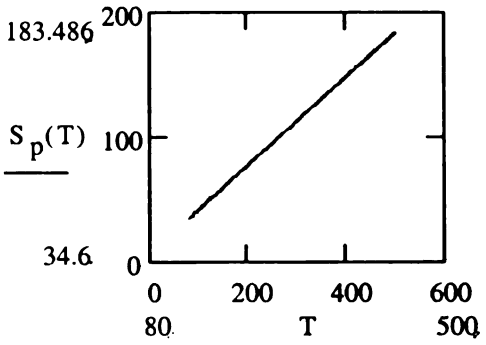

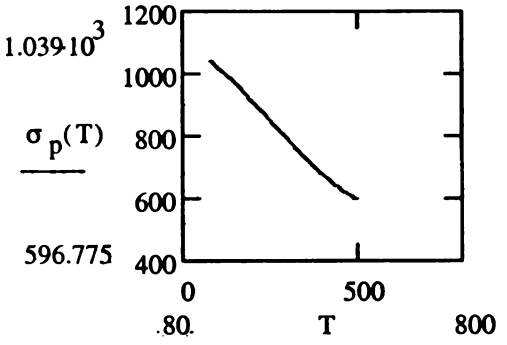

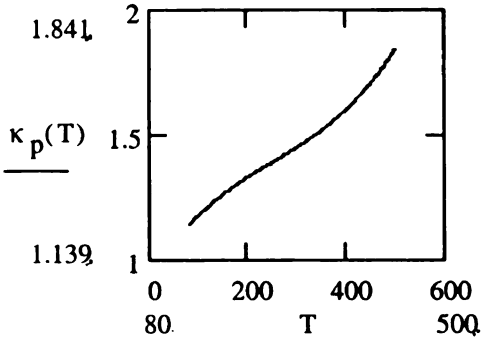

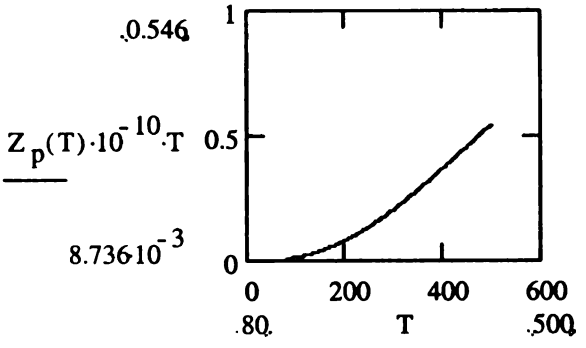

Resistivity is in ohm cm

$$\gamma_n := \frac{A_n}{L_n} \qquad \gamma_p := \frac{A_p}{L_p} \qquad \rho_n(T) := \frac{1}{\sigma_n(T)} \qquad \rho_p(T) := \frac{1}{\sigma_p(T)}$$

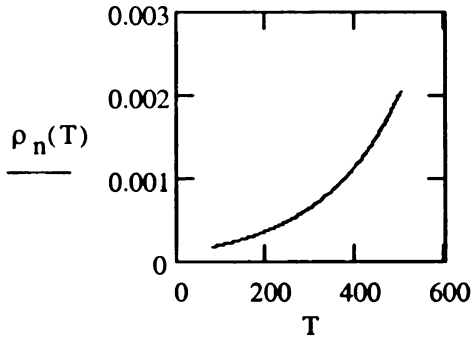

$$R_n(T) := \frac{\rho_n(T) \cdot 0.01}{\gamma_n}$$

$$R_p(T) := \frac{\rho_p(T) \cdot 0.01}{\gamma_p}$$

The properties of the Module

$$S_M(T) := \left| S_n(T) \right| + \left| S_p(T) \right|$$

$$R_{int}(T) := R_n(T) + R_p(T)$$

$$K_M(T) := \kappa_n(T) \cdot \gamma_n + \kappa_p(T) \cdot \gamma_p$$

$$Z(T) := \frac{S_M(T)^2 \cdot 10^{-12}}{K_M(T) \cdot R_{int}(T)}$$

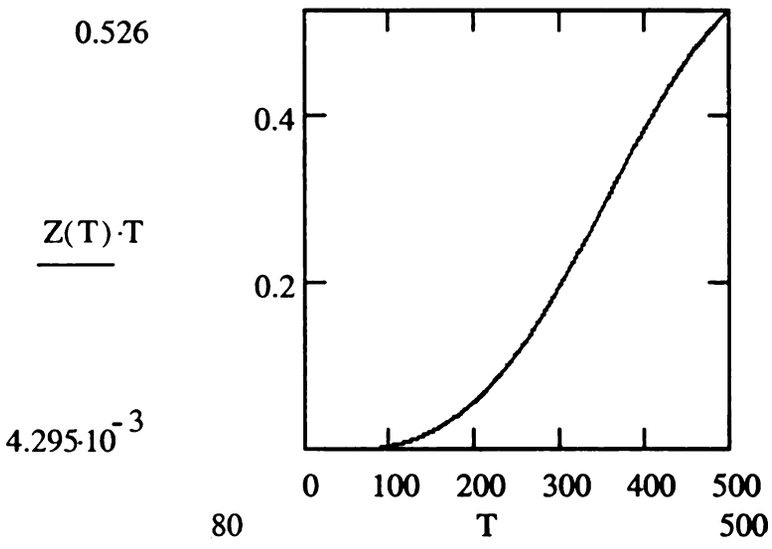

The unit of the load current is in Amp

$$R_{cont} := 3 \cdot 10^{-3}$$

$$R_M(T) := R_{int}(T) + R_{cont}$$

$$\Delta T := 0 .. 200$$

$$I := 0, .1 .. 10$$

$$T_h := 500$$

$$T_M(T_h, \Delta T) := T_h - \frac{\Delta T}{2}$$

$$Q_h(\Delta T, I) := \left(S_M\left(T_M\left(T_h, \Delta T\right)\right) \cdot 10^{-6}\right) \cdot \frac{I}{2} \cdot \left(T_h - \Delta T\right) + K_M\left(T_M\left(T_h, \Delta T\right)\right) \cdot (\Delta T) - \frac{\left(\frac{I}{2}\right)^2 \cdot R_M\left(T_M\left(T_h, \Delta T\right)\right)}{2}$$

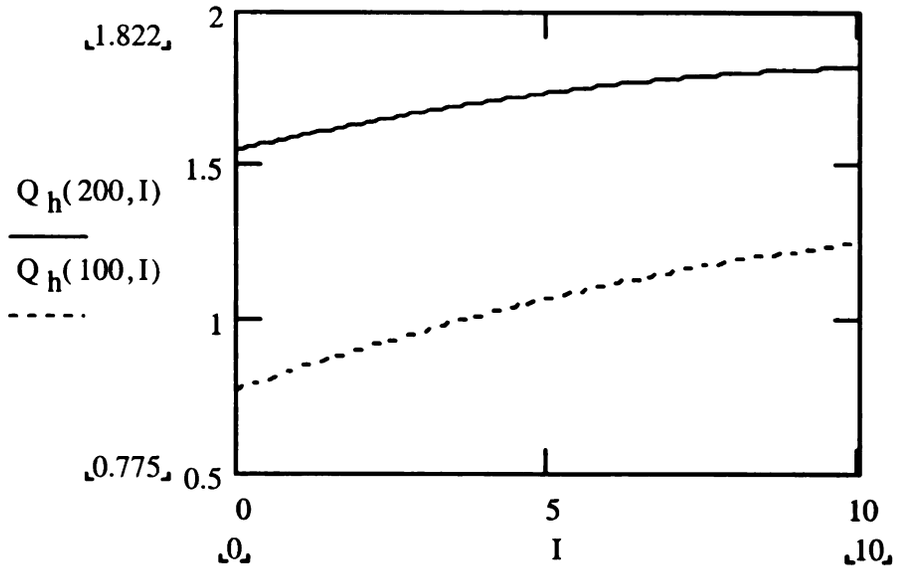
1.822
2
1.5
Q h(200, I)
Q h(100, I)
1
0.775
0.5
0
5
10
0
I
10

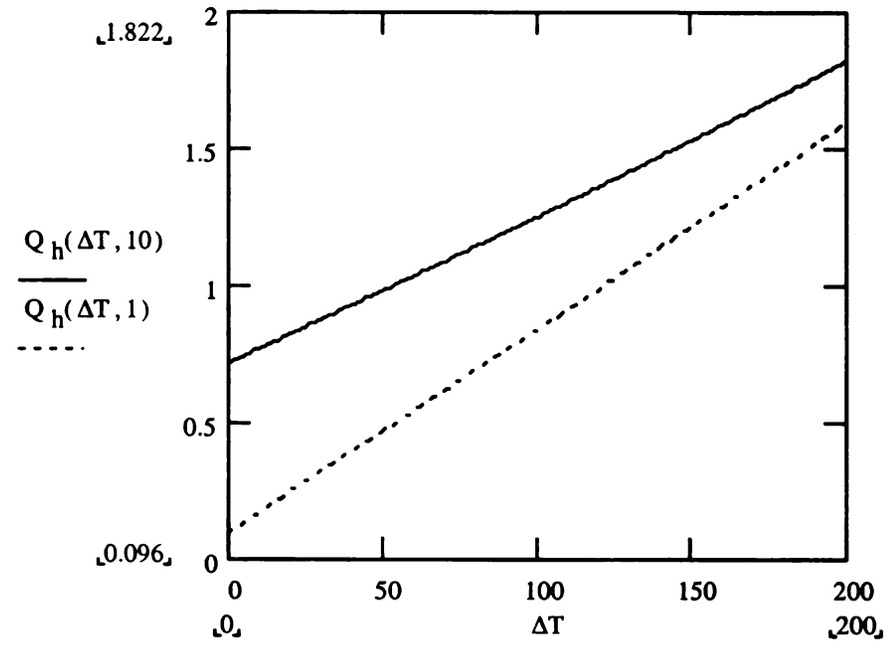
1.822
2
1.5
Q h(ΔT, 10)
Q h(ΔT, 1)
1
0.5
0.096
0
0
50
100
150
200
0
ΔT
200

Open circuit voltage, Voc

$$V_{oc}(\Delta T) := S_M\left(T_M\left(T_h, \Delta T\right)\right) \cdot 10^{-6} \cdot \Delta T$$

$$R_L := R_M(300)$$

Electrical Output Power, We

$$W_e(\Delta T) := \frac{\left(S_M\left(T_M\left(T_h, \Delta T\right)\right) \cdot \Delta T\right)^2 \cdot 10^{-12} \cdot R_L}{\left(R_L + R_M\left(T_M\left(T_h, \Delta T\right)\right)\right)^2}$$

Efficiency

$$\eta_h(\Delta T, I) := \frac{W_e(\Delta T)}{Q_h(\Delta T, I)}$$

For fixed temperature gradient of 200K

$$V_{oc}(200) = 0.064$$

Load current

$$\sqrt{\frac{W_e(200)}{R_L}} = 2.148$$

Load voltage

$$\sqrt{W_e(200) \cdot R_L} = 0.028$$

Total internal resistance

$$R_M\left(T_M(500, 200)\right) = 0.017$$

$$W_e(200) = 0.06$$

$$\eta_h(200, 2.6) = 0.036$$

$$Q_h(200, 2.6) = 1.662$$

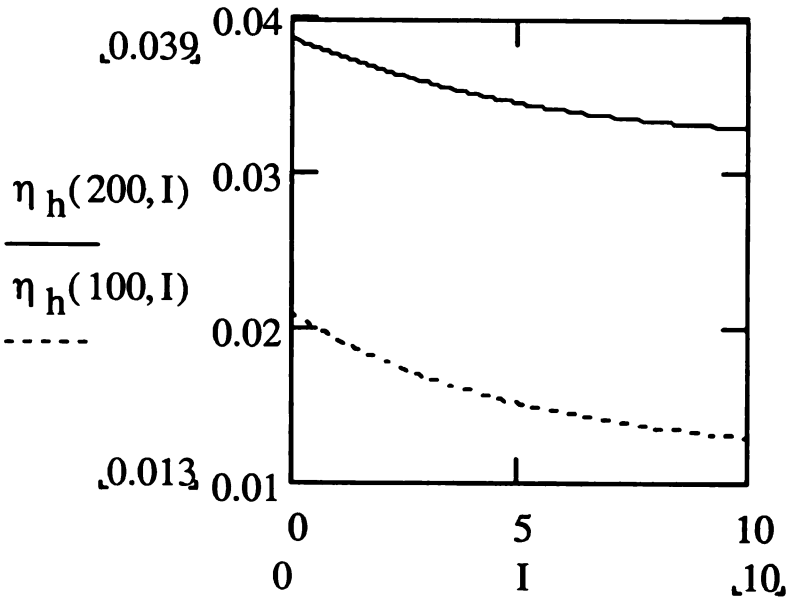
0.039
0.04
η h(200, I)
0.03
η h(100, I)
0.02
0.013
0.01
0
5
10
0
I
10

REFERENCE

[1] H. J. Goldsmid, *Thermoelectric Refrigeration*, Plenum, New York, NY, 1964.

[2] D. D. Pollock, *The Theory and Properties of Thermocouple Elements*, American Society For Testing and Materials, 1971.

[3] F. J. DiSalvo, "Thermoelectric Cooling and Power Generation", *Science*, vol. 285 (1999).

[4] S. Y. Loo, *36-sample Measurement System For Doping and Alloying Trends in New Thermoelectric Materials*, Master Thesis (2000) pp. 19-25.

[5] T. P. Hogan, "Thermoelectricity," *Encyclopedia of Physical Science and Technology*, vol. 16, (2002).

[6] H.J. Goldsmid, *CRC Handbook of Thermoelectrics*, ed. D. M. Rowe (1995) pp.19-25.

[7] H.J. Goldsmid, "The use of semiconductors in thermoelectric refrigeration", *British Journal of Applied Physics*. Vol. 5, Nov. 1954.

[8] M. H. Ettenberg, W. A. Jesser and P. D. Rosi, *Proc. 15th Int. Conf. On Thermoelctrics* 52-56 (IEEE, Piscataway, NJ, 1996).

[9] L. D. Hicks, M. S. Dresselhaus, *Phy. Rev. B*, vol. 47, no.19, pp. 12727, (1993).

[10] R. P. Chasmar and R. Stratton, *J. Electron. Control* 7, 52 (1959).

[11] G. Mahan, "Good Thermoelectrics", *Solid State Physics*, vol. 5.1, 1998.

[12] N. F. Mott, *The Theory of the Properties of Metals and Alloys*, Dover Publications, New York, NY.

[13] G. A. Slack, *CRC Handbook of Thermoelectrics*, ed. D. M. Rowe, (1995) pp.407-440.

[14] M. G. Kanatzidis, et al, "Thermoelectric Materials: Solid State Synthesis," *Naval Res. Rev.* Vol. 48, No. 4 (1996).

[15] D. Y. Chung, et al, "Complex Chalcogenides as Thermoelectric Materials: A Solid State Chemistry Approach," *Bull. Korean Chem. Soc.* Vol. 19, No. 12 (1998), pp. 1283-1293.

[16] S. Sportouch, et al, "Thermoelectric Properties of the Cubic Family of Compounds $AgPbBiQ_3$ (Q=S, Se, Te). Very Low Thermal Conductivity Materials," *Mat. Res. Soc. Symp. Proc.*, Vol. 545 (1999), pp.123-130.

[17] R. Venkatasubramanian, "Thin-film thermoelectric devices with high room-temperature figure of merit," *Nature* (2001)

[18] A. F. Ioffe, *Semiconductor Thermoelements and Thermoelectric Cooling*, Infosearch Limited, London, 1957

[19] M. G. Kanatzidis, "The Role of Solid-State Chemistry in the Discovery of New Thermoelectric Materials", in *Solid State Physics*, ed. H. Ehrenreich, F. Spaepen, vol. 69, pp51-100, Academic Press, New York, 2001

[20] H. Scherrer and S. Scherrer, *CRC Handbook of Thermoelectrics*, pp.211-237.

[21] C. B. Vining, *CRC Handbook of Thermoelectrics*, pp.329-337.

[22] A. L. Jain, "Temperature Dependence of the Electrical Properties of Bismuth-Antimony Alloys," *Physical Review*, Vol. 114, No. 6, June 15 1959.

[23] W. M. Yim and A. Smith, *Solid-State Electron*, **15**, 1141, 1972.

[24] http://virtual.clemson.edu/groups/TMRL/Papers/MATERIAL/skudclath/Ann-Rev-MS-29-89.pdf July 30, 2003.

[25] G. S. Nolas, D.T. Morelli, T. M. Tritt, "Skutterudites: A Phonon-Glass-Electron Crystal Approach to Advanced Thermoelectric Energy Conversion Applications," *Annu. Rev. Mater. Sci.*, pp. 89-116, 1999.

[26] G. S. Nolas, et al., "High figure of merit in partially filled ytterbium skutterudites materials," *Appl. Phys. Letts.* Vol. 77, No. 12, 2000.

[27] G. A.Lamberton, et al., "High figure of merit in Eu-filled $CoSb_3$-based skutterudites," *Appl. Phys. Letts.* Vol. 80, No. 4, 2002.

[28] http://ethomas.web.wesleyan.edu/ees123/clathrate.htm July 30, 2003.

[29] G. S. Nolas, et al., "Semiconducting Ge clathrates: Promising candidates for thermoelectric applications," *Applied Physics Letters*, Vol. 73, No. 2, July 13 1998.

[30] G. S. Nolas, et al., "Transport properties of polycrystalline type-I Sn clathrates," *Physical Review B*, Vol. 65, 165201, 2002.

[31] S. Bhattacharya, et al., "Effect of Sb doping on the thermoelectric properties of Ti-based half-Heusler compounds, $TiNiSn_{1-x}Sb_x$," *Appl. Phys. Lett.* , Vol. 77, No. 16, 16 Oct. 2000.

[32] C. Uher, J. Yang, et al., "Transport properties of pure and doped MNiSn (M=Zr, Hf)," *Phys. Review B*, Vol. 59, No. 13, 1 April 1999.

[33] E. A. Skrabek and D. S. Trimmer, *CRC Handbook of Thermoelectrics*, ed. D. M. Rowe, (1995) pp.267-274.

[34] D.-Y. Chung et al., *Chem. Mater. 9*, 3060 (1997).

[35] D.- Y. Chung, T. Hogan, et al., "$CsBi_4Te_6$: A High-Performance Thermoelectric Material for Low-Temperature Applications," *Science*, Vol. 287, pp.1024-1027, 11 Feb. 2000.

[36] S. Sportouch, et al, "Thermoelectric Properties of the Cubic Family of Compounds $AgPbBiQ_3$ (Q=S, Se, Te). Very Low Thermal Conductivity Materials," *Mat. Res. Soc. Symp. Proc.*, Vol. 545 (1999), pp.123-130.

[37] R. Venkatasubramanian, et al., "Low temperature organometallic epitaxy and its application to superlattice structures in thermoelectrics," *Appl. Phys. Lett.* 75, 1104-1106 (1999).

[38] R. Venkatasubramanian, "Low temperature chemical vapor depostion and etching apparatus and method". US Patent No. 6071351 (6 June 2000).

[39] T.C. Harman, et al., "Quantum Dot Superlattice Thermoelectric Materials and Devices," *Science*, Vol. 297, Sep. 27, 2002

[40] R. Taylor, *CRC Handbook of Thermoelectrics*, ed. D. M. Rowe, (1995) pp.166.

[41] A. D. Stuckes and R. P. Chasmar, *Report of the Meeting on Semiconductors*, The Physical Society, London, England, 1956, pp.119.

[42] H. J. Goldsmid, PhD thesis, University of London (1957).

[43] T. C. Harman, J. H. Cahn, and M. J. Logan, "Measurement of Thermal Conductivity by Utilization of the Peltier Effect," *Journal of Applied Physics*, Vol. 30, No. 9, September 1959.

[44] O. Maldonado, *Cryogenics* (1992), Vol. 32, No 10

[45] R. T. Littleton IV, *et. al.*, "High Temperature Transport Probe for Thermopower and Resistivity Measurements," *Symposium Z: Thermoelectric Materials, 1998 Fall Materials Research Society Proceeding.*

[46] B. M. Zawilski, R. T. Littleton IV, T. M. Tritt, *Review of Scientific Instruments*, vol. 72, no.3, (2001)

[47] T. Hogan, et. al., "Measurement System for Doping and Alloying Trends in New Thermoelectric Materials," *Materials Research Society Symposium Proceedings,* Vol. 545 (1999).

[48] T. A. Al-Obaidi and H. J. Goldsmid, "Determination of the Thermoelectric Figure of Merit from Thermal Conductivity Measurements," *Energy Conversion*, Vol. 9, pp. 131-132, 1969.

[49] T. C. Harman, J. M. Honig, *J. Appl. Phys.*,13, 440, 1962.

[50] C. Wood, "Materials for thermoelectric energy conversion", *Rep. Prog. Phys.* 51, 1988, pp.459-539.

[51] Solid State Cooling Systems, http://www.sscooling.com/Module_Reliability.pdf, July 11, 2003

[52] Ferrotec America Corporation, http://www.ferrotec-america.com/3ref6.htm, July 11, 2003.

[53] T. Caillat, J.-P. Fleurial, et al., "Progress in the development of segmented thermoelectric unicouples at the Jet Propulsion Laboratory", *Mat. Res. Soc. Symp.* Vol. 626 Z11.6.1, 2000.

[54] http://newton.ex.ac.uk/teaching/CDHW/Feedback/ControlTypes.html#FbkTypes May 15, 2003

[55] LakeShore User's Manual Model 330 Autotuning Temperature Controller, 11 August 1998, Chapter 3.3.5 Manual control settings (PID), pg. 3-10 to 3-11.

[56] R. P. Tye, *Thermal Conductivity Vol. 1,* Academic Press, London and New York, 1969.

[57] *CRC handbook of Chemistry and Physics*, ed. By D. R. Lide, 76th Edition, CRC Press 1990-1999.

[58] Goodfellow catalog 2000/2001.

[59] S. O. Kasap, *Principles of Electrical Engineering Materials and Devices,* Revised Edition, McGraw-Hill, 2000.

[60] T. Hogan, et al., "Measurement System for Doping and Alloying Trends in New Thermoelectric Materials," *Eighteenth International Conference on Thermoelectrics Proceedings*, pp. 671-674, 1999.

[61] H. J. Goldsmid and J.W. Sharp, "Estimation of the Thermal Band Gap of a Semiconductor from Seebeck Measurements," *J. of Electronic Materials*, Vol. 28, No. 7, 1999

[62] G. A. Thomas, *et al.*, "Large electronic-density increase on cooling a layered metal: Doped Bi_2Te_3," *Phys. Rev. B*, Vol. 46, No. 3, 1992

[63] Appendix A, Figure A.4.

[64] Appendix A, Figure A.5.

[65] Appendix A, Figure A.1 to A.3.

[66] J. G. Hust and A. B. Lankford, "National Bureau of Standards Certificate, Standard Reference Materials 1460, 1461 and 1462 Austenitic Stainless Steel Thermal Conductivity and Electrical Resistivity as a Function of Temperature from 2 to 1200K".

[67] Appendix A, Figures A.6 to A.14.

[68] R. A. Smith, *Semiconductors*, Cambridge University Press, 1961.

[69] M. Ohring, *The Materials Science of Thin Films,* Academic Press, 1992, pp. 81.

[70] Appendix C, TMA Data.

[71] Appendix A, Figures A.15.

[72] S. Lal, et al., "Thermoelectric module for low temperature applications," *Mat. Res. Soc. Symp. Proc.* Vol. 691, G6.2.1, 2002.